TESIS DOCTORAL

CELLULAR DYNAMICS MODELS OF ANGIOGENESIS

Rocío Vega Martínez

Tesis depositada en cumplimiento parcial de los requisitos para el grado de Doctor en

Ingeniería Matemática

Universidad Carlos III de Madrid

Directores:

Luis L. Bonilla
Manuel Carretero Cerrajero

Tutor:

Luis L. Bonilla

Enero, 2021

Que ser valiente no salga tan caro,
que ser cobarde no valga la pena.
— Joaquín Sabina

Agradecimientos

Me gustaría expresar mi más sincera gratitud a todas aquellas personas que han contribuido, de alguna forma, al desarrollo de este trabajo. En primer lugar, a mis directores Luis L. Bonilla y Manuel Carretero. Tuve la gran oportunidad de trabajar con vosotros y, sobre todo, aprender de vosotros desde que empecé con la ayuda al máster hasta el fin de mi tesis doctoral. Aún recuerdo aquella primera reunión en la que me preguntásteis qué me gustaría hacer en el futuro. Os contesté que investigar en matemáticas relacionadas con la biología, sin mucha esperanza. Era consciente de lo complicado que es el mundo de la investigación y no tenía idea alguna sobre la investigación que se desarrollaba en este campo. Gracias por transmitirme vuestra ilusión en aquel momento sobre ésta línea de investigación y seguir haciéndolo durante todos estos años. Gracias, de verdad, por vuestro apoyo, tiempo, guía y consejos.

Agradezco al Dr. Rui D. M. Travasso sus aportaciones y la fructífera colaboración que ha dado como resultado un artículo. Esta colaboración empezó en el *Workshop on Modeling Biological Phenomena from Nano to Macro Scales* realizado en 2018 en el Fields Institute en Toronto, Canadá. Agradezco al Prof. I. Hambleton, director del Fields Institute, su invitación y apoyo durante el Workshop y, también, a la Prof. A. Carpio, organizadora del Workshop. Agradezco al Prof. Charles S. Peskin por ser mi tutor durante la estancia invitada en el Courant Institute of Mathematical Sciences de la New York University y, también, al Prof. Russel Caflisch, director del Courant Institute, por su invitación y hospitalidad. Todo esto no habría sido posible sin la ayuda del programa propio de la Universidad Carlos III para mi estancia. La investigación de esta tesis ha sido financiada por los proyectos de investigación del Ministerio de Economía y Competitividad (ahora FEDER/Ministerio de Ciencia, Innovación y Universidades – Agencia Estatal de Investigación) No. MTM2014-56948-C2-2-P y No. MTM2017-84446-C2-2-R.

Un agradecimiento especial va para todas aquellas personas con las que he compartido mi día a día en la universidad. Hablo de los ratitos a medio día en los que las actividades del gimnasio me daban, paradójicamente, energía para el resto de la jornada. Esto se debe a unos magníficos entrenadores y a la gente con la que, además de sudor, compartí viernes de spá en la universidad. Y, por supuesto, también hablo de compañeros de despacho y de pasillo que me han aconsejado, ayudado y hecho que los días sean mucho mejores. Entre toda la gente alucinante que podría nombrar, me gustaría destacar a Carolina. Esta aventura la hemos empezado, sufrido y disfrutado juntas, y juntas la terminaremos y celebraremos. Tu compañía y amistad ha sido y seguirá siendo esencial, gracias.

Las amistades han sido una pieza clave, a nivel personal. Las matemáticas también me han aportado mucho en este campo: amigos con los que graduarme fue sólo uno entre los grandes momentos vividos y por vivir, y a quienes doy las gracias por ello. Pero antes de oír hablar de teoremas y demostraciones, otro tipo de argumentos menos deductivos se desarrollaban cuando conocí a quien hoy considero amigo, Víctor. Gracias por tus conversaciones y discusiones de las que siempre hay algo que aprender y, sobre todo, gracias por ser un apoyo incondicional para mí. Cierro este párrafo con una amiga a la que tengo mucho que agradecer y que unas líneas dudo que consigan, Elena. Y es que no hay palabras con las que darte las gracias por poder contar siempre contigo, por tu sinceridad y genio que tanto me han ayudado, por las risas y los viajes hechos y pendientes. Por ser única y estar ahí, gracias.

Concluyo los agradecimientos con unas palabras para mi familia. Su apoyo y confianza me han dado los ánimos y el soporte que necesité. Siempre tuve presente la foto de *el mi padrín* de la orla de empresariales dedicada. En ella deseaba que algún día le devolviese el regalo con una foto mía licenciada, también dedicada. Va sin foto, pero el agradecimiento es de corazón. Por último, mi mayor agradecimiento va para mis padres, Pilar y Manuel. Si he llegado hasta aquí es gracias a haberme enseñado con vuestro ejemplo la importancia del esfuerzo, gracias a haberme apoyado, cuidado y hecho la vida más fácil con cada uno de vuestros gestos. Esta tesis va dedicada a vosotros, por haber creído en mí y animado en cada momento, porque la capacidad de superación y cariño que me habéis demostrado merecen ser reconocidos. Muchas gracias, os quiero.

Contenidos publicados y presentados

Esta tesis doctoral incluye el trabajo realizado en el siguiente artículo:

- **Vega R**, Carretero M, Travasso RDM, Bonilla LL (2020) *Notch signaling and taxis mechanisms regulate early stage angiogenesis: A mathematical and computational model* PLOS Computational Biology 16(1): e1006919. `https://doi.org/10.1371/journal.pcbi.1006919`
  - Publicado previamente en bioRxiv: *Notch signaling and taxis mechanisms regulate early stage angiogenesis: A mathematical and computational model* **Rocío Vega**, Manuel Carretero, Rui D.M. Travasso, Luis L. Bonilla. bioRxiv 569897; doi: `https://doi.org/10.1101/569897`

Este artículo, junto con su material suplementario, se presentan en su totalidad en el capítulo 2 y parte del capítulo 5. El resto de capítulos pueden hacer referencia a este trabajo.

También se incluye el siguiente trabajo pendiente de publicación en el capítulo 3:

- *Anomalous Angiogenesis in Retina.* **Rocío Vega**, Manuel Carretero, Luis L. Bonilla.

Contents

List of Abbreviations

AMD	Age-related Macular Degeneration
BM	Bruch's Membrane
CNV	Choroidal Neovasculatization
CPM	Cellular Potts Model
CPU	Central Processing Unit
CSR	Compressed Sparse Row
CUDA	Compute Unified Device Architecture
DOF(s)	Degree(s) Of Freedom
EC(s)	Endothelial Cell(s)
ECM	Extracellular Matrix
FDM	Finite Difference Method
GPU(s)	Graphics Processing Unit(s)
MCTS	Monte Carlo Time Step
NICD	Notch Intracellular Domain
ODE(s)	Ordinary Differential Equation(s)
PCG	Preconditioned Conjugate Gradient
PDE(s)	Partial Differential Equation(s)
RAM	Random Access Memory
RPE	Retinal Pigment Epithelium
TAF	Tumor angiogenic factors
VEGF	Vascular Endothelial Growth Factor

Chapter 1

Introduction

Cancer kills 26.4% of Spanish people. It is the second cause of death, just behind diseases of the circulatory system, 28.3% [1]. The growth of new blood vessels from the existing vasculature in response to chemical signals from a tumor is called tumor-induced angiogenesis and it is closely related to cancer and metastasis. The growth rate of a tumor is considerably increased in its vascular stage compared to its avascular and solid stage, therefore treating cancer turns excessively difficult and the survival rates rapidly decrease [2].

Among diseases that cause disability but not substantial mortality, age-related macular degeneration may cause severe loss of vision or blindness in many people, particularly the elderly. It is projected that 196 million people will be affected by age-related macular degeneration in 2020, increasing to 288 million by 2040 [3], which is likely an underestimation [4]. With age, Bruch's membrane gets thicker and some damaged cells in the retina become inflamed. The secretion of chemical signals from those cells due to their inflammation induces angiogenesis, but the new blood vessels are disorganized and leaky causing the loss of vision.

John Hunter was the pioneer in describing the vessel formation process in 1787 [5], but the first person who coined the word “angiogenesis” was Arthur T. Hertig in 1935 [6]. He was studying the formation of new blood vessel in the primary placenta of the macaque monkey when this word was used for the first time. Years later, in 1971, Judah Folkman hypothesized that tumors emit Tumor Angiogenic Factors (TAF) to attract blood vessels to them [7]. This investigation triggered the research field of angiogenesis in cancer and in 1989 one of the most important angiogenic factors was discovered: the Vascular Endothelial Growth Factor (VEGF). Since then, drugs with antiangiogenic effects have been investigated for cancer, age-related macular degeneration and other diseases, as it is involved in more than seventy different diseases.

However, angiogenesis also occurs in normal and vital processes such as wound healing or the growth of a fetus. The difference between physiological and pathological angiogenic processes is a matter of balance. In a healthy process, angiogenesis develops to its proper extent and then stops, while in pathological processes angiogenesis does not stop or it does not develop sufficiently. Angiogenesis keeps the number of blood vessels needed in balance: few blood vessels cause tissue death, while uncontrolled vascular proliferation can lead to cancer, macular degeneration and other diseases.

Angiogenesis is a complex, multistep and well regulated process where biochemistry and physics are intertwined. The process entails signaling in vessel cells being driven by both chemical and mechanical mechanisms that result in vascular cell movement, deformation and proliferation. In a later stage of angiogenesis, vessel cells rearrange to form lumen and allow the perfusion of the blood inside the sprout. Depending on what induces the angiogenesis, different environments and cells should be considered, for instance in the retina. A detailed review of the processes involved in angiogenesis from the biological point of view is given in section 1.1.

Beyond experimental investigations, mathematical models of angiogenesis try to help in understanding the process and how the relevant mechanisms of angiogenesis interact. The approach of some models focus on a single scale or a single process of those involved to deepen the knowledge about it. Others span multiple scales or the whole process to give an idea about how to prevent or favor angiogenesis. In section 1.2, we briefly review the mathematical models of angiogenesis that have been used to date as well as those when angiogenesis occurs in the retina and models of lumen formation, the late stage of angiogenesis.

A crucial question about modeling is how to integrate the multiple scales and mechanisms present in angiogenesis in a mathematical model. A model is expected to be useful to explore methods for promoting and inhibiting angiogenesis. However, answering this question with this expectation is not a simple task. Assembling all the processes involved with their different time and length scales requires to develop a cellular dynamics model combined with models for the continuum fields. We achieved this objective by developing a hybrid cellular Potts model of early stage angiogenesis, given in chapter 2. In contrast to recent models, this mathematical and computational model is able to explore the role of biochemical signaling and tissue mechanics. A exhaustive description of the results of the numerical simulations complete the chapter 2.

The advantages of discovering the reasons why angiogenesis starts in the retina or inhibitory mechanisms are innumerable. Unraveling the causes of neovascularization in the retina and giving possible solutions for age-related macular degeneration are our motivation to adapt the angiogenesis model of chapter 2 to the retina. In chapter 3, we present the model and the numerical results.

If mathematical models of angiogenesis that incorporate multiple scales and cellular signaling processes are not that common, those that also include lumen formation are almost nonexistent. In chapter 4, we describe two models of lumen formation and their results. The lumen formation in the first model takes place in a already developed sprout.

Although some restrictions in the model make its applications and possibilities limited, its study is convenient to establish the basis of the second proposed model. In this second model, the lumenization occurs while the sprout is developing and the pressure of the blood is involved, following recent experiments of lumen formation during angiogenesis. This model is work in progress, but we believe that showing the preliminary results in chapter 4 may be interesting.

A critical step in the development of a mathematical and computational model is to analyze the viability of its simulations. The simulations of the model in chapter 2 have been carried out thanks to the parallel computing on Graphics Processing Units (GPUs), as well as simulations of chapters 3 and 4. The large amount of square elements of the grid, nodes, cells and sprouts make this type of computation suitable for these models. The way they have been implemented is explained in chapter 5.

Finally, conclusions of this thesis and future work are drawn in the last chapter 6. This chapter highlights and summarizes the research that has been carried out and proposes future extensions and applications of this work.

1.1 Biological background

The process of growing new blood vessels from the existing ones is called angiogenesis. Angiogenesis begins when some cells belonging to a hypoxic or inflamed tissue need oxygen and they are more than 100 μm away from the nearest blood vessel. Those cells are able to activate signaling pathways that lead to the secretion of pro-angiogenic proteins. The vascular endothelial growth factor is one of these proteins and it is necessary and sufficient to start the process of angiogenesis. Present in different isoforms that modify the binding affinity, VEGF diffuses in the tissue and is able to bind to Extracellular Matrix (ECM) components, forming a well defined spatial concentration gradient in the direction of increasing hypoxia [8, 9]. When the VEGF molecules reach an existing vessel, they promote the dwindling of the adhesion between vessel cells and the growth of newer vessel sprouts. VEGF also activates the tip cell phenotype in the vessel Endothelial Cells (ECs) [10]. The tip cells grow filopodia rich in VEGF receptors, pull the other ECs, open a pathway in the ECM, lead the new sprouts and migrate in the direction of increasing VEGF concentration [11]. Branching of new sprouts occur as a result of crosstalk between neighboring ECs [12].

As the new sprouts grow, ECs have to alter their shape to form a lumen connected to the initial vessel that is capable of carrying blood [13–17]. Moreover, in order for the blood to be able to circulate inside the new vessels, the growing sprouts have to merge either with each other or with existing functional mature vessels [18]. The process by which sprouts meet and merge is called anastomosis [18–22]. A scheme of processes and elements involved in angiogenesis is shown in Fig. 1.1.

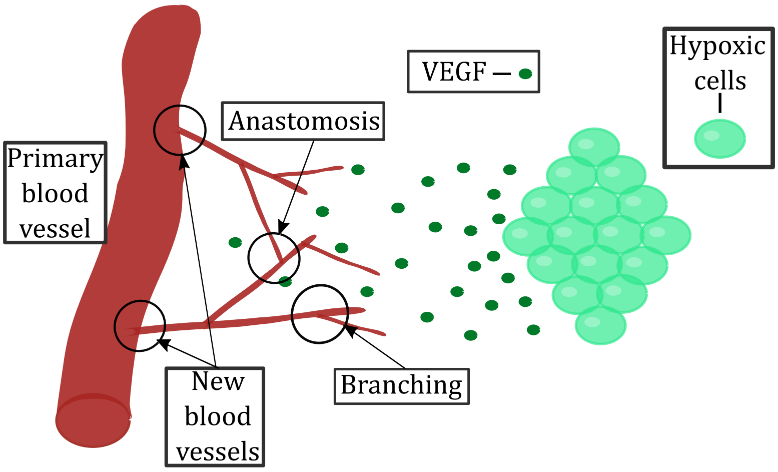

Figure 1.1: **Angiogenesis scheme**

Nascent sprouts are then covered by pericytes and smooth muscle cells, which provide strength and allow vessel perfusion. Poorly perfused vessels may become thinner and their ECs, in a process that inverts angiogenesis, may retract to neighboring vessels leading to more robust blood circulation [23, 24]. Thus, the vascular plexus remodels into a highly organized and hierarchical vascular network of larger vessels ramifying into smaller ones [25].

Growth factors are therefore the main reason for angiogenesis to begin [11]. The movement of the ECs in response to a chemical stimulus is called chemotaxis. However, cell migration is not only due to chemotaxis. The predisposition of cells to migrate up gradients of substrate rigidity is called durotaxis [26]. The traction forces exerted by the cells on the ECM cause its deformation and consequent hardening by the collagen fibers. Other reason for cells to migrate is haptotaxis which is the directional motility of cells usually up a gradient of cellular adhesion sites or substrate-bound chemoattractants.

The movement of endothelial cells is organized and guided by a cell which has a tip cell phenotype. When an EC has the tip cell phenotype, which is triggered by the binding of VEGF to VEGF Receptor 2, VEGFR2, its membrane becomes rich in Delta-4 transmembrane proteins [12,27]. These proteins bind the Notch transmembrane proteins in the neighboring cells triggering the Notch signaling pathway. The activation of this pathway down-regulates VEGFR2 and Delta-4, forcing the neighboring cells not to be in the tip cell phenotype, and to acquire the stalk cell phenotype [28]. Stalk ECs are characterized by a higher proliferation rate [11] triggered by both VEGF and by the tension exerted on them by the tip cell [29]. The sprouts are able to grow due to proliferation of the stalk ECs.

The ECs can interchange dynamically their phenotypes from tip to stalk. In fact, in the growing sprout, the stalk ECs behind the tip cell are often able to overtake the tip cell and to take its place, thereby becoming tip cells and driving sprout elongation [30, 31]. This dynamic behavior ensures that there is always a cell at the front of the sprout with the tip phenotype capable of exerting a contractile force on the matrix, degrading and remodeling matrix fibers and opening a pathway for the sprout to grow.

EC metabolism is strongly connected with this cycling dynamics at the tip of sprouts [32] and it is determinant to vascular patterning, pruning and sprouting [33–35]. The ability of ECs to rearrange themselves is essential for vessel remodeling [23]. Moreover, this dynamics at the tip is only possible due to the regulation of VE-cadherin expression in ECs by the Notch signaling pathway [30, 36, 37]. When the Notch-driven tip-stalk pattern is absent (due to very high VEGF levels, for example) the EC rearrangement dynamics stops [37]. In that case the vessels become thicker and sprouting is severely hampered. Hence, the Notch signaling pathway is pivotal in determining the morphology of blood vessel networks.

Importantly, the dynamics of the ECs' phenotypes in a growing sprout can be rather complex. While at moderate values of VEGF lateral inhibition by tip ECs can be observed [38], at higher VEGF concentrations the situation is different. Recently it has been experimentally observed that high levels of VEGF lead to synchronization of phenotypes between cells at the sprout [39].

Jagged-1 is a ligand of Notch and competes with Delta-4 in angiogenesis [40]. Experiments have shown that when the lateral inhibition pattern induced by Delta-Notch signaling is present, the levels of Jagged-1 follow the EC phenotype: they are lower in tip cells and higher in stalk cells (contrary to what happens with the levels of Delta-4) [41]. However, ECs are able to control independently the levels of Jagged-1 (for example by reaction with proteins of the Fringe family [40]), and therefore they are able to control the sensitivity to Notch-mediated lateral inhibition. Moreover, Jagged-1 also plays an important role in making the Notch mechanism capable of lateral induction, whereby a stalk EC may induce its neighbors to acquire a phenotype equal to its own [42]. For these motives, it is extremely important to understand the implications of Jagged-1 levels in sprouting angiogenesis. A scheme of how Notch signaling pathway interferes in angiogenesis is shown in Fig. 1.2.

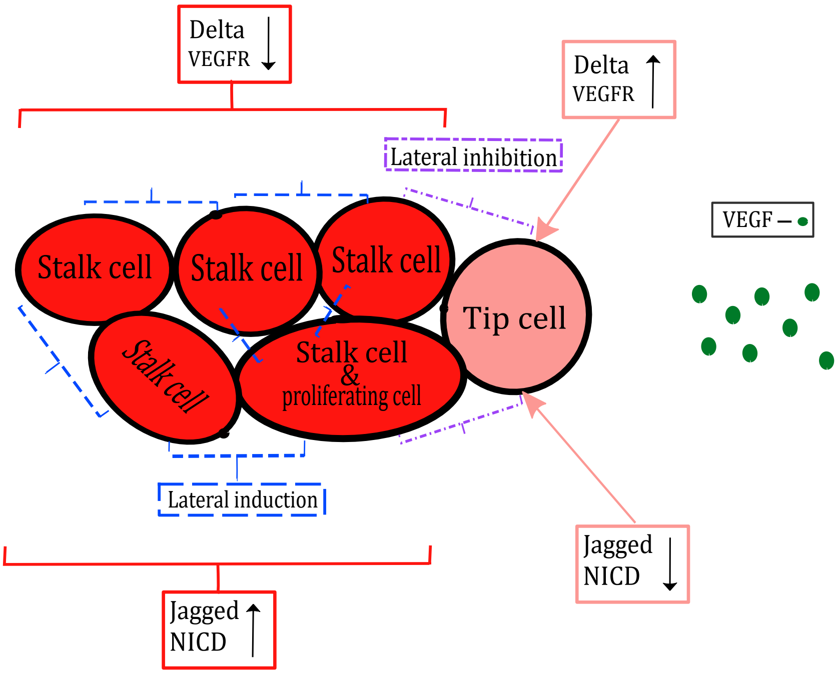

Figure 1.2: **Notch signaling scheme**

To sum up, angiogenesis is a multi-step, complex and well regulated process where biochemistry and physics are intertwined; with signaling in ECs being driven by both chemical and mechanical mechanisms that result in EC proliferation, mechanical deformation and cell movement. This ubiquitous phenomenon in health and disease of higher organisms [43], plays a crucial role in the natural processes of organ growth and repair [44], wound healing [45], or inflammation [46]. Angiogenesis imbalance contributes to numerous malignant, inflammatory, ischemic, infectious, and immune diseases [2,44], such as cancer [7,47–50], rheumatoid arthritis [51], endometriosis [52,53], diabetes [54] and neovascular age-related macular degeneration (AMD) [55].

Exudative or wet AMD is characterized by a breakdown of the blood-retina barrier: blood vessels grow from underneath the macula and leak blood and fluid into the retina [55,56]. These blood vessels and their leaking may form scars leading to permanent loss of central vision. Diagnosis of wet AMD [56] has improved with important non invasive techniques such as optical coherence tomography [57,58] or, quite recently, transscleral optical phase imaging [59]. The retina contains many membranes and tissue layers that make imaging cells and understanding pathologies difficult. The growth of blood vessels in the retina is well documented in pathological cases, such as wet AMD, and in normal cases, such as retinal vascularization in fetuses and newborns [60–63]. In these cases, blood vessels grow out of a primary vessel. Retinal angiogenesis adds a complex geometry to the process.

In wet AMD, negative control mechanisms are breached, angiogenic sprouts issue from choroid blood vessels, cross the Bruch's Membrane (BM), pass Retinal Pigment Epithelium (RPE) cells and knock down photoreceptors producing loss of central vision [63]. Under normal circumstances, oxygen and nutrients diffuse from the choroid vascular layer through the thin BM and the layer of RPE cells to reach photoreceptors. Inversely, RPE process photoreceptor debris, including shed photoreceptor outer segments, pass it through the BM, and the debris is removed by the choriocapillaries in the choroid; see the left panel of Fig. 1.3. Incomplete processing of the debris produces deposits on the RPE layer called drusen. Drusen deposits thicken the BM and create a barrier that interferes with the normal situation. They decrease the diffusion of oxygen and nutrients from the choroid to the photoreceptors and the RPE in one direction, and decrease the removal of debris by the choriocapillaries into the other direction [64]. While this dry AMD produces some loss of vision (severe in the case of geographical atrophy of RPE [65]), it also leads to relative hypoxia within retinal layers. In response, the RPE secrete proangiogenic factors, such as VEGF and vasculogenic and inflammatory cytokines, that go into the choroidal space. This may start angiogenesis thereby producing Choroidal Neovascularization (CNV); see the right panel of Fig. 1.3. CNV vessel sprouts may penetrate the BM and remain underneath the RPE layer (type 1 or 'occult' CNV), or surpass it and go through the outer retina (type 2 or 'classic' CNV). In the later condition, sprouts may leak blood and fluid that eventually produce scars and the death of photoreceptors, which signals the wet phase of AMD [65]; see also sketch in Fig. 1 of Ref. [64].

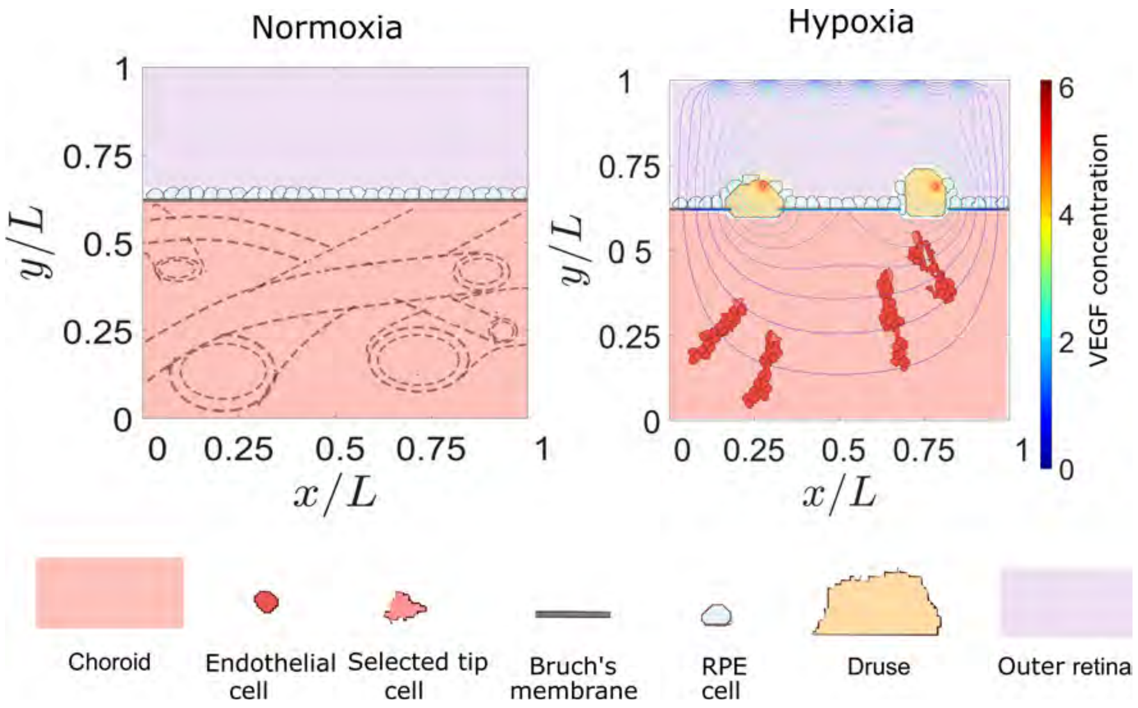

Figure 1.3: **Retina scheme**

Lumen weakening in capillaries may cause blood leaking from the sprouts in the retina [62]. Once a sprout is lumenized, blood is allow to perfuse but also the cells belonging to the sprout are polarized. The surface of the cell membrane that faces inward to the lumen is called apical membrane. The basolateral membrane is the membrane oriented away from the lumen. How the vascular lumen formation occurs is still being discussed, but the study of lumenization in zebrafish and mice has uncovered various mechanisms: budding, cord hollowing and cell hollowing [66, 67].

When a sprout branches out of a lumenized vessel and its luminal space is continuously connected to the lumen of the parent vessel, this is called budding. It could be extend up to the tip cell and the apical and basal polarity is maintained [66, 67].

During cord hollowing mechanism, the lumen of the sprout does not come from the parent vessel. Instead, it is formed by cell polarization and vacuolization. The formation of lumen due to vacuolization is the result of secretion of vacuoles filled with ECM fluids that form inside the cells [66, 67].

Cell hollowing mechanism occurs when the sprout is only one cell wide, and therefore it is similar to a chain of cells. Vacuolization or a mechanism similar to budding can take place in order to form the lumen [66, 67].

A sketch of these three mechanisms can be found in Figs. 2 and 3 of [67] and also in Fig. 4 of [66].

Regarding the lumen formation in angiogenesis, Gebala *et al.* highlighted the role of blood flow in the remodelling of vascular networks *in vivo* [16]. They suggested that lumen expansion during sprouting angiogenesis *in vivo* is motivated by blood flow through a process they termed inverse blebbing. During inverse blebbing, ECs react to high external pressure by inducing spherical deformations of the apical membrane of ECs [16].

1.2 State of the art

In order to elucidate the mechanisms that govern angiogenesis, several mathematical models have been developed over the last few years. The greatest challenge of these models is to integrate all the relevant biological information in angiogenesis in order to understand the whole process. The complexity of angiogenesis is the reason why most models focus on a single scale out of the multiple scales comprising it, which range from gene transcription and protein synthesis, passing through cellular dynamics and reaching the level of organization of tissues and organs.

Early models in angiogenesis described endothelial cells and the blood vessel network as continuous density fields, thus omitting the structural details of the network that the sprouts form. Since these models, the field has evolved significantly. Currently, we could classify the models that describe evolving angiogenesis networks into three large groups: Tip cell models, phase field models and cellular Potts models [68].

1.2.1 Angiogenesis

Tip cell models

Tip cell models of angiogenesis assume that the tip cell establishes the path that the stalk cells of the sprout should follow. These models ignore length scales smaller than a capillary and consider tip cells to be point particles. Then blood vessels advancing toward the hypoxic region are simply tip cell trajectories.

The first model of cell migration by chemotaxis was presented by Stokes and Lauffenburger in 1991 [69, 70]. The stochastic mathematical model proposed for the random motility and chemotaxis of tip cells considers tip cells to be particles of unit mass. The random walk describing the cell velocity under random motility conditions takes into account random motion accelerations, friction in cell movement and a force representing the directional bias imposed by chemotaxis. The cell density of each sprout follows a rate equation whose coefficients depend on the stochastic equation for the tip cell.

In 1998, Anderson and Chaplain proposed a continuous and a discrete two-dimensional models of tumor-induced angiogenesis. The continuous model considers three dependent variables of position and time: the endothelial cell density, the concentration of tumor angiogenic factors and the concentration of fibronectin. They describe macroscopic properties represented by scalar fields whose evolution is given PDEs. The movement of ECs is subject to random motility, chemotaxis and haptotaxis. The discrete model is a random walk with transition probabilities derived from the discretization of the continuous model. Sprout branching occurs according to probabilistic rules that take into account the EC density, maturity of sprouts and space available at each point of the domain. When an advancing tip meets an existing blood vessel or another tip, it inactivates, as its sprout fuses with the other (anastomosis). Anderson and Chaplain's pioneering paper is a breakthrough in tumor-induced angiogenesis modeling. However, the facts that transition probabilities derived from discretization of partial differential equations may become negative [71], and that the tip can only move through mesh points make the resulting network of blood vessels unrealistic.

Years later, in 2004, Plank and Sleeman [72] proposed a model in which cells position is not restricted to positions in the mesh and cells follow a circular random walk. The movement of tip cells is characterized by time dependent functions for their velocity and angular direction. This difference with Anderson and Chaplain model makes their results have a greater agreement with empirical observations.

The last two described models as well as some later tip cell models [73–75] consider branching and anastomosis and integrate a random walk motion of individual blood vessels with a continuum description of fields that determines cell motion. These ideas inspired Capasso and Morale [76] in their hybrid model of Langevin-Ito stochastic equations. They considered reaction-diffusion equations for the continuum fields, migration by chemotaxis and haptotaxis and also branching and anastomosis. Using the stochastic equations, they derived a continuum equation for the tip cells density, although branching and anastomosis present in the stochastic model are not taken into account in the continuum equations.

This inconvenient was solved by Bonilla, Capasso, Alvaro, Carretero, Terragni *et al* [77–81]. They proposed a hybrid model that includes branching, extension of the sprouts, chemotaxis in response to a generic TAF, haptotaxis in response to the fibronectin gradient, and anastomosis. The extension of the ith capillary sprout is given by the nondimensional Langevin-Ito stochastic equations

$$
\begin{aligned}
d\mathbf{X}^i(t) &= \mathbf{v}^i(t)\,dt \\
d\mathbf{v}^i(t) &= \beta\left[-\mathbf{v}^i(t) + \mathbf{F}\big(C(t,\mathbf{X}^i(t))\big)\right]dt + \sqrt{\beta}\,d\mathbf{W}^i(t) \qquad (1.2.1)
\end{aligned}
$$

where $\mathbf{X}^i(t)$ is the position, $\mathbf{v}^i(t)$ the velocity and $C(t,\mathbf{x})$ is the VEGF concentration that obeys a PDE containing diffusion and degradation. The branching process is based on a probability depending on the VEGF concentration. Additionally, tips stop moving at the time and point where they collide with an existing blood vessel, process that simulate anastomosis. Densities of active vessel tips and the vessel tip flux can be obtained by taking the average of several simulations where the equations are solved using numerical methods

$$
\begin{aligned}
p_{\mathcal{N}}(t,\mathbf{x},\mathbf{v}) &= \frac{1}{\mathcal{N}}\sum_{\omega=1}^{\mathcal{N}}\sum_{i=1}^{N(t,\omega)} \delta_{\sigma_x}(\mathbf{x}-\mathbf{X}^i(t,\omega))\,\delta_{\sigma_v}(\mathbf{v}-\mathbf{v}^i(t,\omega)), \qquad (1.2.2)\\
\tilde{p}_{\mathcal{N}}(t,\mathbf{x}) &= \frac{1}{\mathcal{N}}\sum_{\omega=1}^{\mathcal{N}}\sum_{i=1}^{N(t,\omega)} \delta_{\sigma_x}(\mathbf{x}-\mathbf{X}^i(t,\omega)), \qquad (1.2.3)\\
\mathbf{j}_{\mathcal{N}}(t,\mathbf{x}) &= \frac{1}{\mathcal{N}}\sum_{\omega=1}^{\mathcal{N}}\sum_{i=1}^{N(t,\omega)} \left|\mathbf{v}^i(t,\omega)\right| \delta_{\sigma_x}(\mathbf{x}-\mathbf{X}^i(t,\omega)). \qquad (1.2.4)
\end{aligned}
$$

As $\mathcal{N} \to \infty$, the ensemble averages tend to the tip density $p(t,\mathbf{x},\mathbf{v})$, the marginal tip density $\tilde{p}(t,\mathbf{x})$, and the tip flux $\mathbf{j}(t,\mathbf{x})$, respectively.

A deterministic description of the tip density is achieved through a Fokker-Plank integro-differential equation with source terms. One of the most important novelties that they contribute is the term in this equation that represents the geometric anastomosis of the stochastic model. After comparing the density of active tips calculated as an average hundreds of simulations of the stochastic model with the one calculated by the deterministic description, they obtain quantitatively and qualitatively similar results.

In the numerical simulations, it is observed that after an initial stage the density of active tips advances towards the tumor as a two-dimensional pulse whose shape and speed are slowly variable. They determined that a longitudinal section of this pulse is a solitonlike wave whose shape and speed, given by collective coordinates, are described by ordinary differential equations. Numerical simulations show that the soliton is an attractor of the integro - differential equation for the density of active tips.

Phase field models

A phase field model is a continuum model that is able to describe vascular networks. One of the main works in angiogenesis using a phase field model has been developed by Travasso *et al* [82,83]. In their model, ϕ is an order parameter that describes proliferative and non-activated cells and its value indicates the element and condition considered at certain point of the domain

$$\phi(t,\mathbf{x}) = \begin{cases} -1 & \text{if } \mathbf{x} \text{ is in ECM, outside a capillary} \\ +1 & \text{if } \mathbf{x} \text{ is inside a capillary} \\ > 1 & \text{if } \mathbf{x} \text{ is in an area of high proliferation of ECs,} \\ & \text{leading to the widening of the capillary} \\ 0 & \text{if } \mathbf{x} \text{ is at a capillary wall, made out of stalk cells} \end{cases} \tag{1.2.5}$$

A continuum equation for the phase field $\phi(t,\mathbf{x})$ is coupled to a reaction-diffusion equation for the VEGF, where the mobility of ECs, the proliferation rate and the width of the capillary wall are taken into account. Discrete equations are added to the model for activated tip ECs and criteria to distinguish them. Tip cells consume the angiogenic factors and they move in response to these proteins with certain velocity that is proportional to the VEGF gradient if the VEGF gradient at the tip cell position is greater than a threshold. Stalk cells are able to change their phenotype to tip cells if some conditions related to the VEGF are met as well as a tip cell is able to return to the stalk cell state.

Phase field models can include other features such as elasticity and a force at the vessel tip, model presented by Santos-Oliveira *et al* [29], and haptotaxis, suggested by Vilanova *et al* [84]. Both models have been included in a review paper years later [85]. Given a blood vessel network generated by a phase field model, it is also interesting to study the relation between the morphology, blood supply and obstructions as Torres Rojas *et al* have done [86].

Cellular Potts models

The models of angiogenesis discussed in the two previous subsections do not describe the shape of cells or how it changes during vessel formation. However, we need to consider models that capture dynamics of the cell for a more precise analysis of the role of cell mechanics and adhesion in angiogenesis, since ECs migrate by durotaxis and haptotaxis too. Thus treating cells as point particles of tip cells model or a limited distinction between stalk and tip cells of phase field models are not enough and we need to add extra dynamics for them [87].

A Cellular Potts Model (CPM) uses a Monte Carlo dynamics coupled to continuum fields (elastic fields, VEGF, $\dots$) to be capable of dynamically capturing the shape of the cell. Based on the Metropolis algorithm, this lattice-based computational modeling method allows to simulate the collective behavior of cells and ECM [88, 89].

Bauer *et al* [90] developed the first CPM of angiogenesis. In their model, each site of the lattice, $\mathbf{x}$, belongs to an element τ that can be ECs, matrix fibers, tissue cells and interstitial fluid. Each entity of those elements is associated with a unique identifying number, denoted by σ, and the lattice sites of the same entity have assigned the same identifying number allowing the model for instance to distinguish one EC from another. At every Monte Carlo Time Step (MCTS), the cell surface, represented by connected lattice vertices, is updated depending on a set of cell behavior rules such as the target cell shape and size that are translated in an energy change ΔH. In order to do that, a lattice site $\mathbf{x}$ is randomly selected to copy its identifying number $\sigma(\mathbf{x})$ to one of its neighbors $\mathbf{x}'$. After calculating again the total energy H of the system, the copy is accepted if the total energy has been reduced and with the probability $e^{-\beta\Delta H}$ otherwise. The energy described by Bauer *et al* is

$$H = \sum_{\text{sites}} J_{\tau,\tau'}(1-\delta_{\sigma\sigma'}) + \sum_{\text{cells}} \gamma_\tau (a_\sigma - A_\sigma)^2 - \sum_{\text{cells}} \sum_{\text{sites}} \mu_\sigma C(t,\mathbf{x}). \tag{1.2.6}$$

where the first term represents the adhesion between elements, the second term is the area constraint and third one represents chemotaxis and C is the VEGF concentration that satisfies a reaction-diffusion equation. Proliferation is considered in this model and the target area is adapted for the cells undergoing mitosis. Their main objective was to investigate the role of a heterogeneous ECM, containing tissue-specific fibers, fluid, and cells, in sprout formation. A remarkable feature of the model is the representation of the extracellular space in an explicit way rather than the usual continuum field.

On the basis of this model, Mahoney *et al* [91] looked for new strategies to interrupt tumor-induced angiogenesis by adding the effects of oxygen and blood flow to the model.

The two previous CPMs do not incorporate cell mechanics. Van Oers *et al.* [92] developed a CPM for vasculogenesis that includes durotaxis through an ECM strain-dependent term in the Hamiltonian for the energy. This term favors cell extension in the direction of the principal strain. Finite elements are used to calculate the traction force exerted by ECs on the ECM. However, this work models vasculogenesis, not angiogenesis.

1.2.2 Notch signaling models

Numerous mathematical models of angiogenesis study the growth of blood vessels and irrigation using continuum methods, cellular automata, and hybrid methods [29,69,72,77, 78,80,82,83,87,92–103]. Cellular Potts models [88,89] of angiogenesis and vasculogenesis have been particularly successful in capturing vascular cell shape [90], vascular structure [102,104] and in integrating the role of ECM mechanics and structure [92,105–107] in the development of the vasculature.

However, many of these models use simplified models of the Notch pathway to determine the separation between sprouts [18,83,87]. Very detailed models of the Notch signaling pathway that integrate the dynamics of filopodia growth and of anastomosis have been also developed [10,108]. The model of Bentley *et al.* [10] was the first one in suggesting that high levels of VEGF lead to synchronization of phenotypes between cells at the sprout. The ECs in a sprout under high VEGF levels initiate acquiring the tip cell phenotype simultaneously, and then all simultaneously trigger the lateral inhibition by the Delta-Notch signaling, losing the tip phenotype and moving towards the stalk phenotype, only for the process to start again. Synchronized oscillatory behavior in Delta-4 levels in EC cells has been observed under these conditions [39]. In this way, high VEGF hinders the symmetry breaking needed for the lateral inhibition to take place in the sprout. These detailed models shed also light into the regulation of VE-Cadherin by Delta-Notch [30,37] and into the coupling between EC metabolism, Delta-Notch and EC rearrangement dynamics at the tip [32].

Recent mathematical models of Notch signaling in angiogenesis have also predicted states where the cells in the sprout are in a third intermediate state and neither in the tip nor in the stalk phenotype [109, 110]. The Jagged-1 transmembrane protein is an important partner in the regulation of the Notch signaling in angiogenesis, and its introduction in the computational models permit to predict these intermediate EC phenotypes [110–113].

Mathematical models of angiogenesis should integrate the knowledge of Delta-Notch-Jagged signaling with the dynamics of EC organization in a sprout to better understand how the communication between ECs in angiogenesis is mediated by Jagged-1.

1.2.3 Models of angiogenesis in the retina

The complexity of the retinal structures involved in AMD makes the development of mathematical models in this field certainly difficult. While there are many mathematical and computational models describing the development of retinal vascularization, less work has been devoted to such models for AMD; see e.g., [114].

Early modeling research on CNV focus on relating the blood flow in the CNV to that in the underlying choriocapillaries in an appropriate two dimensional (2D) geometry [115]. Darcy's law for a porous medium is used to model flow in choriocapillaries and in blood vessels that connect them to the CNV. Changes in the flow in the connecting vessels strongly influence the flow through the CNV and controling the connecting vessels may be used to block the flow in the CNV, with beneficial effects for wet AMD [115]. A similar idea but using the incompressible Navier-Stokes equation has been recently used to study drug delivery across the blood-retina barrier [116]. These studies consider fixed choroid and CNV networks, ignoring the development and progression of the latter.

To account for the formation and expansion of the CNV, Shirinifard *et al* have used a 3D cellular Potts model of the choroid and outer retina [117]. They conclude that failures in cellular adhesion determine the formation and expansion of CNV. Cells include tip and stalk ECs, cells at RPE and BM, photoreceptor cell outer and inner segments, ECM and fluid regions. Continuum equations model media surrounding cells, VEGF, oxygen and matrix metalloproteinases and are coupled to the Potts Hamiltonian that is updated using a modified Metropolis algorithm. EC chemotaxis and haptotaxis are implemented. Stalk cells may increase their volume and proliferate, BM cells may decrease their volume and die. Different cells have different adhesion parameters. The model does not include blood flow, signaling pathways and change of EC phenotype, or drusen [117].

1.2.4 Models of lumen formation

The uncertainty about the process of lumen formation do not favor the development of mathematical models describing this mechanism. The main work to highlight is due to Boas and Merks [17]. They present a 2D CPM of lumen formation in a preformed sprout. It is assumed that sprouting and lumen formation are separated in time so some cells are placed in rails of "Y" shape before the lumenization starts. Since it is a 2D model, the simulations represent a cross section of the vessel showing local mechanisms driving lumen formation. This 2D model is computationally more efficient than a 3D model [17].

The entities considered in the CPM are cytoplasm, apical and basolateral membranes, vesicle, vacuole, ECM fluid, luminal fluid and ECM. The Hamiltonian takes into account the area constraint term and a adhesion term. Different entities have a different target area and adhesion parameters between them. The element outside the rails is ECM, it is ECM fluid inside the rails, and the adhesion parameter between these entities is high enough not to allow interaction between them. In that way, the ECs separate from each other using either cell repulsion (due to the polarization of cells, or vacuolization, or both) to stick to the walls of the rails and leave space between them [17]. The authors discuss which mechanism is better and how the lumen formation is produced with different cell arrangements in the rails [17].

Chapter 2

Notch signaling and taxis mechanisms regulate early stage angiogenesis: A mathematical and computational model

During angiogenesis, new blood vessels sprout and grow from existing ones. This complex process involves several time scales and complicated interactions between biochemical and biomechanical mechanisms. The regulating effect of Delta-Notch-Jagged is a essential part in the sprouting dynamics and, in order to be described, we need to integrate dynamical models that take into account the Notch signaling proteins with a CPM that takes into account cell shape, movement and proliferation. In this chapter, we carry out this integration process for angiogenesis in the early stage, before sprouts form a lumen, become perfused and can regress. We use a CPM that incorporates cell motion following increasing gradients of VEGF (chemotaxis), of adhesion to substrate (haptotaxis) and of substrate stiffness (durotaxis), as well as a model of cell splitting and proliferation that uses an unsupervised machine learning algorithm, and the Notch signaling pathway. This model will permit to explore the relative importance of mechanical, chemical and cellular cues in angiogenesis.

This chapter consists of three main sections: Mathematical Model, Results and Discussion. The section Mathematical Model, 2.1, describes the CPM coupled with the Delta-Notch-Jagged dynamics. In the section Results, 2.2, we present the results of the simulations and how Jagged-1 determines sprouting dynamics. Finally, in the last section Discussion, 2.3, we draw the conclusions of the chapter.

2.1 Mathematical model

The mathematical model consists of a CPM in which the dynamics of the Notch signaling pathway in endothelial cells selects tip and stalk ECs. Tip ECs move by chemotaxis, haptotaxis and durotaxis and stalk cells proliferate. Vessel branching and anastomosis appear as a result of combined cell signaling, mechanical and chemical taxis.

2.1.1 Cellular Potts model

Square grid

We consider a square domain Ω of side L with grid points (x_i, y_j), where $x_i = i\,h$, $y_j = j\,h$ with $i, j = 0, \ldots, M-1$, $h = L/(M-1)$, and M is the number of nodes on a side of the square. The square contains $M \times M$ grid points and $(M-1)^2$ elementary squares (pixels), each having an area $L^2/(M-1)^2$. To enumerate nodes, we use left-to-right, bottom-to-top order, starting from node 0 on the bottom left corner of the square and ending at node M^2-1 on the rightmost upper corner. In numerical simulations, we use $L = 0.495$ mm.

Objects, spins and Metropolis algorithm

Pixels $\mathbf{x}$ can belong to different objects Σ_σ, namely ECs and ECM. The field (called spin in a Potts model) $\sigma(\mathbf{x})$ denotes the label of the object occupying pixel $\mathbf{x}$ [88]. Each given spin configuration for all the pixels in the domain has an associated energy $H(\{\sigma(\mathbf{x})\})$ to be specified below. At MCTS t, we select randomly a pixel $\mathbf{x}$, belonging to object Σ_σ, and propose to copy its spin $\sigma(\mathbf{x})$ to a neighboring (target) pixel $\mathbf{x}'$ that $\sigma(\mathbf{x}') \neq \sigma(\mathbf{x})$. The scheme of Fig. 2.1 may help to understand the labels involved in the Metropolis algorithm. The proposed change in the spin configuration (spin flip) changes the configuration energy by an amount $\triangle H|_{\sigma(\mathbf{x})\to\sigma(\mathbf{x}')}$, and it is accepted with probability (Metropolis algorithm) [88, 92]

$$P\left(\sigma(\mathbf{x}) \to \sigma(\mathbf{x}')\right)(t) = \begin{cases} e^{-\Delta H|_{\sigma(\mathbf{x})\to\sigma(\mathbf{x}')}/T}, & \Delta H|_{\sigma(\mathbf{x})\to\sigma(\mathbf{x}')} > 0; \\ 1, & \Delta H|_{\sigma(\mathbf{x})\to\sigma(\mathbf{x}')} \leq 0. \end{cases} \tag{2.1.1}$$

The temperature $T > 0$ is measured in units of energy and it is related to an overall system motility. We have selected $T = 4$ in our simulations.

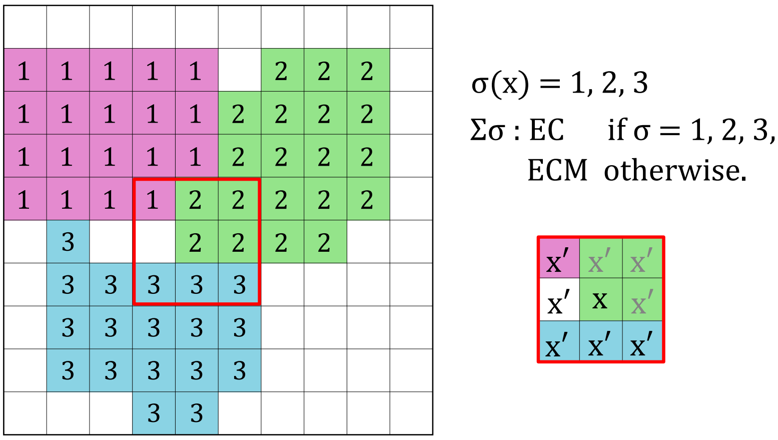

1	1	1	1	1		2	2	2	
1	1	1	1	1	2	2	2	2	
1	1	1	1	1	2	2	2	2	
1	1	1	1	2	2	2	2	2	
	3			2	2	2	2		
	3	3	3	3	3				
	3	3	3	3	3				
	3	3	3	3	3				
			3	3					

Figure 2.1: **Example of a simplified domain for the CPM.** $\sigma(\mathbf{x})$ denotes the label of the object occupying pixel $\mathbf{x}$. Objects, Σ_σ, are ECs and ECM. The zoomed area shows the randomly selected pixel, $\mathbf{x}$, and its neighbors, $\mathbf{x}'$, marked in black those with whom the change could be made.

Energy functional

The energy functional H is

$$\begin{aligned} H \;=\; & \sum_{\sigma} \rho_{\text{area}} \left(\frac{a_\sigma - A_\sigma}{A_\sigma} \right)^2 + \sum_{\sigma} \rho_{\text{perimeter}} \left(\frac{p_\sigma - P_\sigma}{P_\sigma} \right)^2 + \sum_{\sigma} \rho_{\text{length}} \left(\frac{l_\sigma - L_\sigma}{L_\sigma} \right)^2 \\ & + \sum_{\mathbf{x},\mathbf{x}'} \rho_{\text{adh}}^{\Sigma_\sigma,\Sigma_{\sigma'}} \left(1 - \delta_{\sigma,\sigma'}\right) + H_{\text{durot}} + H_{\text{chem}}. \end{aligned} \tag{2.1.2}$$

Here the three first terms are sums over cells and the fourth one sums over all pixels. We have

- a_σ is the area of the cell σ, A_σ is the target area and ρ_{area} is the Potts parameter which regulates the fluctuations allowed around the target area. There are two cell types: non-proliferating tip and stalk cells with $A_\sigma = 78.50\,\mu\text{m}^2$ and proliferating cells with double target area, $A_\sigma = 157\,\mu\text{m}^2$. The target radius of a proliferating cell is $\sqrt{2}$ times that of a non-proliferating cell.

- p_σ is the perimeter of the cell σ, P_σ is the target perimeter and $\rho_{\text{perimeter}}$ is the Potts parameter which regulates the fluctuations allowed around the target perimeter. The target perimeters are $P_\sigma = 31.4\,\mu\text{m}$ for non-proliferating cells, and thrice this, $P_\sigma = 94.2\,\mu\text{m}$, for proliferating cells.

- l_σ is the length of the cell σ, $L_\sigma = 49.5\,\mu\text{m}$ is the target length of nonproliferating cells, $L_\sigma = 70\,\mu\text{m}$ is the target length of proliferating cells, and ρ_{length} is the Potts parameter which regulates the fluctuations allowed around the target length. We define the length of the cell from the longest axis of an ellipse that has the same moment of inertia as the cell. The inertia tensor per unit cell area is [118]

  $$I_{ij}(\sigma) = \frac{1}{N_\sigma} \sum_{\mathbf{X} \in \sigma} (|\mathbf{X}|^2 \delta_{ij} - X_i X_j), \quad i,j = 1,2, \quad \mathbf{X} = \mathbf{x} - \frac{1}{N_\sigma} \sum_{\mathbf{y} \in \sigma} \mathbf{y}, \tag{2.1.3}$$

  where N_σ is the number of pixels in cell σ and the distances $\mathbf{X}$ in the inertia tensor are measured from the center of mass of the cell. Let us now consider an ellipse whose axes have lengths $2a$ and $2b$ ($a \geq b$). Its inertia tensor per unit area defined as in Eq. (2.1.3) has eigenvalues $b^2/4$ and $a^2/4$. Thus, a is twice the square root of the largest eigenvalue of the inertia tensor,

$$a = \sqrt{2\left[I_{11} + I_{22} + \sqrt{(I_{11} - I_{22})^2 + 4I_{12}^2}\right]}, \quad l_\sigma = 2\,a(\sigma). \tag{2.1.4}$$

We define the length of the cell σ as $2a$, where a, given by Eq. (2.1.4), is calculated from the inertia tensor per unit area of Eq. (2.1.3). See also [119].

- The Potts parameter $\rho_{\text{adh}}^{\Sigma_\sigma,\Sigma_{\sigma'}} \geq 0$ is the contact cost between two neighboring pixels. The value of this cost depends on the type of the object to which the pixels belong (cell or medium). Since $\delta_{\sigma,\sigma'}$ is the Kronecker delta, pixels belonging to the same cell do not contribute a term to the adhesion energy.

- The net variation of the durotaxis term H_{durot} is [92]

$$\begin{aligned}\Delta H_{\text{durot}} &= -\rho_{\text{durot}}\, g(\mathbf{x},\mathbf{x}') \left(h(E(\epsilon_1)) \left(\mathbf{v}_1 \cdot \frac{\mathbf{x}'-\mathbf{x}}{|\mathbf{x}'-\mathbf{x}|} \right)^2 \right. \\ &\quad \left. + h(E(\epsilon_2)) \left(\mathbf{v}_2 \cdot \frac{\mathbf{x}'-\mathbf{x}}{|\mathbf{x}'-\mathbf{x}|} \right)^2 \right),\end{aligned} \tag{2.1.5}$$

where ρ_{durot} is a Potts parameter, $g(\mathbf{x},\mathbf{x}') = 1$ for extensions and $g(\mathbf{x},\mathbf{x}') = -1$ for retractions, ϵ_1 and ϵ_2 and $\mathbf{v}_1$ and $\mathbf{v}_2$ ($|\mathbf{v}_1| = |\mathbf{v}_2| = 1$) are the eigenvalues and eigenvectors of the strain tensor ϵ_T, respectively. They represent the principal strains and the strain orientation. ϵ_T is the strain in the target pixel for extensions, and the strain in the source pixel for retractions. $h(E) = 1/\left(1 + \exp\left(-\omega\left(E - E_\theta\right)\right)\right)$ is a sigmoid function with threshold stiffness E_θ and steepness ω. $E(\epsilon) = E_0\left(1 + (\epsilon/\epsilon_{\text{st}})1_{\epsilon\geq 0}\right)$ is a function of the principal strains, in which E_0 sets a base stiffness for the substrate, ϵ_{st} is a stiffening parameter and $1_{\epsilon\geq 0} = \{1,\ \epsilon \geq 0;\ 0, \epsilon < 0\}$: strain stiffening of the substrate only occurs for substrate extension ($\epsilon \geq 0$), whereas compression ($\epsilon < 0$) does not stiffen or soften the substrate. We have used the parameter values: $E_\theta = 15$ kPa, $E_0 = 10$ kPa, $\omega = 0.5$ kPa^{-1}, and $\epsilon_{\text{st}} = 0.1$ [92].

- The variation of the chemotaxis term H_{chem} is

$$\Delta H_{\text{chem}} = -\rho_{\text{chem}}(\mathbf{x},\mathbf{x}')\frac{1}{1+\alpha_{\text{chem}}C(\mathbf{x})}\,[C(\mathbf{x}')-C(\mathbf{x})], \tag{2.1.6}$$

  where $\rho_{\text{chem}}(\mathbf{x},\mathbf{x}') \geq 0$ is a Potts parameter that depends on the type of EC or ECM occupying pixels $\mathbf{x}$ and $\mathbf{x}'$ and will be specified later. Its magnitude is measured by a positive constant ρ^0_{chem}. We have $\alpha_{\text{chem}} = 0.3$ and C is the VEGF concentration in the corresponding pixel.

The values of the Potts parameters are listed in Table 2.1. They are chosen according to those proposed by Bauer *et al.* [90] and Van Oers *et al.* [92] and adjusted so as to make that every term of the net variation of the Hamiltonian have the same order. The perimeter contribution, absent in Refs. [90, 92], is small compared to the other terms in Eq. (2.1.2), so that it only affects the computations in extreme cases (e.g., extremely thin cells, thin cells that stick to the blood vessel). We have added a factor in the chemotaxis term to regulate the fluctuation around the resting VEGF concentration. Note that if α_{chem} is equal to zero, we recuperate the original term of Bauer *et al.* [90]. The proposed value, $\alpha_{\text{chem}} = 0.3$, is small.

Table 2.1: **Dimensionless Potts parameters.**

Param.	ρ_{area}	$\rho_{\text{perimeter}}$	ρ_{length}	ρ_{durot}	ρ^0_{chem}	$\rho_{\text{adh}}^{\Sigma_\sigma,\Sigma_{\sigma'}}$ (cell-cell)	$\rho_{\text{adh}}^{\Sigma_\sigma,\Sigma_{\sigma'}}$ (cell-ECM)
Value	9000	250	7200	25	60000	8.25	16.50

What is the effect of changing the numerical values of the Potts parameters? As said before, with the values in Table 2.1, every term of the net variation of the Hamiltonian has the same order. Variations of 10% or smaller in Potts parameters do not change the outcome of the simulations. Variations larger than 10% with respect to those in Table 2.1 produce unrealistic effects, which are as follows.

- ρ_{area}. Larger increments force cells to reach their target area faster, thereby increasing cell proliferation. The corresponding term becomes more important than the chemotaxis mechanism, which produces slower evolution of vessels toward the hypoxic zone and large clumps of cells in the vessels. Large reductions of this Potts parameter produce irregular cell proliferation and a much larger variety of cell sizes.

- $\rho_{\text{perimeter}}$. Large increments produce round cells, whereas large reductions (up to $\rho_{\text{perimeter}} = 0$) create extremely long and narrow cells stuck to the vessel sprout due to the now dominant effect of the adhesion term.
- ρ_{length}. Large increments produce elongated cells and force them to reach their target length faster. The corresponding term becomes more important than the adhesion or area term. Then appearing isolated cells that take a long time to reach their target area and proliferate (if they are marked for proliferation). Large reductions (up to $\rho_{\text{length}} = 0$) produce rounder cells depending on the values of the other Potts parameters.
- ρ_{durot}. This parameter produces qualitative changes only if it is ten times larger than in Table 2.1. In such a case, durotaxis overwhelms chemotaxis and the perimeter penalty, leading to cells following the stiffness gradients and sticking to each other, which create very irregular vessels.
- ρ_{chem}. Larger increments make chemotaxis dominant. Then cells become bigger and elongated and sprouts extend more rapidly. Sometimes tip cells separate from their sprouts as chemotaxis dominates adhesion effects. Larger reductions produce rounder cells that do not polarize along a specific direction, and produce wider and slower sprouts.
- $\rho_{\text{adh}}^{\Sigma_\sigma,\Sigma_{\sigma'}}$. The adhesion Potts parameter takes on different values for cell-cell and cell-ECM boundaries. If these values become equal (e.g., to 16.5), narrower sprouts are produced and there are cells that escape from them. Larger increments of cell-ECM adhesion, makes very costly for ECM to surround cells, which then stick to each other too much. Larger reductions of cell-ECM produces more elongated cells. Reducing cell-cell adhesion favors cells sticking to each other and acquiring

irregular shapes since the zero energy for a pixel to be surrounded by other pixels of the same cell would be very similar to the small positive energy for the pixel to be surrounded by pixels of a different cell.

2.1.2 Continuum fields at the extracellular scale

VEGF concentration

The VEGF concentration obeys the following initial-boundary value problem [90]:

$$\begin{aligned}
\frac{\partial C(x,y,t)}{\partial t} &= D_f\left(\frac{\partial^2 C(x,y,t)}{\partial x^2}+\frac{\partial^2 C(x,y,t)}{\partial y^2}\right)\\
&\quad -\nu\, C(x,y,t) - G(x,y,C),\ (x,y)\in\Omega,\ t>0, \qquad (2.1.7)\\
C(0,y,t) &= 0,\ C(L,y,t)=S,\\
C(x,0,t) &= \frac{S}{L}x = C(x,L,t),\ (x,y)\in\partial\Omega,\ t>0, \qquad (2.1.8)\\
C(x,y,0) &= 0,\ (x,y)\in\Omega. \qquad (2.1.9)
\end{aligned}$$

In Eq. (2.1.7), the amount of VEGF bound by an EC per unit time is

$$G(x,y,C)=\begin{cases}\Gamma, & \text{if } \Gamma\le \upsilon\, C(x,y) \text{ and } (x,y)\in\Sigma_{\text{EC}},\\ \upsilon\, C, & \text{if } 0\le \upsilon\, C(x,y)<\Gamma \text{ and } (x,y)\in\Sigma_{\text{EC}},\\ 0, & \text{if } (x,y)\notin\Sigma_{\text{EC}},\end{cases} \qquad (2.1.10)$$

where $\upsilon = 1$ h^{-1} and $\Gamma = 0.02$ pg/(μm^2 h) is the maximum amount of VEGF that it could be consumed by a cell per hour [90, 99]. Other values we use are $D_f = 0.036$ mm^2/h, $\nu = 0.6498$/h [90], and $S = 5\times10^{-19}$g/μm^2 (corresponding to 50 ng/mL [31,120] for a sample having a 10 μm height [92]).

Strains

Following Ref. [92], we calculate the ECM strains by using the finite element method to solve the stationary Navier equations of linear elasticity:

$$\begin{aligned} K\ u = f, &\quad \text{in } \Omega, \\ u = 0, &\quad \text{in } \partial\Omega. \end{aligned} \tag{2.1.11}$$

Here K is the stiffness matrix, u is the array of the x and y displacements of all nodes and f is the array of the traction forces per unit substrate thickness exerted by the cells. For nodes outside ECs, $f = 0$. For nodes inside ECs, each component $f_k = \mu_{\text{force}} \sum_j d_{kj} \delta_{\sigma_k, \sigma'_j}$ represents the traction stress on the kth node, μ_{force}, times the sum of the distances, d_{kj}, between the kth node and any node j in the same cell (σ_k is the label of the cell at which node k belongs).

The global stiffness matrix K is assembled from the stiffness matrices K_e of each pixel,

$$K_e = \int_{\Omega_e} B^T D B \ d\Omega_e, \tag{2.1.12}$$

in which

$$D = \frac{E}{1-\nu^2} \begin{pmatrix} 1 & \nu & 0 \\ \nu & 1 & 0 \\ 0 & 0 & \frac{1}{2}(1-\nu) \end{pmatrix}, \tag{2.1.13}$$

and B is the strain-displacement matrix for a four-noded quadrilateral pixel (finite element) [92]. B is a 3×8 matrix that relates the 8-component node displacement u_e of each pixel to local strains ϵ,

$$\epsilon = B u_e, \tag{2.1.14}$$

where $\epsilon = (\epsilon_{11}, \epsilon_{22}, \epsilon_{12})$ is the 3-component column notation of the strain tensor

$$\epsilon_T = \begin{pmatrix} \epsilon_{11} & \epsilon_{12} \\ \epsilon_{12} & \epsilon_{22} \end{pmatrix}. \tag{2.1.15}$$

We have used the numerical values $E = 10$ kPa, $\nu = 0.45$, and $\mu_{\text{force}} = 1$ N/m^2. With these definitions and the durotaxis term given by Eq. (2.1.5), ECs generate mechanical strains in the substrate, perceive a stiffening of the substate along the strain orientation, and extend preferentially on stiffer substrate. The simulated ECs spread out on stiff matrices, contract on soft matrices, and become elongated on matrices of intermediate stiffness [92].

2.1.3 Signaling processes

The Notch signaling pathway is activated when Notch (transmembrane receptor) belonging to a particular cell interacts with Delta-4 or Jagged-1 (transmembrane ligands) belonging to its neighboring cell (trans-activation), thereby releasing the Notch intracellular domain (NICD). NICD then enters the nucleus and modulates the expression of many target genes of the Notch pathway, including both the ligands Delta and Jagged. However, when Notch of a cell interacts with Delta or Jagged belonging to the same cell, no NICD is produced; rather, both the receptor (Notch) and ligand (Delta or Jagged) are degraded (cis-inhibition) and therefore the signaling is not activated. For a given cell i surrounded by other cells, the equations describing this pathway are [110]

$$
\begin{aligned}
\frac{dN_i}{dt} &= r_N H^S(I_i, \lambda_{I,N}) - \big\{ [k_C D_i + k_T D_{\text{ext}}(i)]\, H^S(I_i, \lambda_{D,F}) \\
&\quad + [k_C J_i + k_T J_{\text{ext}}(i)]\, H^S(I_i, \lambda_{J,F}) + \gamma \big\}\; N_i, && (2.1.16)\\
\frac{dD_i}{dt} &= r_D H^S(I_i, \lambda_{I,D}) H^S(V_i, \lambda_{V,D}) - \big[k_C N_i H^S(I_i, \lambda_{D,F}) + k_T N_{\text{ext}}(i) + \gamma \big]\, D_i, && (2.1.17)\\
\frac{dJ_i}{dt} &= r_J H^S(I_i, \lambda_{I,J}) - \big[k_C N_i H^S(I_i, \lambda_{J,F}) + k_T N_{\text{ext}}(i) + \gamma \big]\, J_i, && (2.1.18)\\
\frac{dI_i}{dt} &= k_T N_i \big[H^S(I_i, \lambda_{D,F}) D_{\text{ext}}(i) + H^S(I_i, \lambda_{J,F}) J_{\text{ext}}(i) \big] - \gamma_S I_i, && (2.1.19)\\
\frac{dV_{Ri}}{dt} &= r_{VR} H^S(I_i, \lambda_{I,V_R}) - k_T V_{Ri} V_{\text{ext}}(i) - \gamma V_{Ri}, && (2.1.20)\\
\frac{dV_i}{dt} &= k_T V_{Ri} V_{\text{ext}}(i) - \gamma_S V_i. && (2.1.21)
\end{aligned}
$$

Here, N_i, D_i, and J_i are the number of Notch, Delta-4, and Jagged-1 proteins in the ith cell, respectively, at time t. I_i, V_{Ri} and V_i are the number of NICD, VEGF receptor and VEGF molecules, respectively, that are in the ith cell at time t. r_N, r_D, r_J, and r_{VR}, are the production rates of N, D, J, and V_R, respectively. The cis-inhibition and trans-activation rates are k_C and k_T, respectively, whereas γ and γ_S are degradation rates for N, D, J, V_R and for I, V, respectively. These parameters, their representative values and units are listed in Table 2.2. All unknowns in Eqs. (2.1.16)-(2.1.21) are initially zero but changing these initial conditions does not alter the outcome of simulations.

Table 2.2: **Rates appearing in Eqs.** (2.1.16)-(2.1.21)**.**

Parameter	r_N	r_D, r_J, r_{VR}	k_C	k_T	γ	γ_S
Value	1200	1000	5×10^{-4}	2.5×10^{-5}	0.1	0.5
Unit	molec/h	molec/h	(h molec)$^{-1}$	(h molec)$^{-1}$	h^{-1}	h^{-1}

Outside the ith cell, the number of X molecules is

$$X_{\text{ext}}(i) = \frac{1}{P_i} \sum_{j \in \langle i \rangle} P_{i,j} X_j, \tag{2.1.22}$$

where $X = N, D, J$, and $j \in \langle i \rangle$ are the cells j sharing boundary of length $P_{i,j}$ with cell i. The perimeter of cell i, P_i, minus $\sum_{j \in \langle i \rangle} P_{i,j}$ is the length of its boundary that is not shared with any other cell. Note that $X_{\text{ext}}(i)$ is simply the sum of all X_j if the lengths $P_{i,j}$ are all equal and $P_i = \sum_{j \in \langle i \rangle} P_{i,j}$ because the whole boundary of cell i is shared with other cells. As the cell moves and its boundaries fluctuate due to cellular Potts dynamics, the membrane protein levels of the neighboring cells interacting with the moving cell also vary. In this way, the production rates of the different proteins in a cell are directly influenced by the interactions with its neighborhood and, in particular, by the membrane fluctuations of the cell. $V_{\text{ext}}(i)$ is the number of VEGF molecules outside the ith cell that interact with VEGF receptor cells to produce VEGF molecules inside the ith cell. The external VEGF cells come from the continuum field $C(x, y, t)$, which diffuses from $x = L$. Let $\mathbf{x}_i$ be the pixel of the ith cell that is closer to the hypoxic region. The number of external VEGF molecules in that pixel is $C(\mathbf{x}_i, t)$ multiplied by the conversion factor $\chi_V = N_A L^2/[(M-1)^2 M_V]$, where M_V is the molecular weight of the VEGF molecules and N_A is the Avogadro number. We have used $\chi_V = 1$, which is representative of VEGF molecules with a large molecular weight. In the numerical simulation, C is known in the grid points and its value at a pixel should be the average value of the four grid points of the pixel. Since these values are quite similar, we adopt the value of C at the bottom left grid point of the pixel $\mathbf{x}_i$ as $C(\mathbf{x}_i, t)$.

The shifted, excitatory and inhibitory Hill functions appearing in Eqs. (2.1.16)-(2.1.21) are:

$$H^S(\xi, \lambda_{\eta,\zeta}) = H^-(\xi) + \lambda_{\eta,\zeta} H^+(\xi), \tag{2.1.23}$$

$$H^-(\xi) = \frac{1}{1 + \left(\frac{\xi}{\xi_0}\right)^{n_\zeta}}, \quad H^+(\xi) = 1 - H^-(\xi), \tag{2.1.24}$$

where H^S is excitatory for $\lambda_{\eta,\zeta} > 1$ and inhibitory for $\lambda_{\eta,\zeta} \le 1$. In Eqs. (2.1.23)-(2.1.24), $\xi = V, I$, $\eta = I, V, D, J$, and $\zeta = N, D, J, V_R, F$ (the subscript F refers to Fringe, cf. [110]). The dimensionless parameters n_ζ and $\lambda_{\eta,\zeta}$ appearing in the Hill functions are listed in Table 2.3.

Table 2.3: **Dimensionless parameters appearing in the Hill functions**. I_0 and V_0 are activation numbers of NICD and VEGF molecules, respectively, and χ_V is the conversion factor.

Par.	$\lambda_{I,N}$, $\lambda_{V,D}$, $\lambda_{I,J}$	$\lambda_{I,D}$, λ_{I,V_R}	$\lambda_{D,F}$	$\lambda_{J,F}$	n_N, n_D, n_V, n_{V_R}	n_J	n_F	I_0, V_0	χ_V
Value	2.0	0.0	3.0	0.3	2.0	5.0	1.0	200	1.0

Table 2.4: **Units for nondimensionalizing the Notch equations** (2.1.16)-(2.1.21).

Var.	N_i, D_i, J_i, N_{ext}, D_{ext}, J_{ext}	I_i	V_{Ri}	V_i	V_{ext}	t
Scale	$\sqrt{r_D/k_C}$	$(k_T r_D)/(k_C \gamma_S)$	r_{V_R}/γ	V_0	$6V_0$	$1/\sqrt{k_C r_D}$
Value	$\sqrt{2} \times 10^3$	10^2	10^4	2×10^2	12×10^2	$\sqrt{2}$
Unit	molec	molec	molec	molec	molec	h

2.1.4 Cell types, proliferation, branching and anastomosis

Cell types

In the model, ECs may be on a tip, hybrid or stalk cell phenotype. In nature, tip cells are characterized by having high levels of Delta-4, VEGFR2, and active VEGF signaling (i.e., high levels of VEGF internalization). They develop filopodia and migrate along the VEGF-A gradient, leading the formation of new branches. Delta-4 proteins at tip cell membranes inhibit the neighboring cells (due to lateral inhibition) to adopt a tip phenotype, thereby forcing them to become stalk cells (with low Delta-4, VEGFR2 and internalized VEGF).

Likewise, in our model, tip cells are distinguished by the number of VEGF molecules they possess. Therefore, a cell that has V larger than all its neighbors and $V > 0.5 \max_i V_i(t)$ will acquire the tip cell phenotype and be very motile. To simulate this, tip cells are able to follow the mechanical and chemical cues on the environment, having $\rho_{\text{chem}} \neq 0$ and $\rho_{\text{durot}} \neq 0$. On the other hand, stalk cells are less motile. We consider two different cases: (A) nonmotile stalk cells with $\rho_{\text{chem}} = \rho_{\text{durot}} = 0$ in the model (except when they undergo proliferation, as explained below) [90]; and (B) motile stalk cells with the same ρ_{durot} as for the tip cells, but a smaller ρ_{chem} than that of the tip cells (see below). Stalk cells, by virtue of the lateral induction, characteristic of Notch-Jagged signaling, are able to induce neighboring cells to adopt a stalk cell phenotype, by promoting a decrease of internal VEGF in them.

In our model we track the cells belonging to each growing vessel. A new sprouting vessel can be formed when a stalk cell acquires the tip phenotype. This cell can then become the leading cell of a new vessel that branches out from out the old one. This is illustrated in Fig. 2.2. If the levels of VEGF inside the tip cells that lead an active growing branch drop to values in the interval $0.2 \max_i V_i(t) < V < 0.5 \max_i V_i(t)$, these cells will be in the hybrid phenotype. In spite of the lower amount of Delta-4, VEGFR2 and VEGF, these cells remain with the tip cell characteristics and are able to lead the sprout. Similarly, stalk cells whose internal VEGF increases to the same range acquire the hybrid phenotype and can lead a sprout. The number of cells in the hybrid phenotype is only appreciable for larger Jagged production rates.

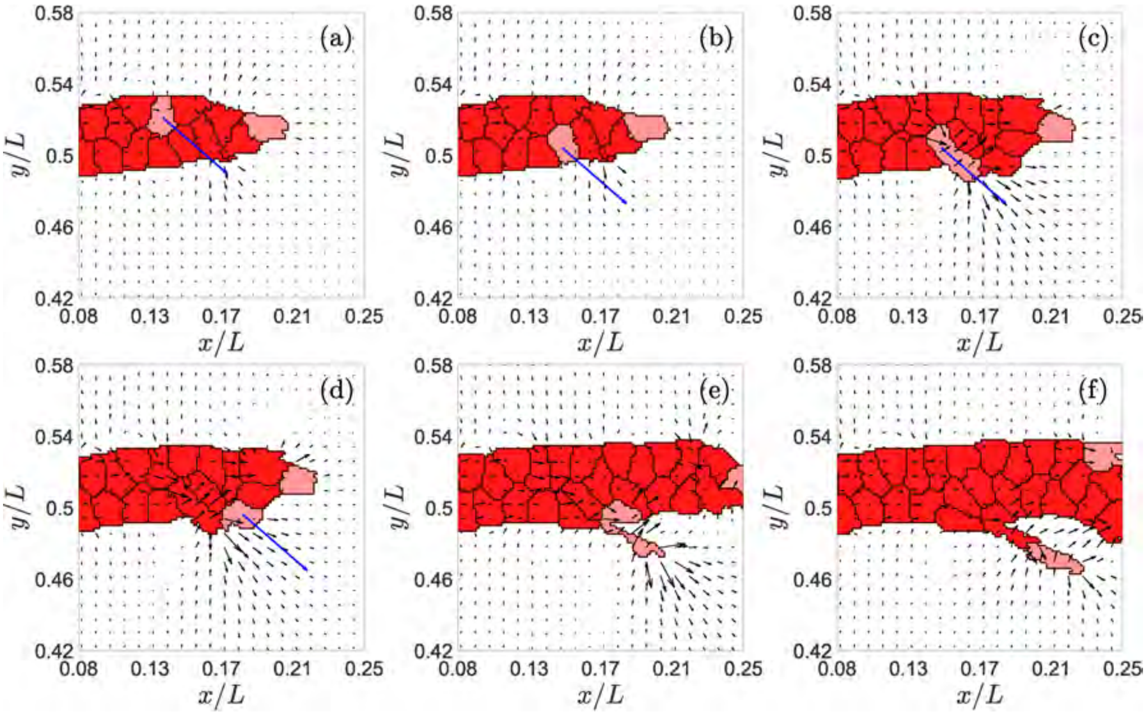

Figure 2.2: **Example of tip cell exchange and branching in the direction of the blue arrow.** Times in MCTS are: (a) 422, (b) 423, (c) 460, (d) 461, (e) 545, (f) 630. The black arrows in this figure represent the directions of largest eigenstrain and, therefore, they point to the likeliest direction of EC motion. The blue arrows indicate the actual direction of motion of a selected tip cell (marked in pink color) for the simulation we have carried out.

Branching

When a stalk cell acquires the tip cell or the hybrid tip/stalk cell phenotype, this event will lead to the creation of a new active sprouting branch depending on its localization within the existing branch and on its moving direction.

To create a new branch, the boundary of the tip cell must touch the ECM. Moreover, let $\mathcal{P}$ be the set of $n_{\mathcal{P}}$ ECM pixels that have boundary with the branching tip cell. For each pixel $\mathbf{x}_p \in \mathcal{P}$, let the *strain vector* be $\mathbf{v}_p = \epsilon_j \mathbf{v}_j$, where ϵ_j is the largest eigenstrain at pixel $\mathbf{x}_p$ and $\mathbf{v}_j$ is the corresponding unit eigenvector, as defined after Eq. (2.1.5). The average modulus and argument for the branching cell i are

$$\Lambda_i = \frac{1}{n_{\mathcal{P}}} \sum_{p\in\mathcal{P}} |\mathbf{v}_p|, \quad \theta_i = \frac{1}{n_{\mathcal{P}}} \sum_{p\in\mathcal{P}} \mathrm{Arg}\, \mathbf{v}_p. \tag{2.1.25}$$

Let us also assume that the gradient of the chemotactic factor C forms an angle Θ with the x-axis. The new tip cell will branch out, creating a new vessel, if the direction given by θ_i points in the direction of the ECM and if $-\pi/2 < \theta_i - \Theta < \pi/2$. For other values of θ_i, the tip cell may not leave the parent vessel, since the chemotactic term of Eq. (2.1.6) opposes branching. Other possibility is that the direction given by θ_i points to another cell, not to the ECM. To facilitate branching computationally, we directly exchange the new tip cell with this neighboring cell (see Figs. 2.2(a) and 2.2(b)). These exchanges may continue in successive MCTS until the new tip cell reaches a boundary of the blood vessel for which the direction given by θ_i points to the ECM, as shown in Fig. 2.2. These cell exchanges in 2D mimic the climbing motion of the new tip cell over the parent vessel in a 3D geometry without merging with it.

We set the branching process to take at least 400 MCTS (incubation time). During this time we implement a persistent motion of the new tip cell in the direction marked by the angle θ_i. During this incubation period, and to provide a good separation from the parent vessel we permit the tip cell to proliferate once (see Figs. 2.2(e) and 2.2(f), and see below). After this time, the dynamics of the branching vessel follows the same rules as that of any other actively sprouting vessel.

Cell proliferation and duration of one MCTS

Endothelial cell proliferation in sprouting angiogenesis is regulated by both mechanical tension and VEGF concentration. In sprouting angiogenesis the tip cell creates tension in the cells that follow its lead. On those first stalk cells, this tension produces strain that triggers cell proliferation, if VEGF concentration is high enough [29]. Therefore, in our model, for each active sprouting vessel, one of the stalk cells that is in contact with a tip cell is randomly chosen to undergo proliferation. Only one cell per sprout proliferates. Tip cells in the model cannot proliferate, except only once when they start a new branch. Once a stalk cell attached to a tip cell has been randomly selected as a proliferating cell, its target area in the CPM is set to become twice the size, whereas its target perimeter is set to a value three times that of non-proliferating cells. This cell will then grow in successive MCTS until it reaches this large target area. Then the cell proliferates if the following three conditions hold: (i) $C(\mathbf{x}_i, t) > \psi_p$ (external VEGF surpasses a threshold), (ii) the cell belongs to an active blood vessel with cell proliferation, and (iii) the cell is not surrounded completely by other cells. Failure to meet one of these conditions precludes proliferation. If the three conditions are met, we use the unsupervised machine learning algorithm *K-means clustering* to split the cell. This algorithm calculates the Euclidean distance of each pixel in the cell to the centroid of two groups of pixels and corrects the centroids until the two pixel groups are balanced. These two groups comprise the new cells. Provided the daughter cells share boundary with the tip cell, one of them is randomly chosen to retain the ability to proliferate but the other cell does not proliferate. If the daughter cells do not share boundary with the tip cell, they both become non-proliferating and a different cell that shares boundary with the tip cell is randomly chosen to become a proliferating cell.

The actual proliferation rate depends on the duration of the cell cycle in MCTS and on how many seconds one MCTS lasts. The latter time is fitted so that numerical simulations reproduce the experimentally observed velocity of a sprouting vessel. We consider two cases. In case (A), we drop the elongation constraint $\rho_{\text{length}} = 0$ and make the stalk cells insensitive to chemo and durotaxis, therefore $\rho_{\text{chem}} = \rho_{\text{durot}} = 0$ for them. Only tip cells move in this case. In case (B), stalk cells also move, albeit more slowly than tip cells. While $\rho_{\text{durot}} = 25$ for both types of EC, $\rho_{\text{chem}}(\mathbf{x}, \mathbf{x}')$ is given by

$$\rho_{\text{chem}}(\mathbf{x}, \mathbf{x}') = \frac{\rho^0_{\text{chem}}}{\max_k D_k} \begin{cases} D_i, & \mathbf{x} \in \Sigma_i,\ \mathbf{x}' \in \Sigma_{\text{ECM}} \text{ or vice versa}, \\ \frac{D_i + D_j}{2}, & \mathbf{x} \in \Sigma_i,\ \mathbf{x}' \in \Sigma_j \text{ or vice versa}, \end{cases} \tag{2.1.26}$$

where i and j are ECs. The level of Delta-4 determines the EC phenotype and, according to Eqs. (2.1.6) and (2.1.26), the strength of their chemotactic drive. Tip cells have a higher level of Delta-4 and, consequently, they are more motile than stalk cells. As the latter also move, it may occur, as shown in Fig. 2.3, that a stalk cell overtakes a tip cell to become the leading cell of its sprout. This has been observed in experiments [30, 31] and in numerical simulations of CPMs different from ours [121]. In our model, the imposed strong gradient of the VEGF concentration $C(\mathbf{x}, t)$ precludes ECs to reverse their direction, unlike the CPMs in Ref. [121], which set a constant external VEGF concentration for their simpler Notch-Delta signaling dynamics. In Ref. [121], chemotaxis is guided by the gradients of a chemical signal secreted by the ECs (seemingly different from VEGF). The chemical signal also diffuses and is consumed by the ECM. Local chemical signal gradients may become contrary to the motion of a given EC, thereby facilitating reversal of its motion. In our model on the other hand, numerical simulations show that a growing sprout may separate from the primary blood vessel more than one cell diameter (10 μm). As the primary vessel is a source of ECs, we create a new stalk cell to fill the resulting hole if this happens.

To obtain the equivalence between the number of MCTS and the time measured in experiments, we measured the pixel size in Fig. 1H of Ref [120], which is 0.9 μm. According to Fig. 3C of the same reference, the vessel mean elongation is 150 pixels (135 μm) in

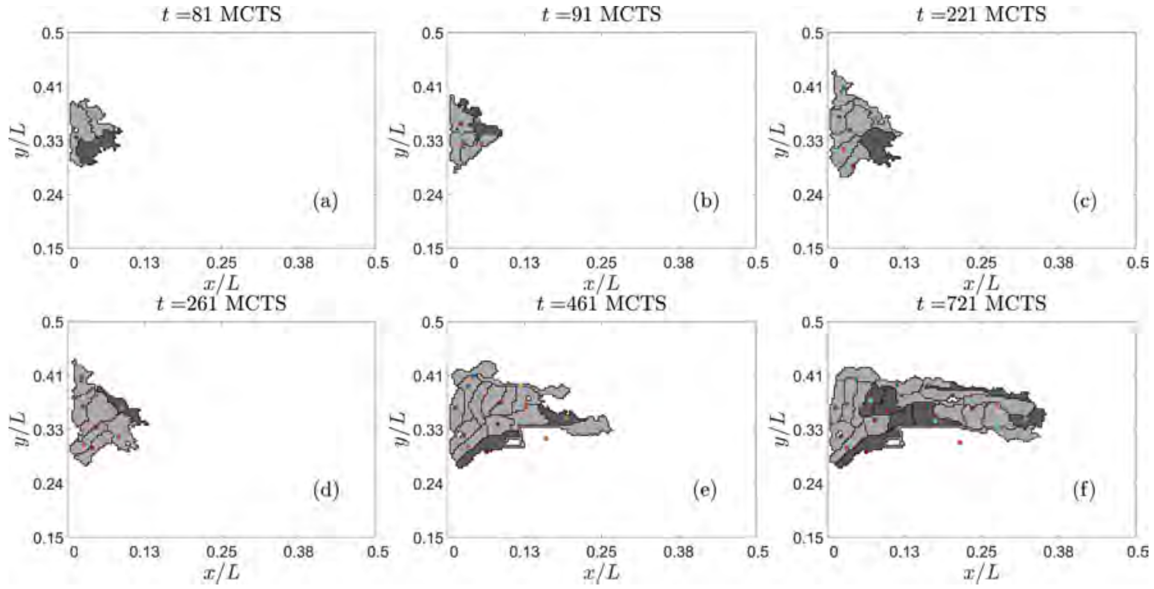

Figure 2.3: **Examples of stalk cells (light color) overtaking tip cells (dark color) in numerical simulations with case (B) dynamics.** EC centers are marked by dots. Note that ECs are more elongated than those undergoing case (A) dynamics.

36 hours for 50 ng/mL VEGF concentration. In our simulations of case (A) dynamics, the vessel mean elongation is 495 μm in 3001 MCTS. Thus, we set 1 MCTS to be 0.044 hours. A similar calculation for case (B) dynamics yields 1 MCTS = 0.03 hours (vessel mean elongation of 247.5 μm in 2200 MCTS).

We can estimate roughly EC proliferation time by dividing the MCTS one sprout is active by the number of cells created in the sprout during that time. We discard those sprouts whose ECs have never proliferated and average over all numerical simulations with the same dynamics, i.e., cases (A) and (B). The resulting proliferation times are 120 MCTS (5.28 hours) for case (A), and 217 MCTS (6.51 hours) for case (B). The proliferation times thus obtained are lower bounds: although only one EC of a given sprout is selected to proliferate at a given time, we cannot guarantee that the same EC of the same sprout will proliferate again at a later time. It could be a different cell that proliferates next, which would surely occurs when performing different numerical simulations. Then the average time for one EC to complete its cell cycle should be longer than that given by our estimation. With this proviso, our proliferation times are shorter but of the same order of magnitude as previously reported division times for EC in vivo or in vitro (83 minutes for cell mitosis but 17.8 hours to complete the cell cycle [122]). Fine tuning of parameters and better estimations of the cell cycle from numerical simulations might produce better agreement with reported experimental values, which, anyway, present some variability.

Anastomosis

When an active sprouting blood vessel merges with another active sprouting vessel, i.e. during anastomosis, one of them becomes inactive. If the collision occurs between tip cells of two different vessels, one vessel is randomly chosen to become inactive. If one tip cell merges with a stalk cell of a different active sprouting vessel, the vessel to which the tip cell belongs becomes inactive. The cells of an inactive vessel do not proliferate or branch, although they continue to undergo Notch signaling dynamics.

2.2 Results

We have run our simulation models for a simple slab geometry and different conditions. A primary vessel is supposed to be along the y axis. The initial VEGF concentration $C(\mathbf{x}, 0)$ is independent of y and decays linearly in x from $x = L$ to $x = 0$. Thus, chemotaxis pushes tip cells towards the vertical line at $x = L$. Most of the results we present below are illustrated with simulations of case (A) dynamics. Except for obtaining more elongated cells and allowing for stalk cell overtaking tip cells, case (B) dynamics produces qualitatively analogous results, as we comment where appropriate. A detailed description of the simulation code can be found in chapter 5.

Cellular mechanics and anastomosis

It is clear that without the deformation of ECM induced by cells tractions and the strain vectors, there will be no branching direction for new tip cells to exit from a given sprout. Thus, cellular mechanics is crucial for branching. We have also found that cellular mechanics significantly controls anastomosis. The arrows in Fig. 2.4 are directed along the strain vector (eigenvector corresponding to the largest eigenstrain and having length equal to that eigenstrain). According to Eq. (2.1.5), the arrows indicate the likeliest direction in which ECs will move. The snapshots depicted in Fig. 2.4 show examples of successful and frustrated anastomosis and branching of advancing blood vessels. A tip cell leads successful branching from the blood vessel at the bottom of Fig. 2.4(a), as shown by Panels (b) and (c). Meanwhile, two blood vessels that sprout from the blood vessel at the top of Fig. 2.4(a) successfully anastomose as shown in Fig. 2.4(c). Notice that the strain vectors show the path of the approaching vessels until they anastomose. However, the branches arising from the two lowest vessels in Fig. 2.4(a) do not anastomose. They approach each other in Fig. 2.4(c) but the strain vectors pull them away from each other and anastomosis is frustrated, as shown in Figs. 2.4(d) and 2.4(e) [92,123,124].

Tip cells have higher levels of VEGF and their motion follows stiffness, chemical and adhesion gradients, as expected from the model. In successful anastomosis, one tip cell is directed by the strain vector to one actively sprouting vessel. When it makes contact, it fuses with that vessel. After that, the VEGF in the tip cell decreases and it becomes a stalk cell.

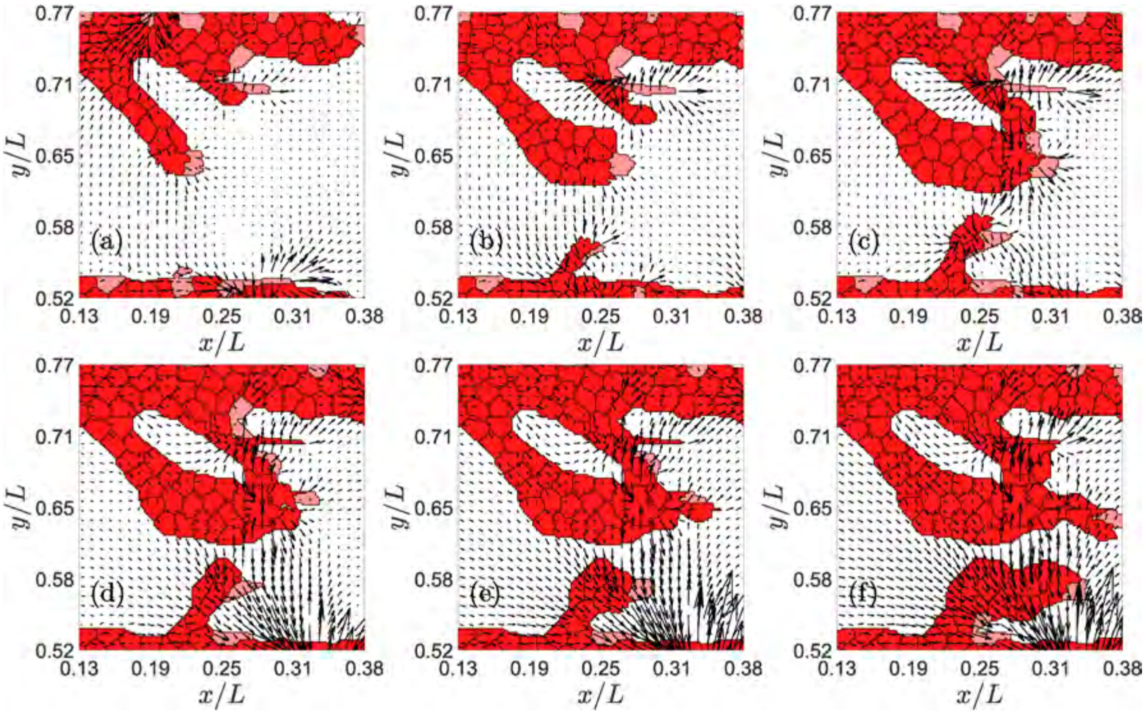

Figure 2.4: **Example of successful and frustrated anastomosis.** Times in MCTS are: (a) 751, (b) 851, (c) 951, (d) 1051, (e) 1101, (f) 1201. Tip cells are pink.

Jagged–Delta dynamics and sprouting

Jagged and Delta dynamics determine sprouting [110, 111]. Studies of Notch signaling in one cell driven by external Jagged and Delta molecules show that the phenotype of a tip cell changes to hybrid tip/stalk and then to stalk cell as the external Delta concentration surpasses successive thresholds (cf. Fig. 3 of Ref. [110]). The thresholds depend on the Jagged production rate. Lateral induction works similarly for one cell driven by external Jagged molecules: tip cells change to hybrid tip/stalk and stalk phenotypes as the external Jagged concentration surpasses successive Delta-dependent thresholds [110, 111]. Simulations of our model illustrate the effects of J-N and D-N signaling combined with chemo-, hapto- and durotaxis. Figure 2.5 shows that increasing the Jagged production rate r_J yields smaller branching blood vessels, thereby decreasing the irrigation of the hypoxic region. Furthermore, sprouting is accelerated as the Jagged production augments: thinner and less efficient sprouts are formed faster as r_J increases. Stalk cells proliferate on advancing sprouts. Thus, increasing the number of tip cells leading sprouts results in increasing cell proliferation and a more rapid sprout advance. This behavior agrees with the sketch in Fig. 5A of Ref. [110], which indicates that pathological angiogenesis is obtained when there is an excess Jagged production. The sprouts in physiological angiogenesis are thicker and advance more slowly than the more abundant and thinner sprouts in pathological angiogenesis, as shown in Fig. 2.5.

The Delta production rate r_D acts opposite to r_J. High and intermediate levels of r_D ensure physiological angiogenesis, whereas the numbers of the hybrid tip/stalk cells increase for low levels of r_D. In more detail, we observe that, for $r_J = 500$ molec/h and $r_D = 1000$ molec/h, Figs. 2.6(a) and 2.6(b) show a gap between the VEGF of stalk and tip cells: the content of V is very low for stalk cells. It increases monotonically with V_{ext} and J for hybrid-tip and tip cells. Fig. 2.6(b) also shows that tip cells and hybrid tip-stalk cells have larger J than stalk cells. As r_J increases, at $r_J = 2000$ molec/h, the hybrid-tip cells have proliferated and bridge the gap in V, as depicted in Figs. 2.6(c) and 2.6(d). Fig. 2.6(d) indicates that J is smaller for the tip cells at large Jagged production rates, which is consistent with lateral induction of stalk phenotype by stalk cells with large J values [110]. For large r_J, tip cells have less Jagged ($J \approx 10$ and $V > 2$) than other cell types (J between 10 and 15 and $V < 2$), as shown in Fig. 2.6(d). Fig. 2.6(e) and 2.6(f) show that the Delta production rate r_D acts in opposition to r_J. At $r_D = 7500$ molec/h, Fig. 2.6(e), there is again a gap between the VEGF of stalk and tip cells. At this large Jagged production rate, tip cells have lower Jagged than stalk cells, as depicted in Fig. 2.6(f), which is similar to Fig. 2.6(d). However, Fig. 2.6(f) exhibits a gap between the maximum value of J for tip cells and the values of J for stalk cells, as compared to Fig. 2.6(d).

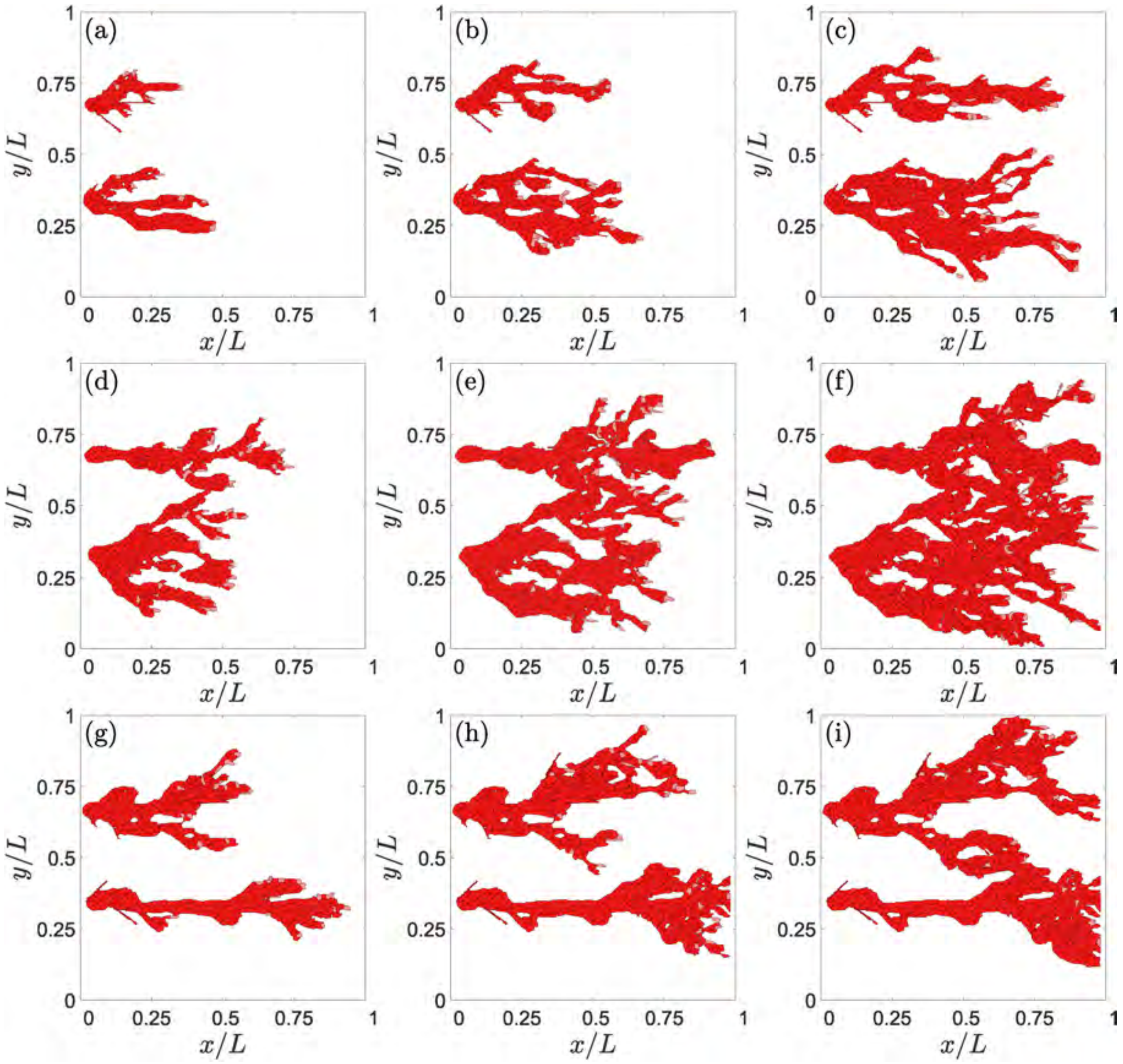

Figure 2.5: **Effect of Jagged production on angiogenesis.** For $r_J = 500$ molec/h and $r_D = 1000$ molec/h, snapshots at times: (a) 2001 MCTS, (b) 2751 MCTS, (c) 3501 MCTS. For $r_J = 2000$ molec/h and $r_D = 1000$ molec/h, snapshots at times: (d) 2001 MCTS, (e) 2751 MCTS, (f) 3501 MCTS. For $r_J = 2000$ molec/h and $r_D = 7500$ molec/h, snapshots at times: (g) 2001 MCTS, (h) 2501 MCTS, (i) 3501 MCTS.

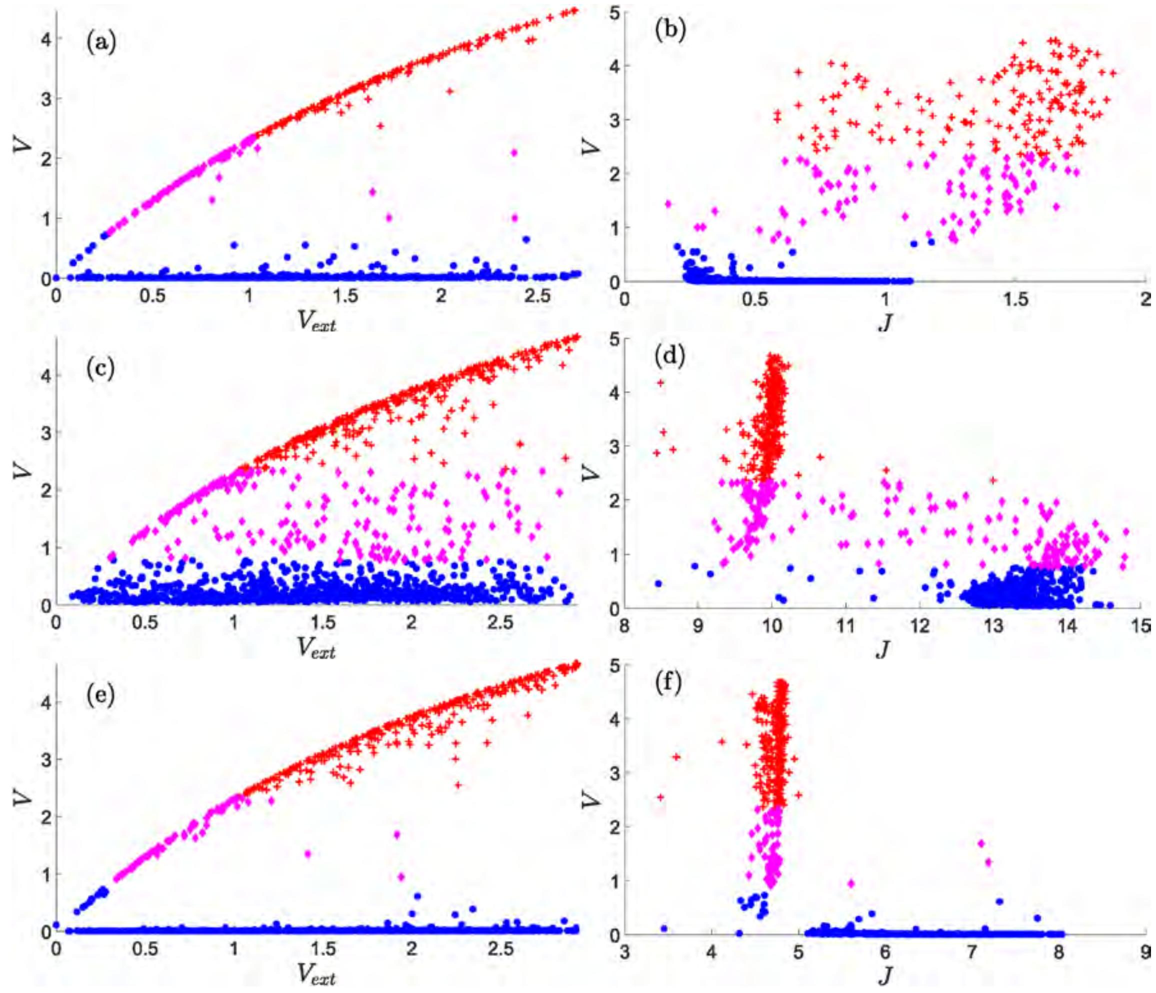

Figure 2.6: **Content of VEGF, V, versus $\mathbf{V_{ext} = C}$, and of V versus J in the tip, stalk and hybrid tip-stalk cells within the angiogenic network at 3501 MCTS.** (a), (b) $r_J = 500$ molec/h, $r_D = 1000$ molec/h; (c), (d) $r_J = 2000$ molec/h, $r_D = 1000$ molec/h; (e), (f): $r_J = 2000$ molec/h, $r_D = 7500$ molec/h. Other parameter values are as indicated in Tables 2.1-2.3. Nondimensional units for V, V_{ext}, J are as indicated in Table 2.4. The meaning of symbols is as follows. Red cross (tip cell), magenta rhombus (hybrid tip/stalk cell), blue circle (stalk cell).

Jagged–Delta dynamics and anastomosis

What is the effect of modifying J-N and D-N signaling on angiogenesis? Figs. 2.5 and 2.7 show the effects of lateral inhibition by D-N signaling versus lateral induction by J-N signaling. Increasing the Jagged production rate produces more hybrid tip/stalk cells and more sprouts, as shown by Figs. 2.5 and, for the higher content of hybrid tip/stalk cells, by Figs. 2.6(c) and 2.6(d). However, for a high Jagged production rate, increasing the Delta production rate favors lateral inhibition by tip cells, which eventually decreases the number of new sprouts, makes anastomosis less frequent, as illustrated by Figs. 2.5(g), 2.5(h), 2.5(i), and 2.7.

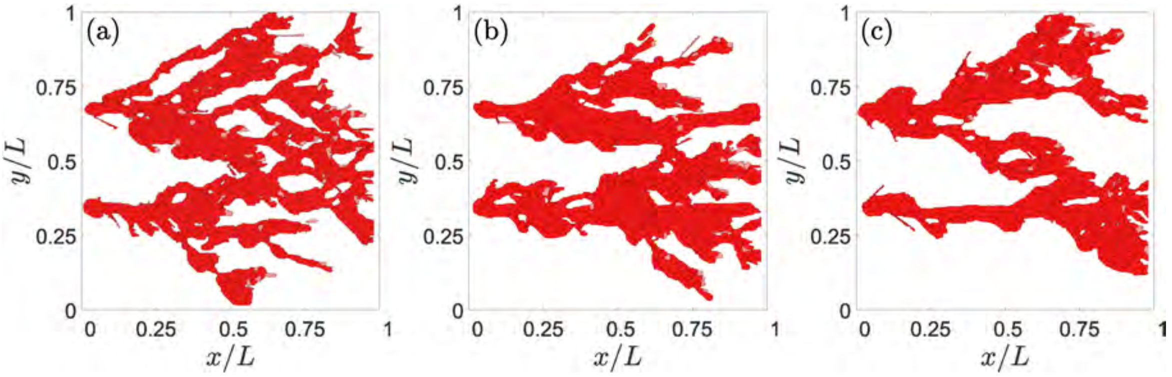

Figure 2.7: **Effect of the Delta production rate on angiogenesis with a high Jagged production rate of $\mathbf{r_J = 2000}$ molec/h at 3501 MCTS.** (a) $r_D = 3000$ molec/h, (b) $r_D = 6000$ molec/h, and (c) $r_D = 7500$ molec/h. Lateral inhibition due to more activated D-N signaling decreases the number of hybrid tip/stalk cells and branching.

Fig. 2.8 shows the concentrations of N, V, J and D for a developed angiogenic network for several values of the Jagged-1 and Delta-4 production rates. We observe that tip cells have large values of V and D for both normal ($r_J = 500$ molec/h) and high ($r_J = 2000$ molec/h) Jagged production rates, cf. Figs. 2.8(g)-(i) and 2.8(m)-(o). These figures highlight the role of lateral inhibition on stalk cells that are neighbors of tip cells.

For large r_J, Figs. 2.8(k) and 2.8(l) show that stalk cells clearly have larger values of J, thereby illustrating the more important role of lateral induction. For large r_J and moderate r_D, Fig. 2.8(h) exhibits a larger number of cells with intermediate values of their internal VEGF, which shows the abundance of the hybrid tip/stalk cell phenotype. This is not the case for lower Jagged production rate as shown by the VEGF content in Figs. 2.8(g) and, for higher Delta production rate, in Fig. 2.8(i). As explained before and as shown by comparing Figs. 2.6(b) to 2.6(d) and 2.6(f), stalk cells have a smaller value of J than tip or hybrid tip/stalk cells at smaller Jagged production rates. In these cases, lateral inhibition by D-N signaling is more important. Figs. 2.8(m), 2.8(n) and 2.8(o) show that the D level of stalk cells is much reduced as compared with that of neighboring tip cells. Increasing the production rate of Delta-4 restores the morphology of the advancing normal vasculature to angiogenesis with high Jagged production rate, as shown by a comparison of Fig. 2.8(n) to Figs. 2.8(o) and 2.8(m).

Figure 2.9 further shows the effect of varying the production rates of Jagged and Delta on the advance and morphology of the vascular plexus. With respect to the simulations in Figs. 2.2 and 2.4 for standard values of r_J and r_D, increasing the production of Jagged, as shown in Fig. 2.5, produces more tip cells that run faster, cf. Figs. 2.9(a) and 2.9(b). Thus, lateral induction mediated by Jagged accelerates the advance of vasculature and increases the number of blood vessels by creating more hybrid tip/stalk cells, as explained before in relation to Figs. 2.5 and 2.6. If we keep constant r_J and increase the Delta production rate, lateral inhibition by tip cells becomes stronger, cf. Fig. 2.5. Then the number of tip cells decreases whereas the vasculature advances only slightly faster because angiogenesis and anastomosis diminish compared with the case of smaller r_D, cf. Fig. 2.9(c) and 2.9(d).

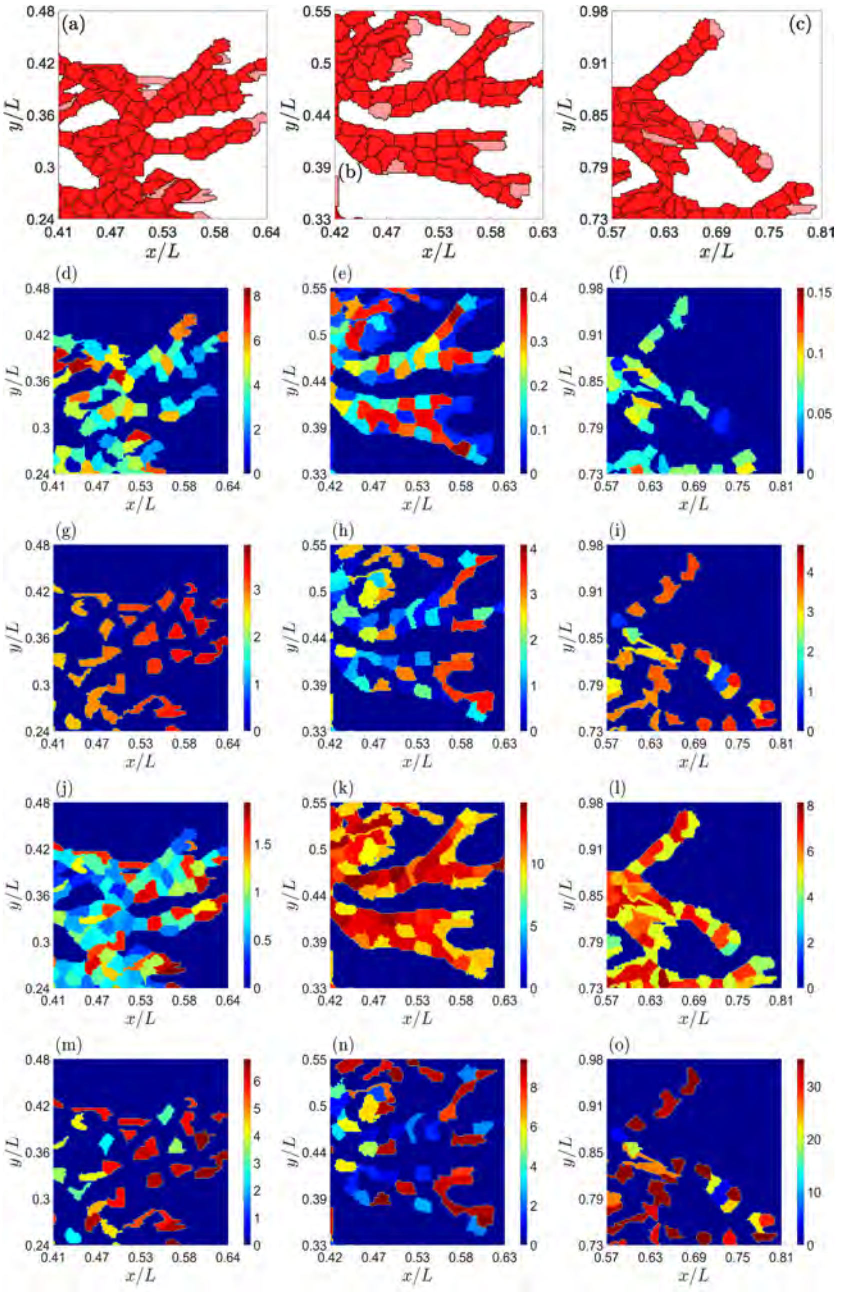

Figure 2.8: **Effect of the Jagged and Delta production rates on angiogenesis at a time of 2901 MCTS.** (a)-(c) Snapshots of networks, (d)-(f) Notch concentration, (g)-(i) VEGF concentration, (j)-(l) Jagged-1 concentration, (m)-(o) Delta-4 concentration. Data: (a),(d),(g),(j),(m) $r_J = 500$ molec/h, $r_D = 1000$ molec/h, (b),(e),(h),(k),(n): $r_J = 2000$ molec/h, $r_D = 1000$ molec/h, (c),(f),(i),(l),(o): $r_J = 2000$ molec/h, $r_D = 7500$ molec/h. Nondimensional units for protein concentrations are as in Table 2.4.

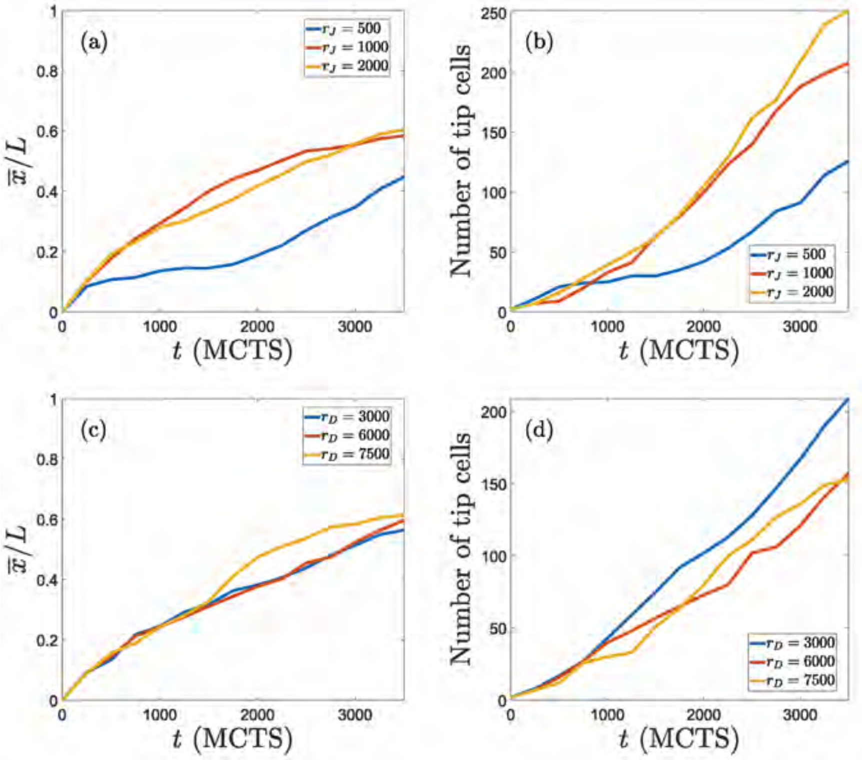

Figure 2.9: **Effect of varying the production rates of Jagged and Delta on the advance and morphology of the vascular plexus** (a) Average abscissa (position on x axis) of the tip cells as a function of time, and (b) number of tip cells versus time for $r_D = 1000$ molec/h and $r_J = 500$, 1000 and 2000 molec/h. Increasing Jagged production rate yields more tip cells that advance faster. (c) Average position of tip cells versus time, and (d) number of tip cells versus time, for $r_J = 2000$ molec/h and $r_D = 3000$, 6000 and 7500 molec/h. Increasing Delta production rate makes tip cells to advance slightly more but it diminishes the number of tip cells. The effect of r_D on the number of tip cells is opposite to that of r_J in Panels (a) and (b).

Sensitivity

The sensitivity of the results to the particular parameter set chosen is studied by varying one parameter at a time. In previous paragraphs, we have analyzed the effect of varying Potts parameters on the simulations of the model. They affect the relative importance of mechanical and chemical cues as described, and their effects are consistent with previous works on chemotaxis [90] and durotaxis [92]. Here we discuss the sensitivity of simulation results to changes in the parameters controlling cellular signaling. To this end, we have carried out 6 simulations for each of the production rates mentioned above and taken the averages of these realizations. Figs. 2.10(a) and 2.10(b) display, as a function of time, the number of angiogenic sprouts and the percentage of pixels of the hypoxic region at $x = L$ that are occupied by them, respectively. The number of sprouts and the occupation fraction ϕ should be contrasted with Figs. 2.5 to 2.7. For fixed $r_D = 1000$ molec/h, increasing r_J produces thinner and more numerous pathological sprouts that arrive faster to $x = L$. Increasing r_D at a higher r_J decreases the proliferation of sprouts and the fraction of pixels occupied by them at the hypoxic region. However, the sprouts move faster towards the hypoxic region, which keeps having a higher occupation fraction ϕ than in the case of physiological angiogenesis with lower r_J. Increasing Delta production decreases the number of sprouts (and thickens them), as corroborated by the experiments of Ubezio *et al* [39]. Fig. 2.11 depicts how the percentages of tip and stalk cells in moving sprouts evolve in time for the data of Fig. 2.10. In all cases, the percentages stabilize to the same low values of tip cells and high values of stalk cells after 2000 MCTS (time it takes the first sprouts to arrive at the hypoxic region). For shorter times, the influence of production rates on the relative number of tip/stalk cells is evident: higher r_J lowers the percentage of tip cells, whereas the influence of an increment of r_D on the percentage of tip/stalk cells is less clear. These data need to be contrasted with those of Figs. 2.5 to 2.7 to achieve a clearer picture of the morphology and thickness of the angiogenic network.

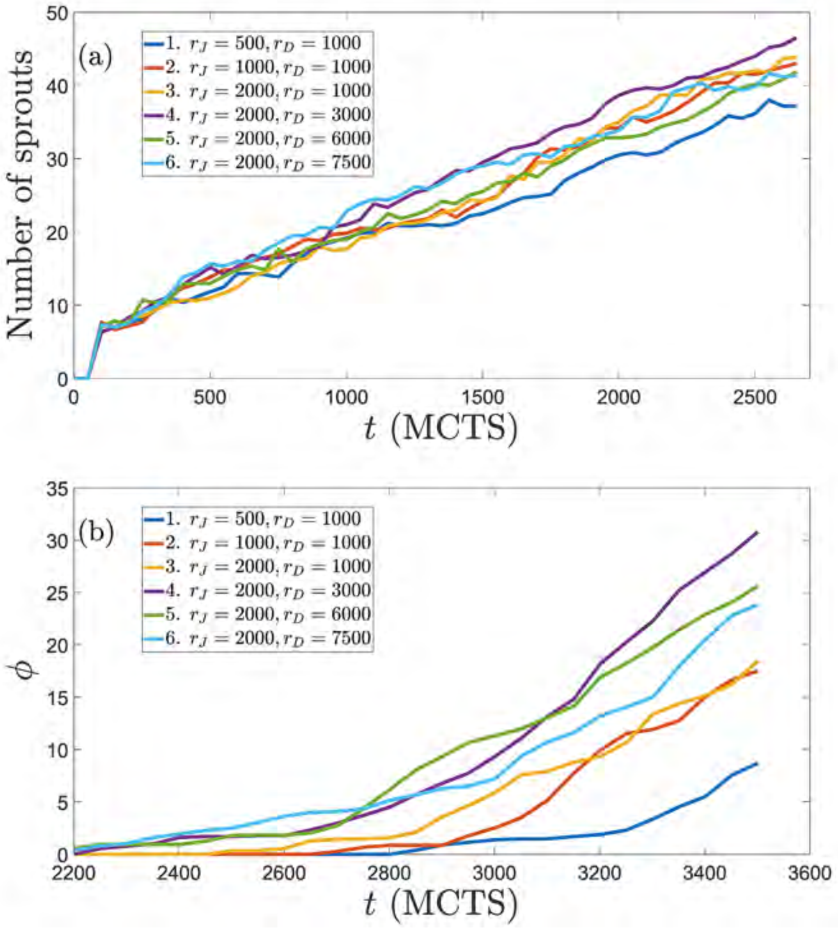

Figure 2.10: **Sensitivity of simulation results to changes in the parameters controlling cellular signaling** (a) Number of angiogenic sprouts versus time, and (b) percentage of pixels ϕ at $x = L$ (the hypoxic region) that are occupied by vessel sprouts versus time, for the indicated Jagged and Delta production rates. Data correspond to averages over 6 realizations of the stochastic process.

Results using case (B) dynamics with cell elongation

Numerical simulations with case (B) dynamics that includes cell elongation produce qualitatively the same results as reported in previous paragraphs. Obvious differences are that ECs are more elongated than in case (A) dynamics and that there is cell overtak-

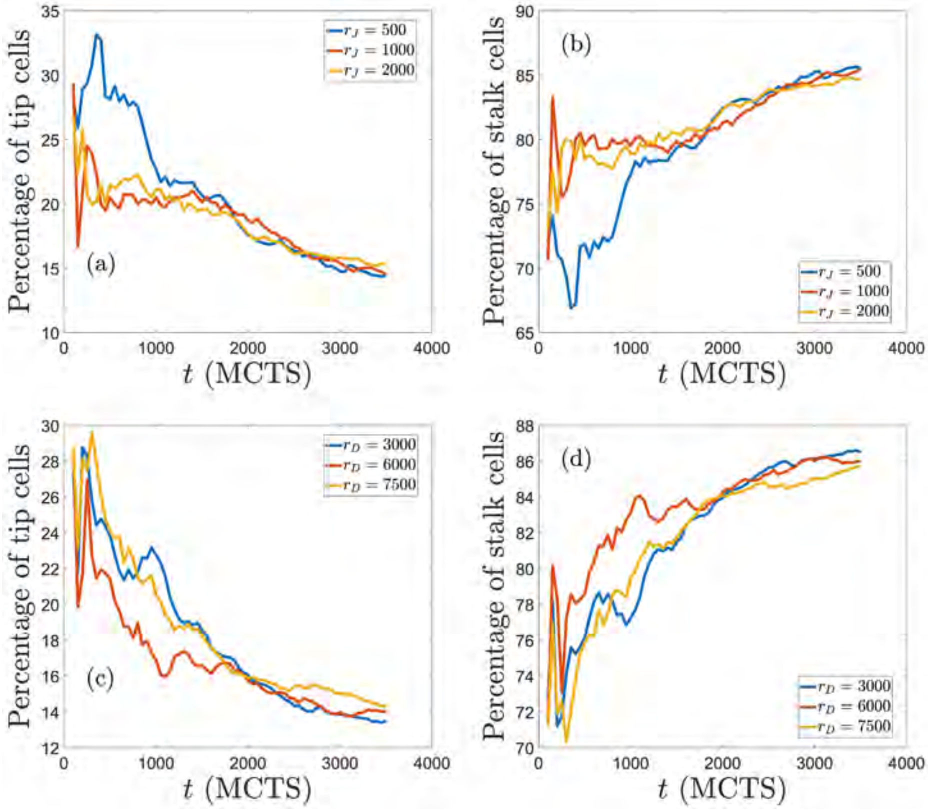

Figure 2.11: **Percentage of tip and stalk cells versus time for the simulations displayed in Fig. 2.10.** Production rates are $r_D = 1000$ molec/h in panels (a) and (b), and $r_J = 2000$ molec/h in panels (c) and (d).

ing as shown in Fig. 2.3. Fig. 2.12 exhibits the elongated cells of case (B) dynamics when compared with the corresponding results of case (A) dynamics depicted in Fig. 2.5. Increasing the Jagged production rate gives rise to more vessel sprouts, and increasing the Delta-4 production rate decreases the number of tip cells and, consequently, decreases the number of sprouts; see Fig. 2.13.

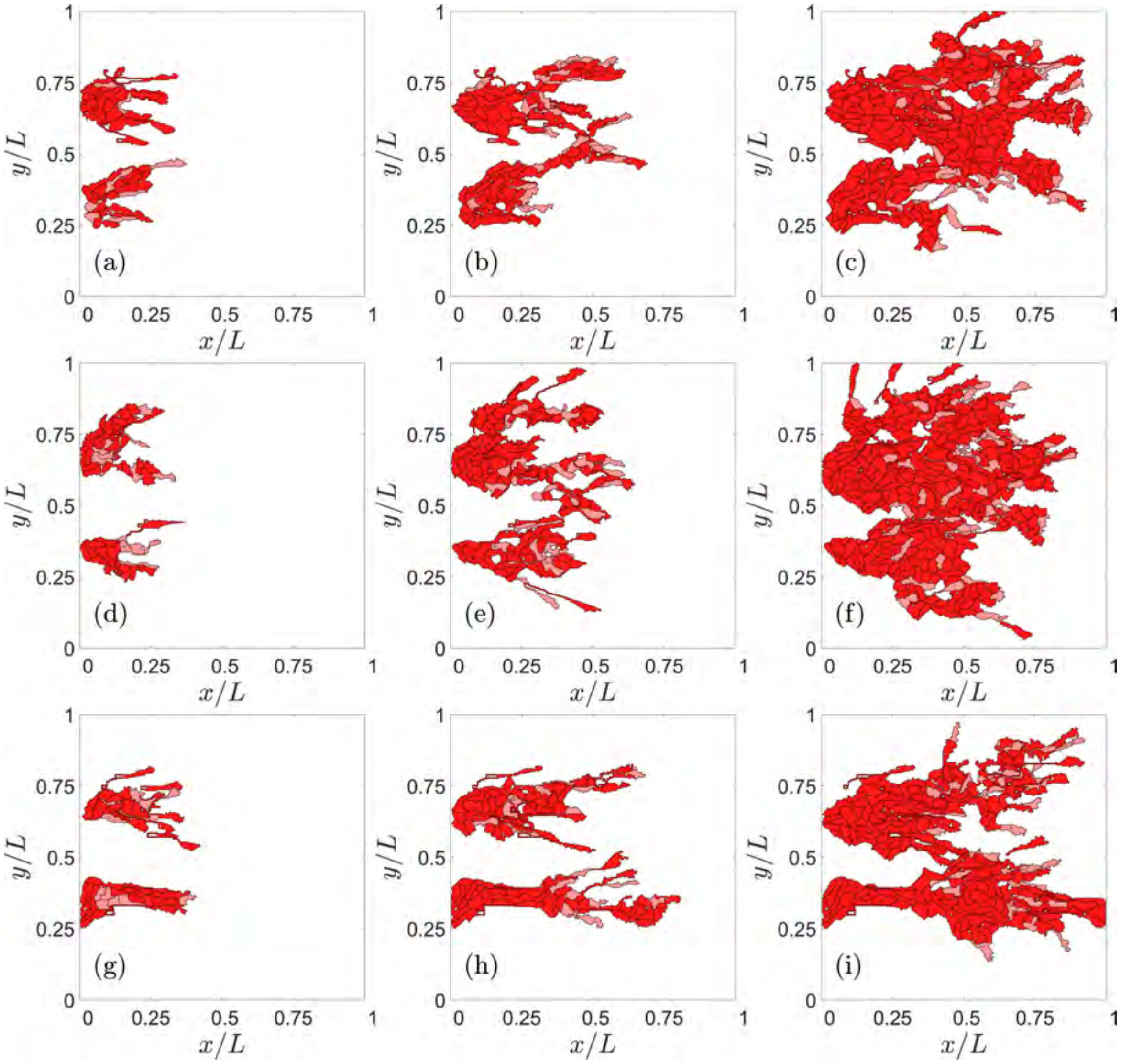

Figure 2.12: **Effect of Jagged production on angiogenesis for case (B) elongational cellular dynamics and a sample of half length than for case (A) dynamics.** For $r_J = 500$ molec/h and $r_D = 1000$ molec/h, snapshots at times: (a) 801 MCTS, (b) 1601 MCTS, (c) 2401 MCTS. For $r_J = 2000$ molec/h and $r_D = 1000$ molec/h, snapshots at times: (d) 801 MCTS, (e) 1601 MCTS, (f) 2401 MCTS. For $r_J = 2000$ molec/h and $r_D = 7500$ molec/h, snapshots at times: (g) 801 MCTS, (h) 1601 MCTS, (i) 2401 MCTS.

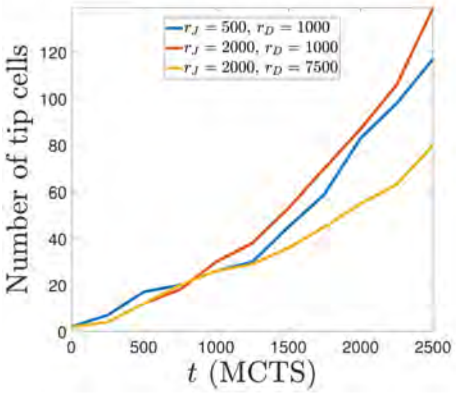

Figure 2.13: **Number of tip cells versus time for $\mathbf{r_J = 500}$ and 2000 molec/h, $\mathbf{r_D = 1000}$ and 7500 molec/h with the elongational cell dynamics of case (B).**

2.3 Discussion

The mathematical model of angiogenesis presented here illustrates the relative importance of mechanical, chemical and cellular cues when they are all considered simultaneously. Given a proliferation rate of cells and a VEGF gradient on a homogeneous extracellular matrix, competing J-N and D-N dynamics determine the influence of lateral inhibition and lateral induction on tip cell selection, branching, anastomosis and speed of angiogenesis. Anastomosis is driven by chemotaxis. Cellular motion is informed by haptotaxis and durotaxis. However, anastomosis may be favored or impeded depending on the mechanical configuration of strain vectors in the ECM near tip cells. Notch signaling determines tip cell selection and vessel branching. We consider two types of cell dynamics. In case (A) dynamics, stalk cells are insensitive to chemical and mechanical cues and may be selected for proliferation when they are next to the tip cell of a growing sprout. Cellular division is informed by the local stress field. Tip cells can only proliferate once, when they start a new sprout, and move by sensing gradients of VEGF and stiffness. This dynamics tends to produce rounder stalk cells. In case (B) dynamics, cellular elongation is constrained and stalk cells move by also sensing chemical and mechanical cues but cellular chemotaxis is proportional to the ratio of the local Delta-4 concentration to the maximum possible value thereof. Thus, tip cells react more strongly to VEGF and are more motile than stalk cells. Yet, the latter also move and may overtake tip cells and replace them as the leading cell of a growing sprout.

For both case (A) and case (B) dynamics, lateral induction by stalk cells and lateral inhibition by tip cells are informed by competing Jagged-Notch and Delta-Notch dynamics in manners that depend quantitatively on the Delta and Jagged production rates. In particular, the numerical simulations of our model predict the following effects of the production rates. Increasing the production rate of Jagged favors lateral induction of stalk cells, which yields more hybrid tip/stalk cells and a thinner vasculature that advances faster. On the other hand and as observed in experiments [39], increasing the production rate of Delta lowers the number of tip cells by lateral inhibition of stalk cells. Then there are less sprouts and anastomosis is less frequent while the advance of the vascular plexus is only slightly faster. Our numerical simulations illustrate the regulating role of Notch-Jagged-Delta signaling in the velocity and morphology of angiogenic vasculature. An imbalance of the Jagged production, so that there is more Jagged and increased lateral induction of stalk cells, results in anomalous thinner sprouts and faster angiogenesis. This may be corrected by increasing the Delta-4 production rate, which boosts lateral inhibition of tip on stalk cells, diminishes the number of tips and slows down somewhat angiogenesis.

To allow for quantitative comparisons with experiments, e.g., [39], our 2D model of early stage angiogenesis needs to be extended in several directions to be made more realistic and to account for later stages of angiogenesis. The extension of the model to three dimensional configurations is straightforward although it requires more computing power. While we have studied relatively short distances between the primary vessel and the target hypoxic region, we need to consider larger systems to be able to do statistical studies of vessel numbers and their width. To move toward later stages of the formation of an advancing vascular plexus, we need to add lumen formation [17] and blood circulation to the model [24]. These processes will allow us to tackle the concurrent sprouting and anastomosis on the front of the advancing vascular plexus and the pruning of poorly perfused sprouts on its back [24, 25].

Chapter 3

Anomalous angiogenesis in retina

In this chapter we present a 2D Potts model that includes EC Notch signaling, chemotaxis, haptotaxis and durotaxis [125] to ascertain the influence of these mechanisms on AMD. We consider the simple geometry sketched in Fig. 1.3 of section 1.1: a square domain in which the Bruch membrane separates the choroid crisscrossed by blood vessels, which may issue angiogenic sprouts, from RPE cells, eventual drusen and a subretinal space on top of which there are photoreceptors. The choroid vessels may issue sprouts at randomly chosen points provided the VEGF concentration surpasses some threshold in those points. The growth of drusen above RPE cells turns on VEGF sources that attract the sprouts issued from the choroid vessels to them. Once ECs have crossed the BM, they either form subRPE type 1 CNV or subretinal type 2 CNV. Type 1 CNV occurs if the sprouts form a network between the BM and the RPE cells, whereas type 2 CNV occurs if the sprouts succeed moving beyond the RPE layer and towards the VEGF emitting photoreceptors. We find that adhesion between RPE cells and between RPE cells and the BM decides whether angiogenic sprouts succeed in invading the subRPE space or the subretinal space, thereby producing type 1 or 2 CNV, respectively.

We study how drusen, defects in the BM and local VEGF gradients affect CNV. Notch signaling dynamics confirms that CNV is an example of pathological angiogenesis with thin and leaky capillary sprouts [125].

The section Angiogenesis Model, 3.1, describes the CPM coupled with the Delta-Notch-Jagged dynamics adapted to the retina. In the section Numerical Results, 3.2, we present the results of the simulation and how impaired adhesion, VEGF concentration and Notch signaling pathway affect CNV. Finally, in the section Discussion, 3.3, we draw the conclusions of the chapter.

3.1 Angiogenesis model

To describe angiogenesis in the retina, we need a model able to describe cellular processes at cellular and subcellular sizes. The CPM [88] is particularly useful at these scales, as it incorporates in a natural way constraints for the volume, area or length of the cells, as well as adhesion between cells or with the extracellular matrix (haptotaxis) [88, 117]. Attraction due to chemical gradients (chemotaxis) [90] or to substrate stiffness gradients (durotaxis) [92] have also been added to CPM. Strains in the cells together with the unsupervised K-means algorithm can be used to implement proliferation of the cells [125]. The phenotype of leading tip cells or follower stalk cells is decided by the Notch signaling pathway, and the corresponding dynamics [110] can also be incorporated to the CPM [125]. The model described in this section is an adaptation of the one presented in the chapter 2.

3.1.1 Cellular Potts model

In our simulations, we consider different entities $\Sigma_\sigma :$ the choroid, the Bruch's membrane, retinal pigmented epithelium cells, endothelial cells, extracellular matrix, photoreceptors and drusen. We ignore the outer segments of photoreceptors and their dynamics. Thus, there is a free space between the RPE layer and the photoreceptors. We fix the number of drusen, N_{drusen}, and of RPE cells, N_{RPE}, whereas the number of ECs varies. Different cells comprise a number of elementary squares or pixels in a square domain Ω of side L (in numerical simulations, $L = 400$ μm). The precise labels of pixels belonging to different cells are classified depending on the entity

$$\sigma(\mathbf{x}) = \begin{cases} 0, & \text{if } \mathbf{x} \in \Sigma_{\text{ECM}}; \\ 1, \ldots, \ N_{\text{drusen}} + 1, & \text{if } \mathbf{x} \in \Sigma_{\text{BM}}; \\ N_{\text{drusen}} + 2 \ldots, \ 2N_{\text{drusen}} + 1, & \text{if } \mathbf{x} \in \Sigma_{\text{drusen}}; \\ 2N_{\text{drusen}} + 2 \ldots, \ 2N_{\text{drusen}} + 1 + N_{\text{RPE}}, & \text{if } \mathbf{x} \in \Sigma_{\text{RPE}}; \\ 2N_{\text{drusen}} + N_{\text{RPE}} + 2, \ldots & \text{if } \mathbf{x} \in \Sigma_{\text{EC}}. \end{cases} \tag{3.1.1}$$

For each pixel configuration, we define the Hamiltonian

$$\begin{aligned} H &= \sum_\sigma \rho_{\text{area}} \left(\frac{a_\sigma - A_\sigma}{A_\sigma} \right)^2 + \sum_\sigma \rho_{\text{peri.}} \left(\frac{p_\sigma - P_\sigma}{P_\sigma} \right)^2 + \sum_\sigma \rho_{\text{length}} \left(\frac{l_\sigma - L_\sigma}{L_\sigma} \right)^2 \\ &+ \sum_{\mathbf{x},\mathbf{x}'} \rho_{\text{adh}}^{\Sigma_\sigma,\Sigma_{\sigma'}} \left(1 - \delta_{\sigma,\sigma'}\right) + H_{\text{durot}} + H_{\text{chem}}, \end{aligned} \tag{3.1.2}$$

where the three first terms are sums over cells. These terms impel them to reach target areas, perimeters and lengths with strengths given by their Potts parameters ρ_j. The fourth term (haptotaxis) sums over all pixels and accounts for adhesion between elements. It is zero for pixels belonging to the same cell and calibrates the repulsion between pixels belonging to different cells (adhesion is stronger for smaller repulsion), depending on the value of the corresponding Potts parameter $\rho_{\text{adh}}^{\Sigma_\sigma,\Sigma_{\sigma'}}$. The fifth and sixth terms correspond to durotaxis and chemotaxis, impelling cells to move toward gradients of stiffness and VEGF concentration, respectively [125]. Detailed expressions for these terms are given in section 2.1. At each MCTS t, we select randomly a pixel $\mathbf{x}$, belonging to object Σ_σ, and propose to copy its spin $\sigma(\mathbf{x})$ to a neighboring (target) pixel $\mathbf{x}'$ that does not belong to $\Sigma_{\sigma(\mathbf{x})}$. The proposed copy in the spin configuration (spin flip) changes the configuration energy by an amount $\triangle H|_{\sigma(\mathbf{x})\to\sigma(\mathbf{x}')}$, and it is accepted with probability $P\left(\sigma(\mathbf{x}) \to \sigma(\mathbf{x}')\right)(t) = \{e^{-\Delta H|_{\sigma(\mathbf{x})\to\sigma(\mathbf{x}')}/T}, \Delta H > 0; 1, \Delta H \le 0\}$ (Metropolis algorithm) [88, 92]. The BM does not change throughout the simulation. Thus, MC attempts involving $\mathbf{x} \in \Sigma_{\mathrm{BM}}$ or $\mathbf{x}' \in \Sigma_{\mathrm{BM}}$ are discarded. An appropriate temperature for our simulations is $T = 4$. The values of the target areas, perimeters and lengths as well as the Potts parameters are listed in Tables 3.1–3.4. The length constraint does not apply to drusen or RPE.

Table 3.1: **Target areas, perimeters and length.**

Param.	A_{EC}	P_{EC}	L_{EC}	A_{RPE}	P_{RPE}	A_{druse}	P_{druse}
Value	$78\ \mu\mathrm{m}^2$	$50\ \mu\mathrm{m}$	$60\ \mu\mathrm{m}$	$169\ \mu\mathrm{m}^2$	$52\ \mu\mathrm{m}$	$2827\ \mu\mathrm{m}^2$	$188\ \mu\mathrm{m}$

Table 3.2: **Dimensionless Potts parameters.** Area, perimeter and length.

Param.	ρ_{area} (EC)	ρ_{peri} (EC)	ρ_{length} (EC)	ρ_{area} (RPE)	ρ_{peri} (RPE)	ρ_{area} (druse)	ρ_{peri} (druse)
Value	25000	75	180	100000	100	750000	500

Table 3.3: **Dimensionless Potts parameters.** Durotaxis, chemotaxis and adhesion.

Param.	ρ_{durot}	ρ^0_{chem}	$\rho^{\mathrm{EC,EC}}_{\mathrm{adh}}$	$\rho^{\mathrm{EC,ECM}}_{\mathrm{adh}}$	$\rho^{\mathrm{EC,RPE}}_{\mathrm{adh}}$	$\rho^{\mathrm{EC,druse}}_{\mathrm{adh}}$
Value	25	50000	70–80	40	60	80

Table 3.4: **Dimensionless Potts parameters.** Adhesion.

Param.	$\rho^{\mathrm{ECM,RPE}}_{\mathrm{adh}}$	$\rho^{\mathrm{BM,RPE}}_{\mathrm{adh}}$	$\rho^{\mathrm{druse,RPE}}_{\mathrm{adh}}$	$\rho^{\mathrm{RPE,RPE}}_{\mathrm{adh}}$	$\rho^{\mathrm{druse,ECM}}_{\mathrm{adh}}$	$\rho^{\mathrm{druse,druse}}_{\mathrm{adh}}$
Value	40	0–30	160	80–90	80	200

3.1.2 Continuum fields at the extracellular scale

VEGF concentration

The VEGF concentration $C(x, y, t)$ obeys the following initial-boundary value problem [125]:

$$\frac{\partial C}{\partial t} = D_f \left(\frac{\partial^2 C}{\partial x^2} + \frac{\partial^2 C}{\partial y^2} \right) - \nu\, C - G(x, y, C) + A(x, y),\ (x, y) \in \Omega,\ t > 0, \quad (3.1.3)$$

$$C(0, y, t) = 0 = C(L, y, t),\ C(x, 0, t) = 0 = C(x, L, t),\ (x, y) \in \partial\Omega,\ t > 0, \quad (3.1.4)$$

$$\mathbf{n} \cdot \nabla C(x, y, t) = 0,\ (x, y) \in x_{\mathrm{h}} \times \{y_{\mathrm{d}}, y_{\mathrm{u}}\} \cup \{x_{1\mathrm{l}}, x_{1\mathrm{r}}, x_{2\mathrm{l}}, x_{2\mathrm{r}}\} \times y_{\mathrm{v}}, t > 0, \quad (3.1.5)$$

$$C(x, y, 0) = 0,\ (x, y) \in \Omega. \quad (3.1.6)$$

where $y_{\mathrm{d}} = 246\ \mu\mathrm{m},\ y_{\mathrm{u}} = 248\ \mu\mathrm{m}, y_{\mathrm{v}} = [y_{\mathrm{d}}, y_{\mathrm{u}}],\ x_{1\mathrm{l}} = 72\ \mu\mathrm{m},\ x_{1\mathrm{r}} = 128\ \mu\mathrm{m},\ x_{2\mathrm{l}} = 272\ \mu\mathrm{m},\ x_{2\mathrm{r}} = 328\ \mu\mathrm{m},\ x_{\mathrm{h}} = [0\ \mu\mathrm{m}, x_{1\mathrm{l}}] \cup [x_{1\mathrm{r}}, x_{2\mathrm{l}}] \cup [x_{2\mathrm{r}}, 400\ \mu\mathrm{m}]$ are the points in which the Bruch's membrane is located with the corresponding holes. In Eq. (3.1.3), the amount of VEGF bound by an EC per unit time is

$$G(x, y, C) = \begin{cases} \Gamma, & \text{if } \Gamma \leq \upsilon\, C(x, y) \text{ and } (x, y) \in \Sigma_{\mathrm{EC}}, \\ \upsilon\, C, & \text{if } 0 \leq \upsilon\, C(x, y) < \Gamma \text{ and } (x, y) \in \Sigma_{\mathrm{EC}}, \\ 0, & \text{if } (x, y) \notin \Sigma_{\mathrm{EC}}, \end{cases} \quad (3.1.7)$$

where $\upsilon = 1\ \mathrm{h}^{-1}$, $D_f = 0.036\ \mathrm{mm}^2/\mathrm{h}$, $\nu = 0.6498/\mathrm{h}$ and $\Gamma = 0.02\ \mathrm{pg}/(\mu\mathrm{m}^2\ \mathrm{h})$ is the maximum amount of VEGF that it could be consumed by a cell per hour [90,99,125]. In eq. (3.1.3), the VEGF source due to the hypoxia caused by drusen and photoreceptors is

$$\begin{aligned} A(x, y) = & \sum_{i=1}^{N_{\mathrm{drusen}}} \alpha_i \exp\left\{ - \left[\frac{\left(x - x^{d_i}\right)^2}{2\sigma_x^2} + \frac{\left(y - y^{d_i}\right)^2}{2\sigma_y^2} \right] \right\} \\ & + \sum_{i=1}^{N_{\mathrm{photo}}} \alpha_i \exp\left\{ - \left[\frac{(x - x^{p_i})^2}{2\sigma_x^2} + \frac{(y - y^{p_i})^2}{2\sigma_y^2} \right] \right\}. \end{aligned} \quad (3.1.8)$$

Here the coefficient α_i is the amplitude, (x^{d_i}, y^{d_i}) or (x^{p_i}, y^{p_i}) is the center and σ_x, σ_y are the x and y spreads of the blob, $\sigma_x = \sigma_y = 7$. After a sprout arrives nearby a drusen, the surrounding region ceases to be hypoxic, therefore the corresponding Gaussian of the first summation disappears from $A(x, y)$.

Durotaxis

ECs generate mechanical strains in the substrate, perceive a stiffening of the substrate along the strain orientation, and extend preferentially on stiffer substrate. The simulated ECs spread out on stiff matrices, contract on soft matrices, and become elongated on matrices of intermediate stiffness [92]. Strains enter the durotaxis term in the Hamiltonian (3.1.2) with technical details about the elasticity equations explained in section 2.1.

3.1.3 Signaling processes and cell dynamics

A crucial distinction between ECs is that between tip and stalk phenotypes. Tip cells are highly motile, do not proliferate, act as leaders of angiogenic sprouts, sense chemical gradients and advance towards VEGF sources produced by hypoxic cells. Stalk cells proliferate and are less motile, often following tip cells. The tip-stalk cell phenotype is selected by the Notch signaling communication pathway, which is quantified by model differential equations explained in section 2.1. The unknowns in these equations are the Notch, Delta-4, and Jagged-1 proteins in a cell, and the number Notch intracellular domain and VEGF molecules and of VEGF receptors in the cell. The phenotype of a cell is decided by whether the number of its VEGF molecules surpass appropriate thresholds [110]. See the precise criterion in Ref. [125] and in section 2.1. This means that stalk cells may become tip cells and vice versa. There are also hybrid stalk-tip cells that can lead thinner angiogenic sprouts [110,125]. Advancing blood vessels may undergo branching, thereby creating new sprouts, and fuse with existing vessels (anastomosis). Branching is only allowed between BM and photoreceptors. The details are explained in Ref. [125] and section 2.1.

3.1.4 Retinal configuration and onset of angiogenesis

We consider a simplified configuration for the space (measuring about $L = 400\,\mu$m) between the choroid and the photoreceptors as sketched in Fig. 1.3 of section 1.1. The choroid contains several layers comprising blood vessels of different sizes, including narrow capillaries. In a 2D section, choriocapillaries oriented in different directions may issue angiogenic sprouts that are then attracted towards openings in the BM and the RPE layer. Instead of modeling the fixed choriocapillaries (parent vessels) issuing new blood vessels, we randomly generate a fixed number of points $N_{\rm pv}$ that may initiate sprouts and establish an external VEGF activation threshold for the sprouts to start. The parent vessels are randomly placed at the rectangle $0 < x < L$, $0 < y < 0.3L = 120\,\mu$m and the concentration of external VEGF satisfies Eqs. (3.1.3) - (3.1.6). The $2\,\mu$m wide BM is a segment placed at $y = 246\,\mu$m [57, 126] and it is followed by RPE cells with interspersed drusen, which have Gaussian sources of VEGF representing hypoxic areas. These sources placed at $y = 249\,\mu$m are farther than 100 μm from the choriocapillaries, which is consistent with the criterion for hypoxia to occur. New sprouts grow from the initial points only if the external VEGF concentration in them is larger than a threshold. The described CPM causes the sprouts to advance toward the drusen and they may or may not pass the BM and RPE attracted by the VEGF sources at the photoreceptors.

After the CPM simulation begins, we need a criterion for RPE cells and photoreceptors to become hypoxic and issue VEGF. During the first hundreds of MCTS, RPE cells and drusen grow to acquire their target size [117, 127]. Once a drusen i reaches forty percent of its target size, it produces a hole in the BM, the RPE cells around it become hypoxic and start producing VEGF. The VEGF source associated with drusen i is represented by a Gaussian function centered at $\left(x^{d_i}, y^{d_i}\right)$. This process also activates N_{photo} sources of VEGF associated with photoreceptors equally spaced on the x axis at $y = 388\,\mu$m. We ignore the photoreceptors outer segments and their dynamics. As in the case of the sources associated with drusen, these VEGF sources are represented by Gaussian functions centered at $(x^{p_j}, y^{p_j} = 388\,\mu\text{m})$ [128]. The holes divide the BM into $N_{\text{drusen}}+1$ pieces. Once VEGF sources are activated, new sprouts can start from the parent vessels at their predetermined sites if the external VEGF concentration there surpasses the activation threshold. VEGF sources stop emitting it when they are reached by ECs.

3.2 Numerical results

Different adhesion parameters between ECs and between RPE and BM cells characterize haptotaxis, which, together with VEGF gradients, determine the formation and type of CNV [117]. In addition to confirming impaired lateral adhesion between BM and RPE and between RPE cells themselves as major drives of CNV, we explore how adhesion between ECs, chemotaxis and Notch signaling affect CNV. We find that Notch signaling proteins are markers of the CNV type that develops during AMD. Additionally, reducing the production of Jagged may inhibit CNV and, therefore, stop AMD. A detailed description of the simulation code can be found in Chapter 5.

3.2.1 Impaired adhesion

Adhesion defects modify the pattern of choroidal neovascularization in the retina [117]. The adhesion Potts parameter measures the energetic cost for cells to stay together: it is zero for pixels of the same cell and it is larger for pixels of different cells. The larger the Potts parameter between pixels of different cells is, the stronger these neighboring cells repel each other (thereby meaning weaker adhesion among them). Thus, impared adhesion among cells implies that the corresponding Potts parameter has increased with respect to the normal adhesion values. We now consider the effect that modifying Potts parameters for different cell types has on the formation and type of CNV.

Adhesion between RPE and BM

Reducing the adhesion between the basement membrane of the RPE and the BM may enable CNV to invade the sub-RPE space [117, 129]. As chemotaxis attracts vessel sprouts towards sites with higher VEGF concentration beyond the RPE, vessels may cross this layer at sites where adhesion is weakest, i.e., near drusen. If adhesion between RPE and the BM is weak (large Potts parameter), ECs move easily in the space between them, thereby producing type 1 CNV, as observed in the left panels of Fig. 3.1. If the Potts parameter decreases (central and right panels of Fig. 3.1), the adhesion between RPE and the BM increases. ECs then try to surpass the RPE near the drusen that have opened a hole in the BM. Eventually, the sprouts reach the subretinal space, whereby producing type 2 CNV. The resulting CNV does not form a dense network of blood vessels between RPE and BM.

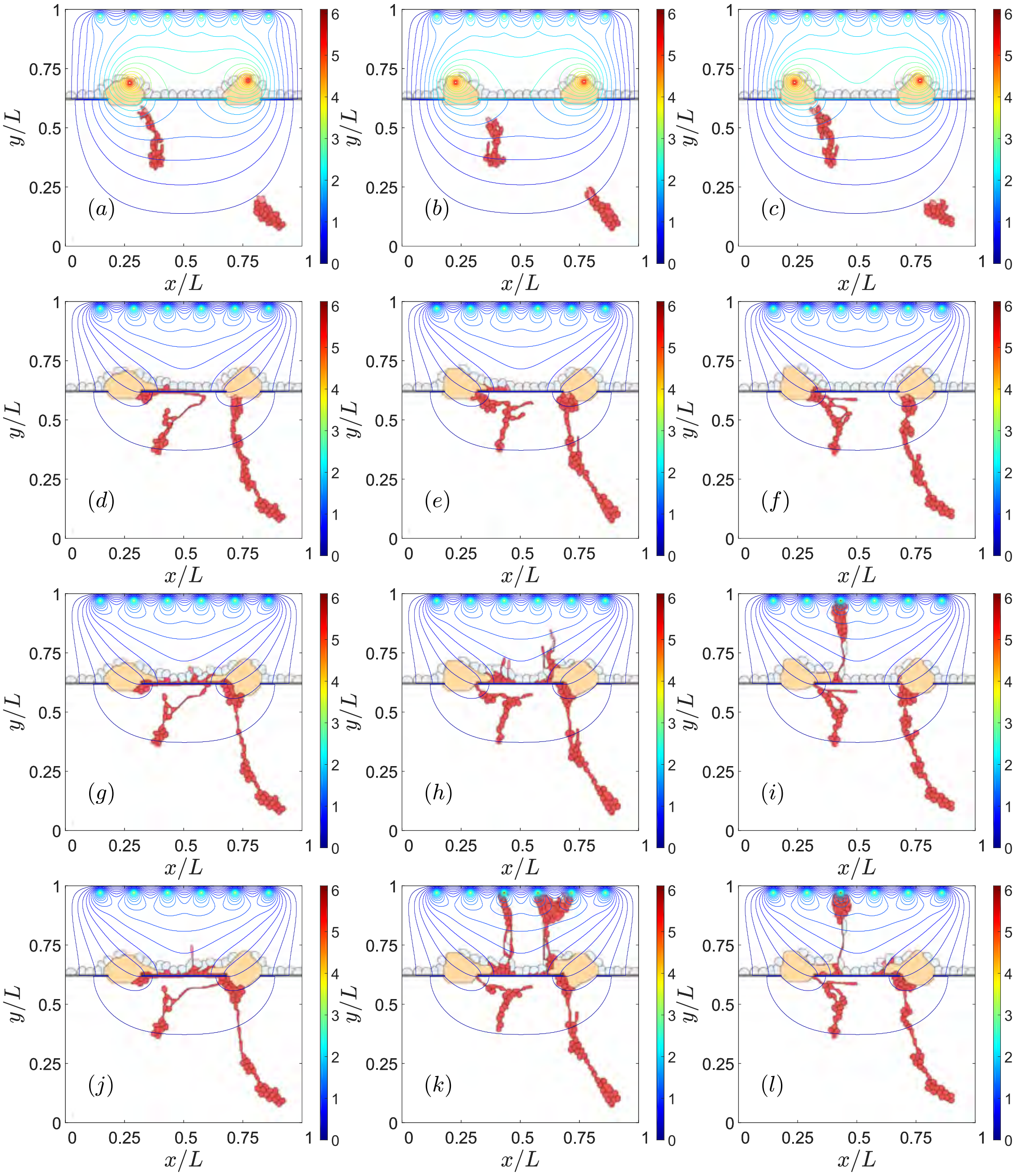

Figure 3.1: **Effect of impaired adhesion between RPE and BM.** For $\rho_{\text{adh}}^{\Sigma_\sigma,\Sigma_{\sigma'}}$(RPE - BRM) $= 30$, snapshots at times: (a) 601 MCTS, (d) 1601 MCTS, (g) 4501 MCTS, (j) 9001 MCTS. For $\rho_{\text{adh}}^{\Sigma_\sigma,\Sigma_{\sigma'}}$(RPE - BRM) $= 6$, snapshots at times: (b) 601 MCTS, (e) 1601 MCTS, (h) 4501 MCTS, (k) 9001 MCTS. For $\rho_{\text{adh}}^{\Sigma_\sigma,\Sigma_{\sigma'}}$(RPE - BRM) $= 0$, snapshots at times: (c) 601 MCTS, (f) 1601 MCTS, (i) 4501 MCTS, (l) 9001 MCTS.

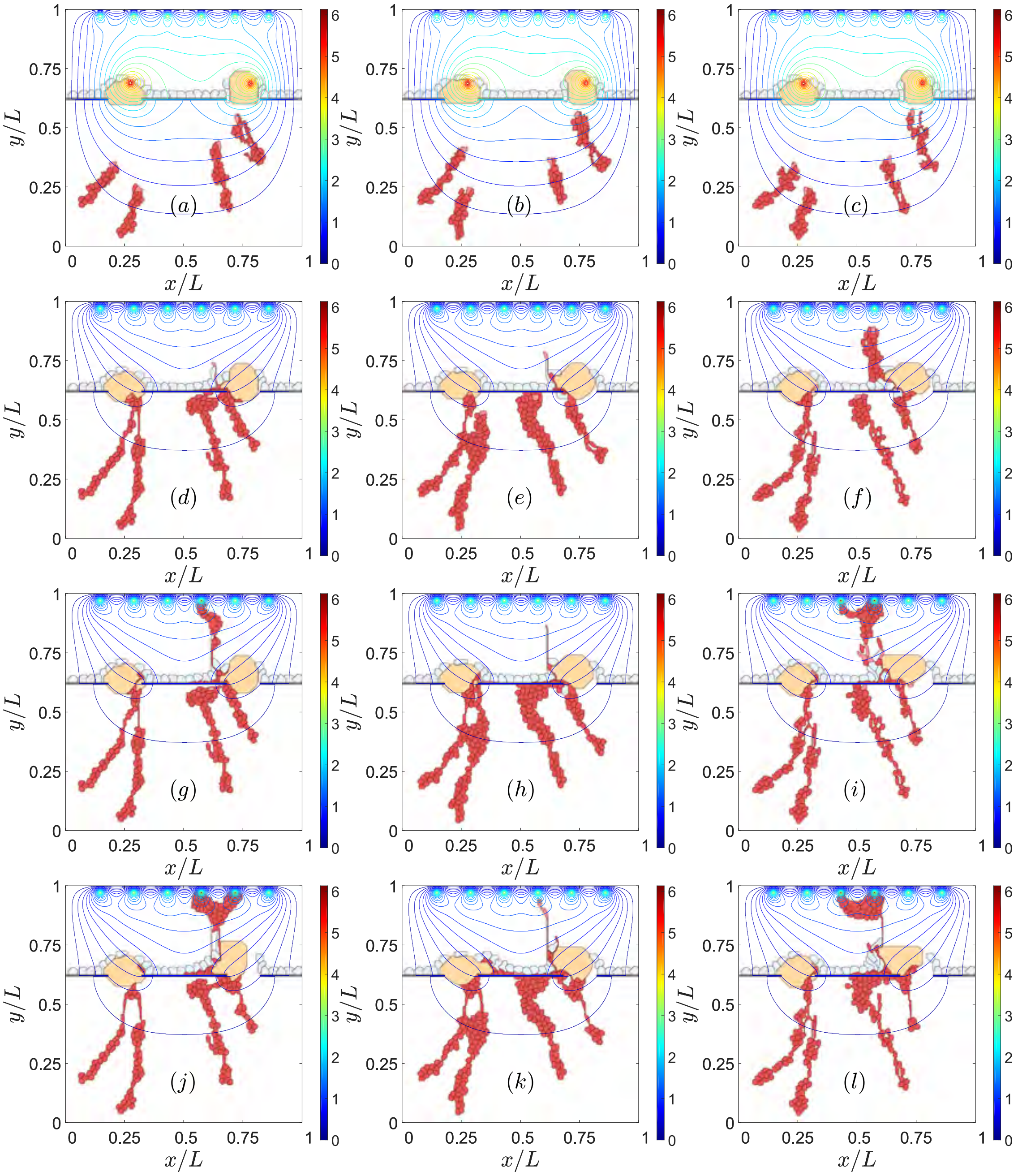

Figure 3.2: **Effect of impaired adhesion between RPE - RPE & EC - EC.** For $\rho_{\text{adh}}^{\Sigma_\sigma,\Sigma_{\sigma'}}$(EC-EC) $= 70$, $\rho_{\text{adh}}^{\Sigma_\sigma,\Sigma_{\sigma'}}$(RPE cell - RPE cell) $= 90$, snapshots at times: (a) 601 MCTS, (d) 1801 MCTS, (g) 3601 MCTS, (j) 8001 MCTS. For $\rho_{\text{adh}}^{\Sigma_\sigma,\Sigma_{\sigma'}}$(EC-EC) $= 70$, $\rho_{\text{adh}}^{\Sigma_\sigma,\Sigma_{\sigma'}}$(RPE cell - RPE cell) $= 80$, snapshots at times: (b) 601 MCTS, (e) 1801 MCTS, (h) 3601 MCTS, (k) 8001 MCTS. For $\rho_{\text{adh}}^{\Sigma_\sigma,\Sigma_{\sigma'}}$(EC-EC) $= 80$, $\rho_{\text{adh}}^{\Sigma_\sigma,\Sigma_{\sigma'}}$(RPE cell - RPE cell) $= 80$, snapshots at times: (c) 601 MCTS, (f) 1801 MCTS, (i) 3601 MCTS, (l) 8001 MCTS.

RPE - RPE & EC - EC adhesion

Impaired lateral adhesion between RPE cells facilitates type 2 CNV [130,131]. ECs and the sprouts they generate are able to penetrate the RPE layer effortlessly, as shown in the left column of Fig. 3.2. Stronger adhesion between cells in RPE makes it difficult for sprouts to cross the layer, thereby favoring type 1 over type 2 CNV, as shown in the middle column of Fig. 3.2.

While adhesion between endothelial cells affects the quality of the resulting blood vessels [107], it also influences the resulting type of CNV, cf the middle and right columns of Fig. 3.2. Reduced adhesion between ECs has the consequences displayed on the right column of Fig. 3.2: ECs are able to intersperse RPE cells and drusen to change quickly from type 1 to type 2 CNV. This produces blood vessels of poorer quality. Strong EC-EC adhesion makes it difficult for the sprout to pass through RPE cells since the ECs have to disconnect from their EC neighbors to cross the RPE, as shown by the middle column of Fig. 3.2.

To sum up, Fig 3.2 shows that we can favor type 1 CNV and prevent type 2 CNV by making stronger the adhesion between cells in RPE (from left column to middle column). In addition, if the adhesion between ECs weakens, poor quality sprouts will pass RPE layer and produce type 2 CNV (middle and right columns of Fig 3.2).

3.2.2 Sources of VEGF

High levels of VEGF concentration generated by sources produce large VEGF gradients that drive sprouts, therefore being one chief cause of CNV [132]. This is illustrated by Fig. 3.3. The VEGF concentration at the sources in this figure increases from the left column to the middle and right ones, whereas time as measured by MCTS increases from top to bottom. If the level of VEGF is too low, the ECs at the walls of the choroid vessels do not have enough VEGF to activate and start to develop a sprout, as shown on the left column of Fig. 3.3. Medium and high levels of VEGF concentration produce CNV, cf middle and right column of Fig. 3.3. On the middle column of this figure, only two of the four possible choroid vessels that emit sprouts have been activated, whereas all four sites have been activated on the right column of Fig. 3.3. The subsequent larger chemotaxis causes the sprouts to reach the let drusen earlier on the right column of Fig. 3.3 than on its middle column. The larger levels of VEGF favor the faster evolution from type 1 to type 2 CNV shown on the right column of Fig. 3.3.

The value of the VEGF gradient at the point where the sprout tries to cross the RPE determines the sprout chances of starting type 2 CNV. The VEGF concentration throughout the domain and the parameter values are the same for Figs. 3.4 and 3.5, which have a different seed of the random number generator that determines the sprout initiation points. The local VEGF gradient at the point where the sprouts are closer to the end of the RPE layer is larger for Fig. 3.5 than for Fig. 3.4. The larger chemotactic force experienced by the leading EC implies that type 2 CNV is produced in Fig. 3.5 while only type 1 CNV is observed in Fig. 3.4. The right columns of figures 3.4 and 3.5 depict the number of active VEGF receptors at the times corresponding to panels on the left columns. It is clear that the number of active VEGF receptors is larger when there is successful type 2 CNV, as in Fig. 3.5, as compared with type 1 CNV as in Fig. 3.4. Having the same adhesion and VEGF concentration do not determine the type of CNV. The setup of the parent vessels in the choroid may generate different CNV outcomes.

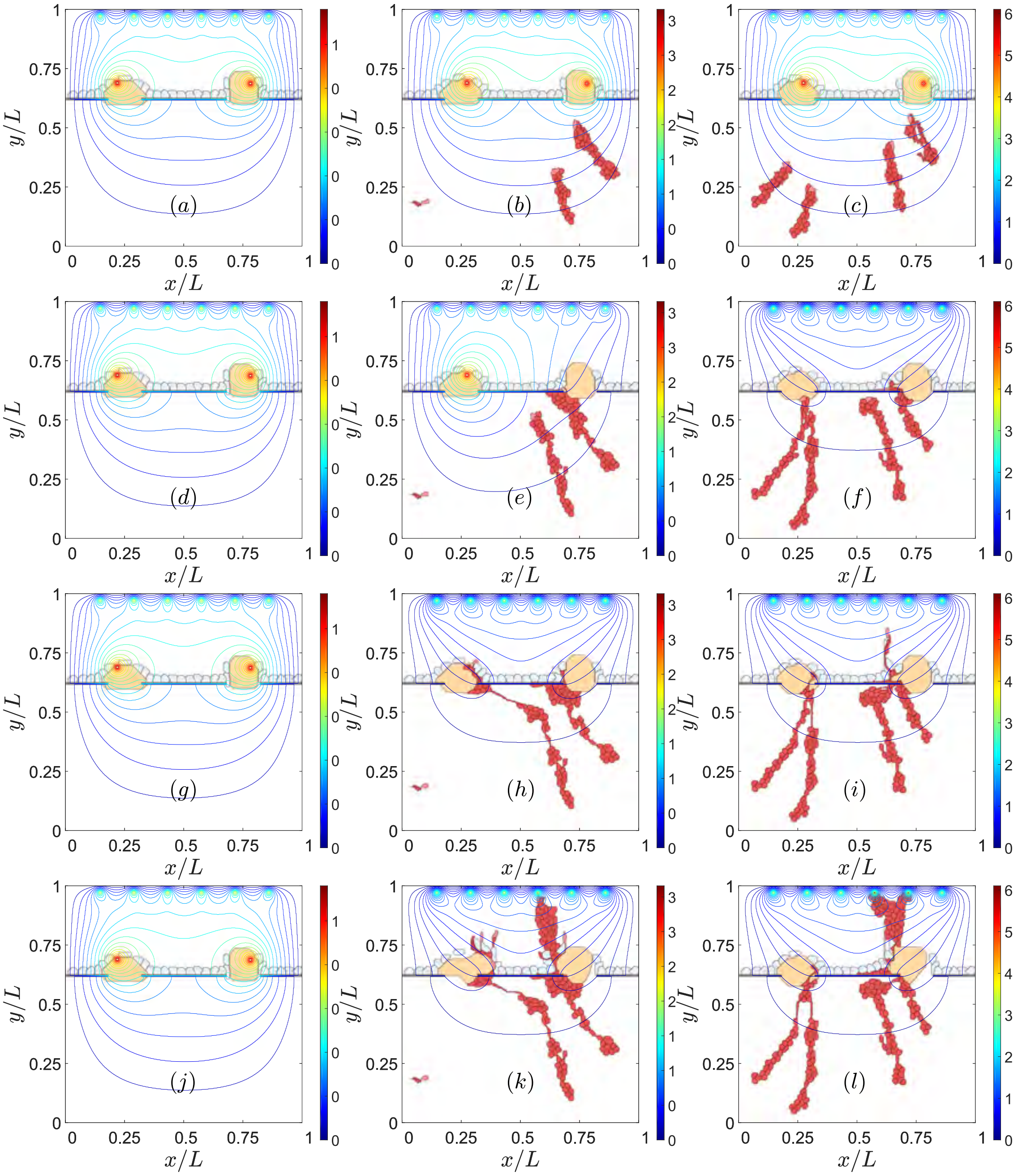

Figure 3.3: **Effect of the VEGF concentration at the sources.** For $\alpha_i = 4.01 \times 10^{-4} = 0.000401$, snapshots at times: (a) 601 MCTS, (d) 1201 MCTS, (g) 3001 MCTS, (j) 5201 MCTS. For $\alpha_i = 1.203 \times 10^{-3} = 0.001203$, snapshots at times: (b) 601 MCTS, (e) 1201 MCTS, (h) 3001 MCTS, (k) 5201 MCTS. For $\alpha_i = 2.005 \times 10^{-3} = 0.002005$, snapshots at times: (c) 601 MCTS, (f) 1201 MCTS, (i) 3001 MCTS, (l) 5201 MCTS.

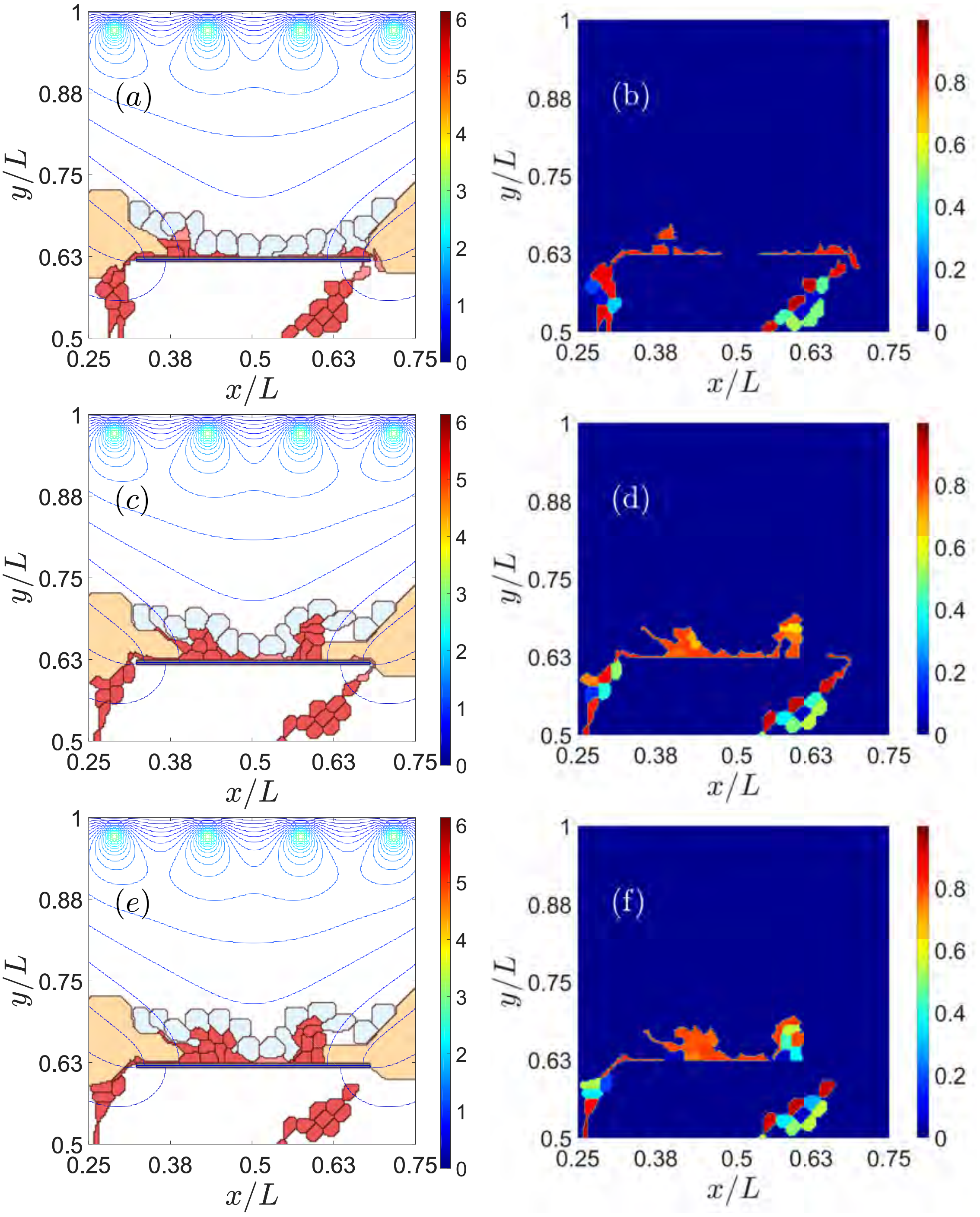

Figure 3.4: **Type 1 CNV due to the lack of VEGF in the point where the tip cell of the sprout tries to cross the RPE** (left column: (a), (c), (e)). Amount of VEGF receptors of ECs (right column: (b), (d), (f)). Snapshots at times: (a), (b) 1501 MCTS, (c), (d) 4501 MCTS, (e), (f) 9001 MCTS

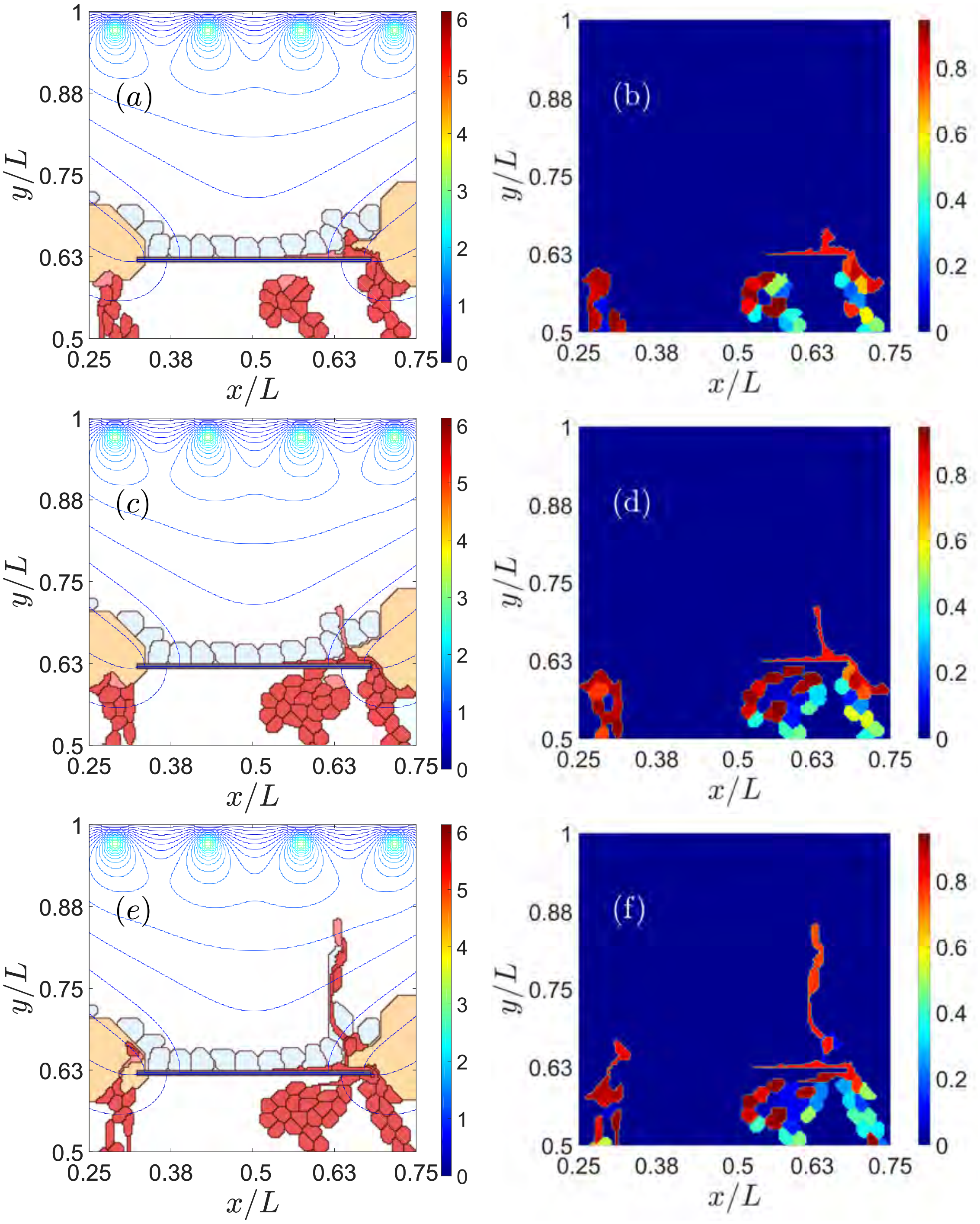

Figure 3.5: **Type 2 CNV favored by the point where the sprout cross the RPE** (left column: (a), (c), (e)). Amount of VEGF receptors of ECs (right column: (b), (d), (f)). Snapshots at times: (a), (b) 1201 MCTS, (c), (d) 1501 MCTS, (e), (f) 3001 MCTS

3.2.3 Notch signaling

While Figs. 3.4 and 3.5 show the effect of active VEGF receptors on retinal CNV, other proteins involved in the Notch signaling pathway may characterize the resulting CNV network.

Jagged and Delta dynamics determine sprouting [125], therefore also CNV. The thresholds of Delta concentration of cells to change the phenotype depend on the Jagged production rate. The simulations shown previously have a Jagged production rate, r_J, of 2000 and a Delta production rate, r_D, of 1000. The chosen values correspond to pathological angiogenesis [125], which is the most similar scenario to type 2 CNV. Figs. 3.6 and 3.7 show the effect of decreasing r_J in the left column and increasing r_D in the right column from the reference simulation placed in the middle of the figures. The reference simulation in Fig. 3.6 is the one corresponding to middle column in Fig. 3.1. The reference simulation in Fig. 3.7 is the one corresponding to right column in Fig. 3.2. In both figures, 3.6 and 3.7, reducing the Jagged production rate, left column, favors type 1 over type 2 CNV and makes the blood vessels thicker than the ones in the middle column. However, the increase of the Delta production rate does not prevent type 2 CNV. We also observe that the resulting blood vessels are thinner and worse organized than the ones in the middle column.

In order to distinguish pathological from physiological angiogenesis we can display the content of VEGF in the tip, stalk and hybrid tip-stalk cells, V, versus the external VEGF, $V_{\text{ext}} = C$, or versus the Jagged content J [125].

Fig. 3.8 shows the content of VEGF, V, versus $V_{\text{ext}} = C$, and of V versus J in the tip, stalk and hybrid tip-stalk cells within the angiogenic network of Fig. 3.6 at 9001 MCTS. We recall that the left column of Fig. 3.6 exhibits type 1 CNV, whereas the other columns display type 2 CNV. With respect to Fig. 3.8(a), Fig. 3.8(c) shows that the number of hybrid cells has increased considerably and appear for a wider range of external VEGF.

Fig. 3.8(e) is similar to Fig. 3.8(c), but the hybrid cells are more concentrated around lower external VEGF values. With respect to Fig. 3.8(b), Fig. 3.8(d) exhibits a wider range of Jagged for hybrid and stalk cells. Hybrid cells with higher Jagged do not behave as actual tip cells, they are more erratic, which correspond to a pathological angiogenesis and clearly type 2 CNV. Fig. 3.8(f) is in an intermediate state between Fig. 3.8(b) and Fig. 3.8(d) but the hybrid cells have low Jagged. We can classify Fig. 3.8(a) & Fig. 3.8(b) and Fig. 3.8(e) & Fig. 3.8(f) in physiological angiogenesis despite Fig. 3.8(e) & Fig. 3.8(f) correspond to a type 2 CNV. Similar behavior is shown in Fig. 3.9 corresponding to Fig. 3.7.

Fig. 3.10 shows the content of VEGF, V, versus $V_{\text{ext}} = C$, and of V versus J in the tip, stalk and hybrid tip-stalk cells within the angiogenic network of Fig. 3.1 at 9001 MCTS. We recall that the left column of Fig. 3.1 exhibits type 1 CNV, whereas the other columns display type 2 CNV. With respect to Fig.3.10(a), Figs. 3.10(c) and (e) show that the number of hybrid cells has increased considerably and appear for a wider range of external VEGF. With respect to Fig. 3.10(b), Figs. 3.10(d) and (f) exhibit the same trend as J increases. The proliferation of stalk cells beyond that of tip cells as J increases is a sign of pathological angiogenesis (abundant thin sprouts often led by hybrid-tip cells) [125]. Thus, type 2 CNV clearly corresponds to pathological angiogenesis and can be distinguish by the graphs in Figs. 3.10(c)-(f). Fig. 3.10(a), with a well separated content of V between tip and stalk cells, indicates that type 1 CNV is closer to physiological angiogenesis. However, Fig. 3.10(b) shows that stalk cells also proliferate when compared to tip cells as J increases, which is a sign of pathological angiogenesis [125]. Similar behavior is shown in Fig. 3.11 corresponding to Fig. 3.2. Figs. 3.11(c)-(d) are similar to Figs. 3.10(a)-(b), thereby indicating type 1 CNV, which is confirmed by the middle column of Fig. 3.2. The other panels in Fig. 3.11 indicate type 2 CNV, the same as the left and right columns of Fig. 3.2.

Tables 3.5 and 3.6 may help to understand figures 3.8, 3.9, 3.10, 3.11.

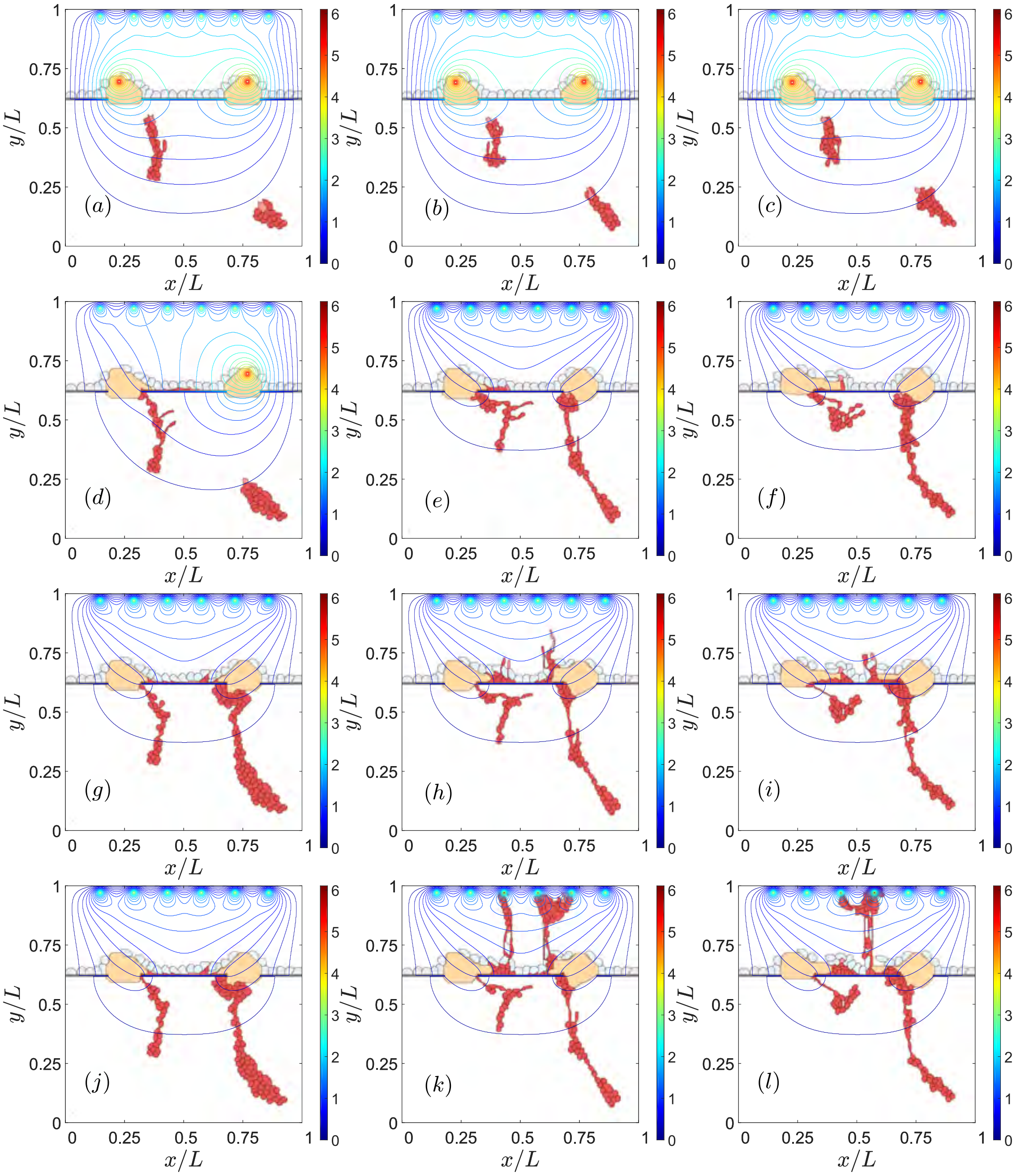

Figure 3.6: **Effect of Jagged and Delta production on CNV.** For $r_J = 500$ molec/h, $r_D = 1000$ molec/h, snapshots at times: (a) 601 MCTS, (d) 1601 MCTS, (g) 4501 MCTS, (j) 9001 MCTS. For $r_J = 2000$ molec/h, $r_D = 1000$ molec/h, snapshots at times: (b) 601 MCTS, (e) 1601 MCTS, (h) 4501 MCTS, (k) 9001 MCTS. For $r_J = 2000$ molec/h, $r_D = 7500$ molec/h, snapshots at times: (c) 601 MCTS, (f) 1601 MCTS, (i) 4501 MCTS, (l) 9001 MCTS.

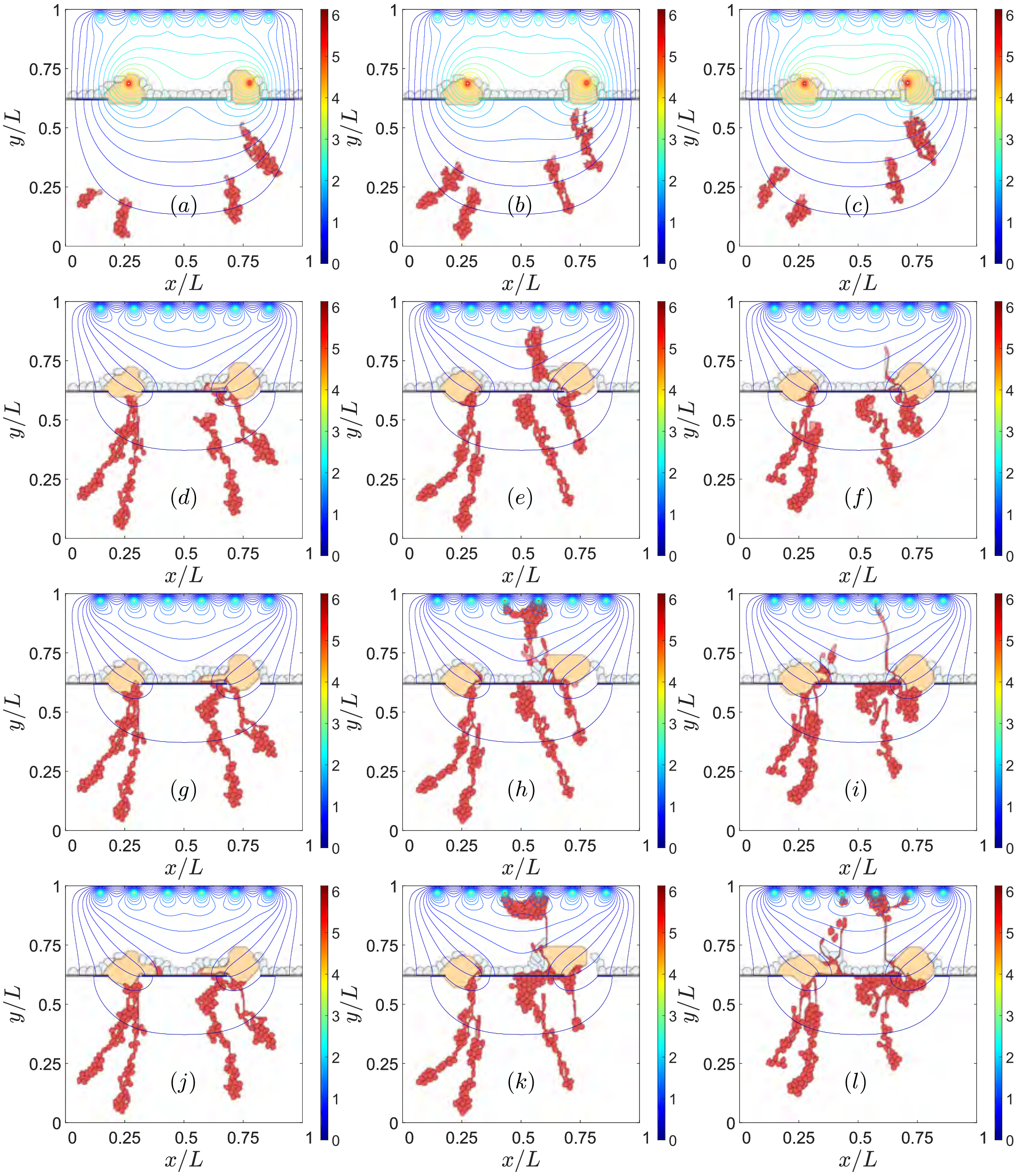

Figure 3.7: **Effect of Jagged and Delta production on CNV.** For $r_J = 500$ molec/h, $r_D = 1000$ molec/h, snapshots at times: (a) 601 MCTS, (d) 1801 MCTS, (g) 3601 MCTS, (j) 8001 MCTS. For $r_J = 2000$ molec/h, $r_D = 1000$ molec/h, snapshots at times: (b) 601 MCTS, (e) 1801 MCTS, (h) 3601 MCTS, (k) 8001 MCTS. For $r_J = 2000$ molec/h, $r_D = 7500$ molec/h, snapshots at times: (c) 601 MCTS, (f) 1801 MCTS, (i) 3601 MCTS, (l) 8001 MCTS.

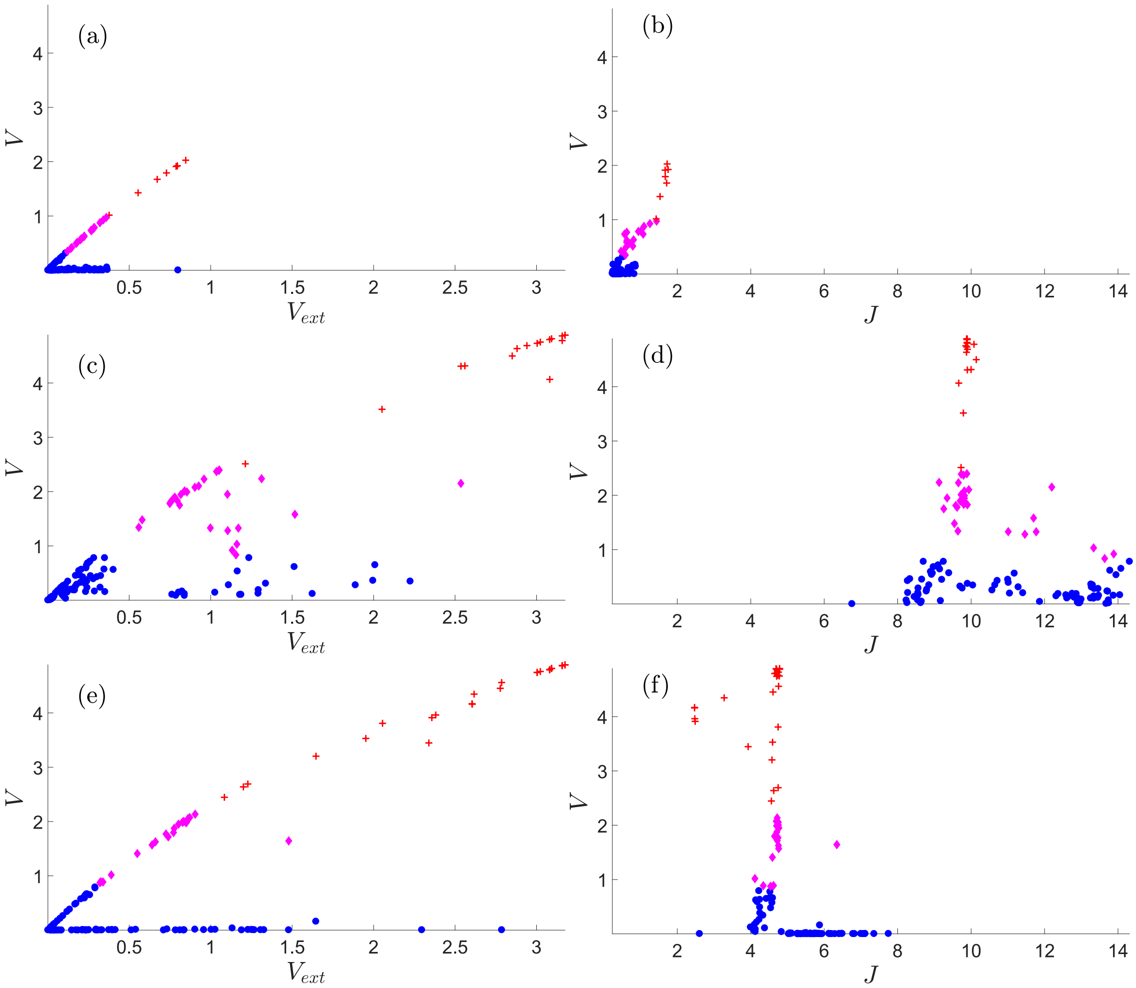

Figure 3.8: **Content of VEGF, V, versus $V_{\text{ext}} = C$, and of V versus J in the tip, stalk and hybrid tip-stalk cells within the angiogenic network at 9001 MCTS.** (a), (b) $r_J = 500$ molec/h, $r_D = 1000$ molec/h (Fig. 3.6 left column); (c), (d) $r_J = 2000$ molec/h, $r_D = 1000$ molec/h (Fig. 3.6 middle column); (e), (f) $r_J = 2000$ molec/h, $r_D = 7500$ molec/h (Fig. 3.6 right column). The meaning of symbols is as follows. Red cross (tip cell), magenta rhombus (hybrid tip/stalk cell), blue circle (stalk cell).

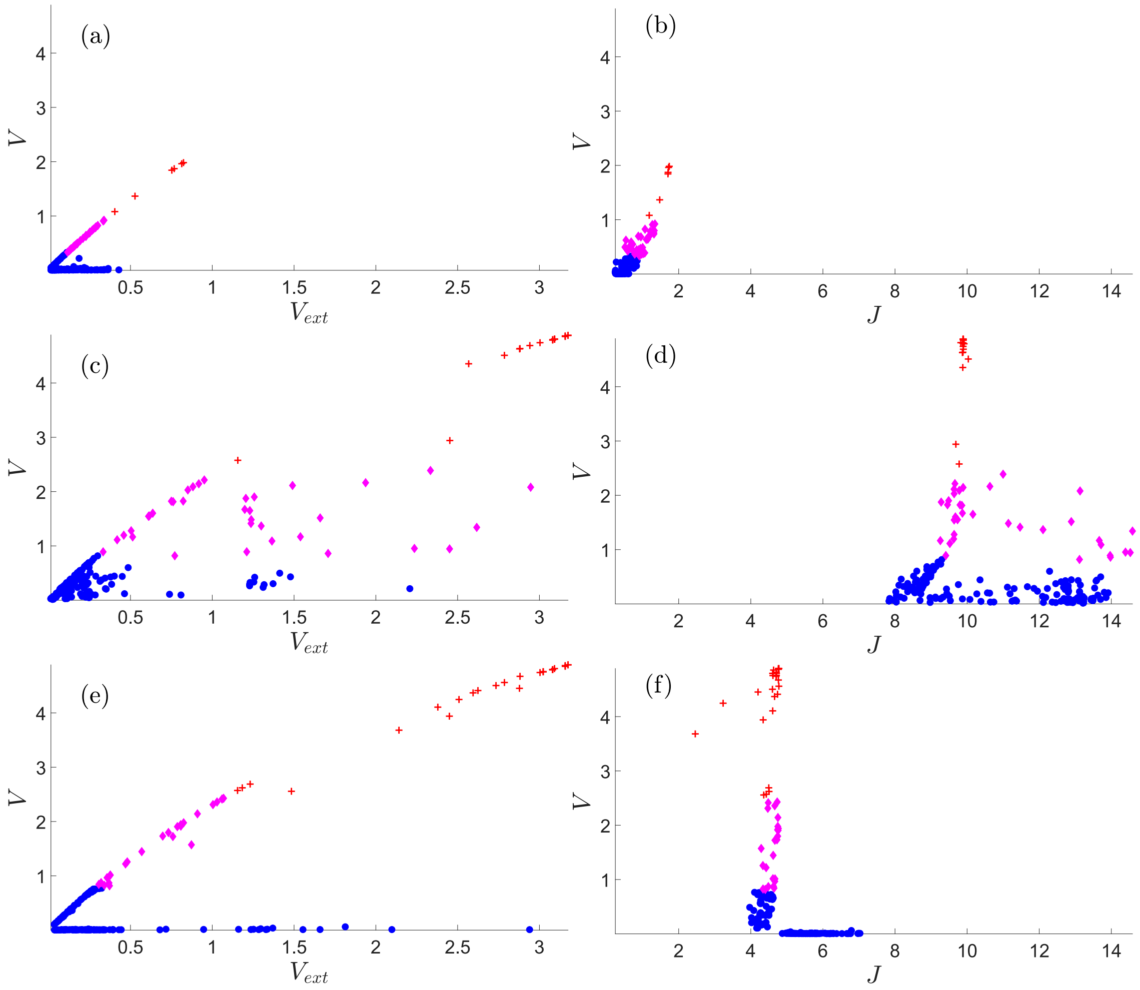

Figure 3.9: **Content of VEGF, V, versus $V_{\text{ext}} = C$, and of V versus J in the tip, stalk and hybrid tip-stalk cells within the angiogenic network at 8001 MCTS.** (a), (b) $r_J = 500$ molec/h, $r_D = 1000$ molec/h (Fig. 3.7 left column); (c), (d) $r_J = 2000$ molec/h, $r_D = 1000$ molec/h (Fig. 3.7 middle column); (e), (f) $r_J = 2000$ molec/h, $r_D = 7500$ molec/h (Fig. 3.7 right column) The meaning of symbols is as follows. Red cross (tip cell), magenta rhombus (hybrid tip/stalk cell), blue circle (stalk cell).

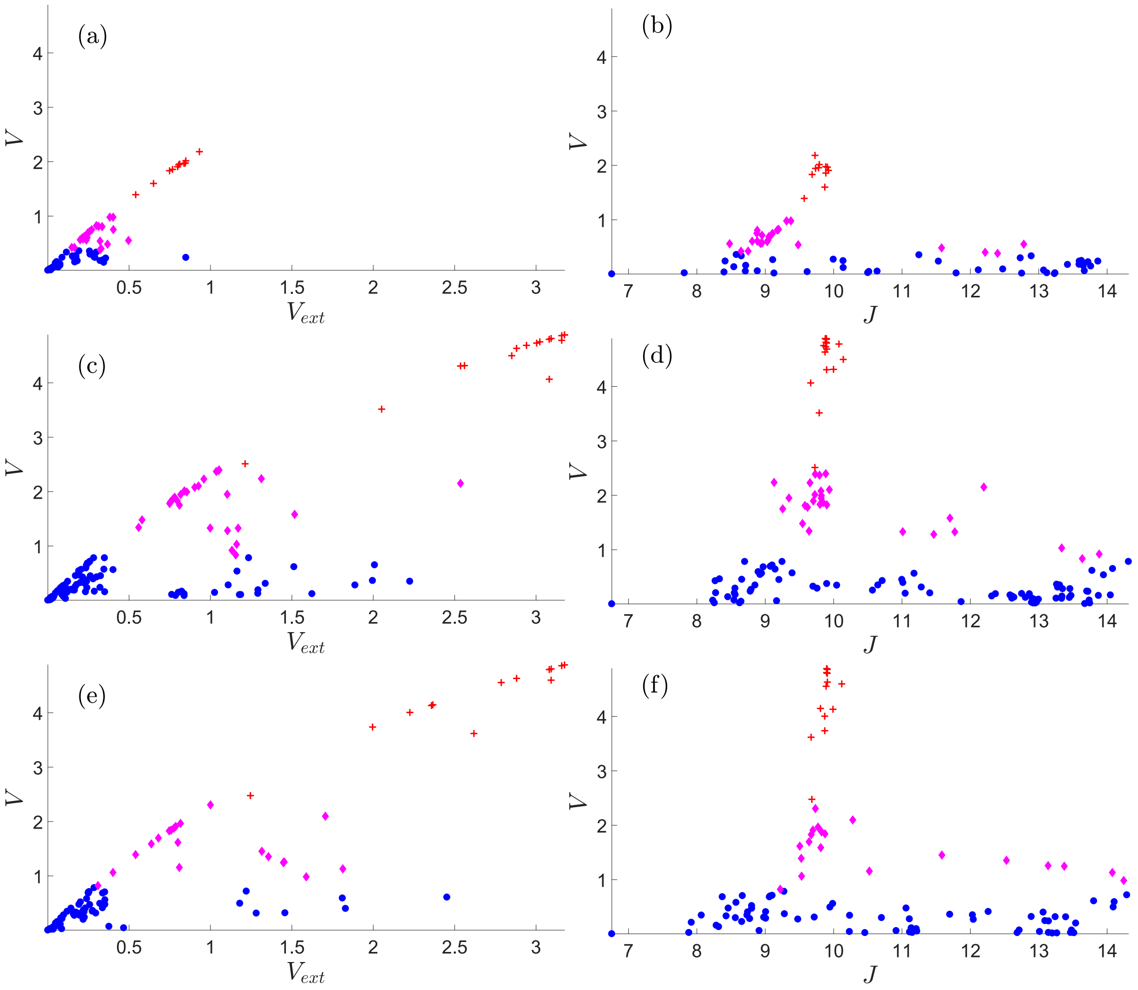

Figure 3.10: **VEGF content, V, versus $V_{\text{ext}} = C$, and versus Jagged content J in the tip, stalk and hybrid tip-stalk cells within the angiogenic network at 9001 MCTS.** (a), (b) $\rho_{\text{adh}}^{\Sigma_\sigma,\Sigma_{\sigma'}}$(RPE - BRM) $= 30$ (Fig. 3.1 left column); (c), (d) $\rho_{\text{adh}}^{\Sigma_\sigma,\Sigma_{\sigma'}}$(RPE - BRM) $= 6$ (Fig. 3.1 middle column); (e), (f) $\rho_{\text{adh}}^{\Sigma_\sigma,\Sigma_{\sigma'}}$(RPE - BRM) $= 0$ (Fig. 3.1 right column). The meaning of symbols is as follows. Red cross (tip cell), magenta rhombus (hybrid tip/stalk cell), blue circle (stalk cell).

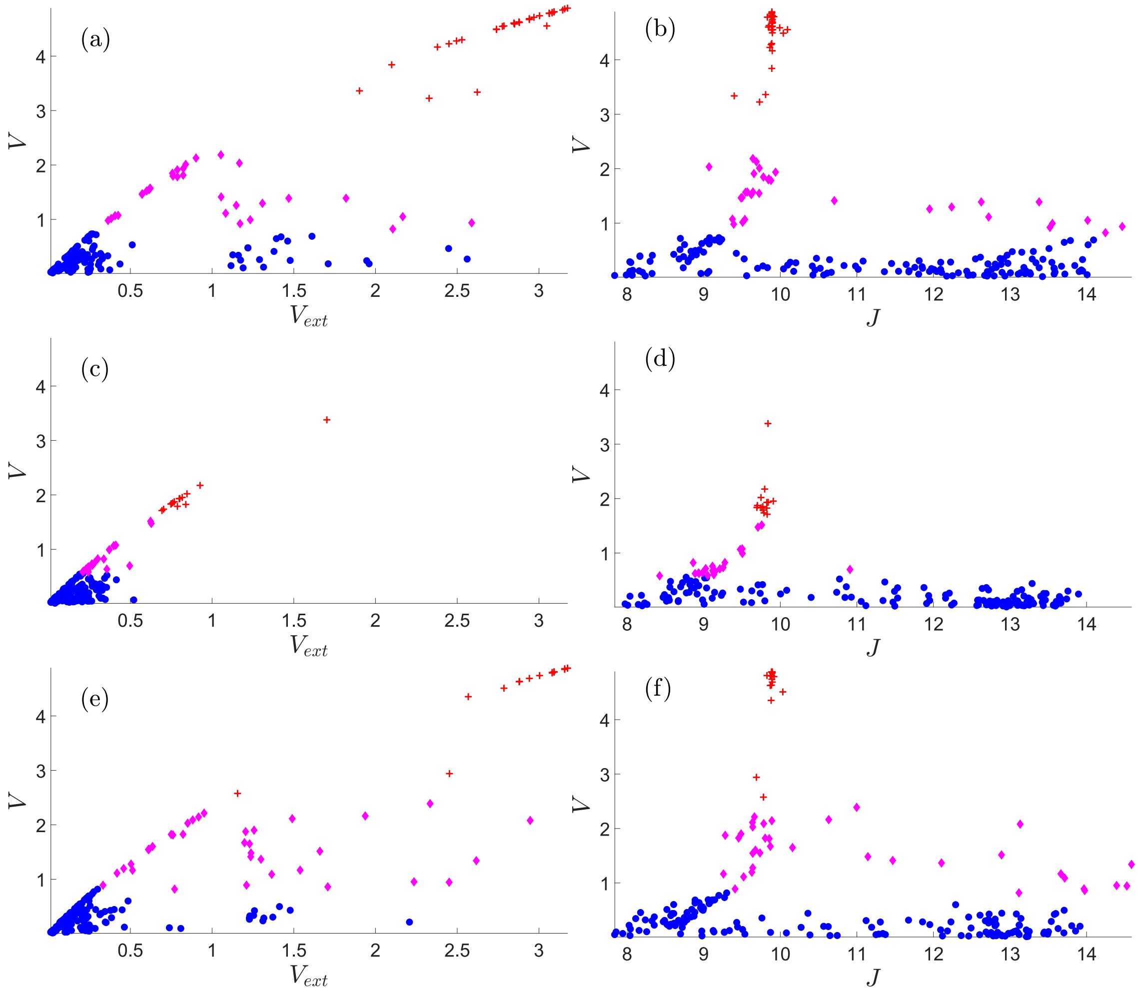

Figure 3.11: **Content of VEGF, V, versus $V_{\text{ext}} = C$, and of V versus J in the tip, stalk and hybrid tip-stalk cells within the angiogenic network at 8001 MCTS.** (a), (b) $\rho_{\text{adh}}^{\Sigma_\sigma,\Sigma_{\sigma'}}$(EC-EC) $= 70$, $\rho_{\text{adh}}^{\Sigma_\sigma,\Sigma_{\sigma'}}$(RPE cell - RPE cell) $= 90$ (Fig. 3.2 left column); (c), (d) $\rho_{\text{adh}}^{\Sigma_\sigma,\Sigma_{\sigma'}}$(EC-EC) $= 70$, $\rho_{\text{adh}}^{\Sigma_\sigma,\Sigma_{\sigma'}}$(RPE cell - RPE cell) $= 80$ (Fig. 3.2 middle column); (e), (f) $\rho_{\text{adh}}^{\Sigma_\sigma,\Sigma_{\sigma'}}$(EC-EC) $= 80$, $\rho_{\text{adh}}^{\Sigma_\sigma,\Sigma_{\sigma'}}$(RPE cell - RPE cell) $= 80$ (Fig. 3.2 right column). The meaning of symbols is as follows. Red cross (tip cell), magenta rhombus (hybrid tip/stalk cell), blue circle (stalk cell).

3.2.4 Summary

Figures	Correspond to	CNV	Notch signaling parameters and characterization
3.8(a), 3.8(b)	Fig. 3.6, left column. Notch signaling .	1	$r_J = 500\,; r_D = 1000\,.$ Well separated content of V between tip and stalk cells. Close to physiological angiogenesis.
3.8(c), 3.8(d)	Fig. 3.1, middle column. Impaired adhesion of RPE - BM . Fig. 3.6, middle column. Notch signaling .	2	$r_J = 2000\,; r_D = 1000\,.$ High proliferation of stalk cells for $J > J_{\text{tipmax}}\,.$ Pathological angiogenesis.
3.8(e), 3.8(f)	Fig. 3.6, right column. Notch signaling .	2	$r_J = 2000\,; r_D = 7500\,.$ High proliferation of stalk cells for $J > J_{\text{tipmax}}\,.$ Pathological angiogenesis.
3.9(a), 3.9(b)	Fig. 3.7, left column. Notch signaling .	1	$r_J = 500\,; r_D = 1000\,.$ Well separated content of V between tip and stalk cells. Close to physiological angiogenesis.
3.9(c), 3.9(d)	Fig. 3.2, right column. Impaired adhesion of RPE - RPE . Fig. 3.7, middle column. Notch signaling .	2	$r_J = 2000\,; r_D = 1000\,.$ High proliferation of stalk cells for $J > J_{\text{tipmax}}\,.$ Pathological angiogenesis.
3.9(e), 3.9(f)	Fig. 3.7, right column. I Notch signaling .	2	$r_J = 2000\,; r_D = 7500\,.$ High proliferation of stalk cells for $J > J_{\text{tipmax}}\,.$ Pathological angiogenesis.

Table 3.5: **Summary of figures 3.8 & 3.9**

Figures	Correspond to	CNV	Potts adhesion parameters and characterization
3.10(a), 3.10(b)	Fig. 3.1, left column. Impaired adhesion of RPE - BM .	1	$\rho_{\text{adh}}^{\Sigma_\sigma,\Sigma_{\sigma'}}$(RPE - BM) $= 30$. Well separated content of V between tip and stalk cells. Close to physiological angiogenesis.
3.10(c), 3.10(d)	Fig. 3.1, middle column. Impaired adhesion of RPE - BM .	2	$\rho_{\text{adh}}^{\Sigma_\sigma,\Sigma_{\sigma'}}$(RPE - BM) $= 6$. High proliferation of stalk cells for $J > J_{\text{tipmax}}$. Pathological angiogenesis.
3.10(e), 3.10(f)	Fig. 3.1, right column. Impaired adhesion of RPE - BM .	2	$\rho_{\text{adh}}^{\Sigma_\sigma,\Sigma_{\sigma'}}$(RPE - BM) $= 0$. High proliferation of stalk cells for $J > J_{\text{tipmax}}$. Pathological angiogenesis.
3.11(a), 3.11(b)	Fig. 3.2, left column. Impaired adhesion of RPE - RPE & EC - EC .	2	$\rho_{\text{adh}}^{\Sigma_\sigma,\Sigma_{\sigma'}}$(EC-EC) $= 70$; $\rho_{\text{adh}}^{\Sigma_\sigma,\Sigma_{\sigma'}}$(RPE - RPE) $= 90$. High proliferation of stalk cells for $J > J_{\text{tipmax}}$. Pathological angiogenesis.
3.11(c), 3.11(d)	Fig. 3.2, middle column. Impaired adhesion of RPE - RPE & EC - EC .	1	$\rho_{\text{adh}}^{\Sigma_\sigma,\Sigma_{\sigma'}}$(EC-EC) $= 70$, $\rho_{\text{adh}}^{\Sigma_\sigma,\Sigma_{\sigma'}}$(RPE - RPE) $= 80$. Well separated content of V between tip and stalk cells. Close to physiological angiogenesis.
3.11(e), 3.11(f)	Fig. 3.2, right column. Impaired adhesion of RPE - RPE & EC - EC .	2	$\rho_{\text{adh}}^{\Sigma_\sigma,\Sigma_{\sigma'}}$(EC-EC) $= 80$, $\rho_{\text{adh}}^{\Sigma_\sigma,\Sigma_{\sigma'}}$(RPE - RPE) $= 80$. High proliferation of stalk cells for $J > J_{\text{tipmax}}$. Pathological angiogenesis.

Table 3.6: **Summary of figures 3.10 & 3.11**

3.3 Discussion

The mathematical model of angiogenesis in retina presented here illustrates the relative importance of mechanical, chemical and cellular cues to study AMD.

Given enough VEGF concentration in the choroidal space, CNV occurs and its type is affected by adhesion defects. Impaired adhesion between the basement membrane of the RPE and the BM allows the cells to move easily in this space. However, the sprouts may reach the subretinal space if the adhesion between RPE and the BM is strong. Our simulations also show that a reduced lateral adhesion between RPE cells facilitates type 2 CNV. Sprouts cross without difficulty the RPE layer and change from type 1 to type 2 CNV. Furthermore, we studied adhesion between ECs realizing that if it is weakened, the ECs are able to intersperse RPE cells and drusen to change quickly from type 1 to type 2 CNV.

One chief cause of CNV is a large VEGF gradients produced by high levels of VEGF at the sources. While a low level of VEGF at the walls of the choroid vessels does not activate ECs and start to develop a sprout, medium and high levels produce CNV and the levels difference affects the number of sprouts that are activated. The VEGF concentration is not only related to the cause of CNV, but also to its type. Under the same parameter values and conditions, the value of the VEGF gradient at the point where the sprout tries to cross the RPE determines the sprout chances of starting type 2 CNV. Higher VEGF concentration produces more active VEGF and greater number of VEGF receptors in tip cells so that the larger chemotactic force experienced by the leading ECs favors type 2 CNV over type 1 CNV.

Not only VEGF receptors and active VEGF of Notch signaling proteins determine CNV. A large Jagged production rate corresponds to pathological angiogenesis, which is the most similar scenario to type 2 CNV. Decreasing the Jagged production rate makes the blood vessels thicker and the number of hybrid cells behaving as tip cells is much lower so only type 1 CNV is observed. However, increasing Delta production rate with a high Jagged production rate does not prevent type 2 CNV in retina [125]. The resulting blood vessels are thinner and worse organized, but they are still able to cross the RPE layer. Finally, we can also distinguish type 1 CNV from type 2 CNV displaying the content of VEGF in the tip, stalk and hybrid tip-stalk cells, V , versus the external VEGF, $V_{\text{ext}} = C$, or versus the Jagged content J. Finding hybrid tip - stalk cells in a wide range of V_{ext} is a sign of type 2 CNV. On the other hand, the greater is the variance of Jagged in tip and hybrid tip - stalk cells, the greater the probability of having a type 2 CNV.

To allow for quantitative comparisons with experiments, our 2D model of angiogenesis in retina needs to be extended in several directions to be made more realistic and to predict better the evolution of wet AMD. The extension of the model to three dimensional configurations is straightforward although it requires more computing power. To move toward later stages of the formation of an advancing vascular plexus, we need to add lumen formation and blood circulation to the model. These processes will allow us to tackle the concurrent sprouting and anastomosis on the front of the advancing vascular plexus and the pruning of poorly perfused sprouts on its back.

Chapter 4

Models of lumen formation in sprouting angiogenesis

Lumen formation is an important feature to consider in mathematical and computational models of angiogenesis due to its biological implications. However, the work that has been done in this field is limited. In this chapter we present the two models of lumen formation we have developed.

The first one is inspired in the model of Boas and Merks for lumen formation [17] and described in section 1.2.4. In this model we start with a preformed sprout simulated with the model of chapter 2 and we assume that the mechanisms of cord and cell hollowing lumenize the sprout using cell repulsion and vacuolization. Boas and Merks consider that ECs are placed in rails where they can not escape when they are separating from each other to form the lumen [17]. This fact affects the results in our model, as we have to let the membrane of cells that are in contact to the ECM be fixed. Thus, the obtained results are not what we expected because we cannot use this model while the sprout is developing. Additionally, fixing the walls produces a lack of realism because it makes no sense using a CPM and not being able to allow fluctuations in membranes.

Due to the inconveniences of that model, we decided to develop a new one based on the experiments of Gebala *et al.* [16] explained in section 1.1. The blood pressure from the parent vessel exerts a force on the cell membrane that is taken into account in the CPM Hamiltonian. Cell polarization is simulated in this model by adding a new adhesion term in the Hamiltonian. This combination leads to the inverse blebbing described in their experiments. The preliminary results on developing a single sprout where the lumenization occurs are promising. We are still working on this model, overcoming its limitations and analyzing the results in more complex networks.

The chapter is divided into two main sections in which the two models are explained. The section 4.1 Cell and cord hollowing model contains the explanation of the mathematical model mentioned in the title as well as the results and discussion. In section 4.2 Inverse blebbing model the structure is similar: description of the mathematical model of inverse blebbing, presentation of the results and discussion.

4.1 Cell and cord hollowing model

4.1.1 Mathematical model

Cellular Potts model

Pixels $\mathbf{x}$ can belong to different type of compartments, $\tau(\sigma(\mathbf{x}))$, where $\sigma(\mathbf{x})$ is the ID of these compartments. Different objects of the same type $\tau(\sigma(\mathbf{x}))$ have different ID $\sigma(\mathbf{x})$ in order to distinguish them. In eq. (4.1.1), the value of $\tau(\sigma(\mathbf{x}))$ associated to each compartment is displayed.

$$\tau(\sigma(\mathbf{x})) = \begin{cases} 0, & \text{if } \mathbf{x} \text{ belongs to the ECM,} \\ 1, & \text{if } \mathbf{x} \text{ belongs to the luminal fluid,} \\ 2, & \text{if } \mathbf{x} \text{ belongs to the cytoplasm of a cell,} \\ 3, & \text{if } \mathbf{x} \text{ belongs to the apical membrane of a cell,} \\ 4, & \text{if } \mathbf{x} \text{ belongs to the basolateral membrane of a cell,} \\ 5, & \text{if } \mathbf{x} \text{ belongs to a vesicle,} \\ 6, & \text{if } \mathbf{x} \text{ belongs to a vacuole,} \end{cases} \tag{4.1.1}$$

Except for the ECM and the luminal fluid, the rest of the elements are part of a cell. The model also considers a label, $\xi(\sigma(\mathbf{x}))$, that identifies the cell to which the pixel $\mathbf{x}$ belongs. Thus, each pixel $\mathbf{x}$ has three labels: the type of the compartment $\tau(\sigma(\mathbf{x}))$, the ID of that compartment $\sigma(\mathbf{x})$ and the ID of the cell to which that compartment belongs $\xi(\sigma(\mathbf{x}))$, in case it is not ECM or luminal fluid [17]. The scheme of Fig. 4.1 may help to understand the labels $\sigma(\mathbf{x})$, $\tau(\sigma(\mathbf{x}))$ and $\xi(\sigma(\mathbf{x}))$.

For each pixel configuration, we define the Hamiltonian

$$\begin{aligned} H =& \lambda_{\text{area}}(\xi) \sum_{\xi} \left(A(\xi) - a(\xi)\right)^2 + \lambda_{\text{area}}(\sigma) \sum_{\sigma} \left(A(\sigma) - a(\sigma)\right)^2 + \\ & \sum_{(\mathbf{x},\mathbf{x}')} J_E\left(\tau(\sigma(\mathbf{x})), \tau(\sigma(\mathbf{x}'))\right)\left(1 - \delta\left(\xi(\sigma(\mathbf{x})), \xi(\sigma(\mathbf{x}'))\right)\right) + \\ & \sum_{(\mathbf{x},\mathbf{x}')} J_I\left(\tau(\sigma(\mathbf{x})), \tau(\sigma(\mathbf{x}'))\right)\left(1 - \delta\left(\sigma(\mathbf{x}), \sigma(\mathbf{x}')\right)\right)\delta\left(\xi(\sigma(\mathbf{x})), \xi(\sigma(\mathbf{x}'))\right) \end{aligned} \tag{4.1.2}$$

where the first two terms are the area constraints for cells, first summation, or for the compartments, second summation. A is the target area, a the actual area and λ the Potts parameters. The third and four terms represent the haptotaxis where two kind of adhesion are considered: internal, J_I, between elements of the same cell; and external, J_E, between elements of different cells [17]. The reference values of the parameters of eq. (4.1.2) can be found in Tables 4.1, 4.2 and 4.3. At each MCTS t, we select randomly a pixel $\mathbf{x}$, belonging to object $\tau(\sigma(\mathbf{x}))$, and propose to copy its spin $\sigma(\mathbf{x})$ to a neighboring

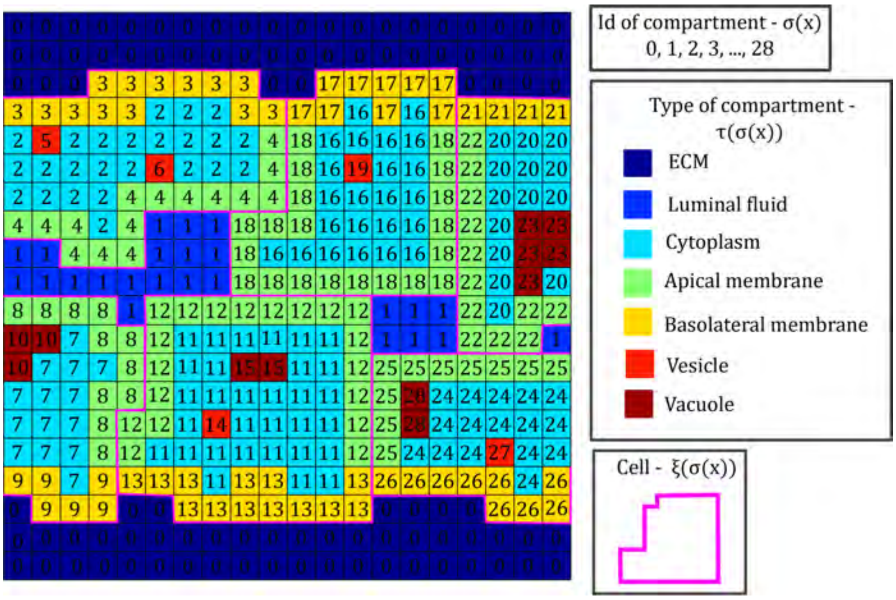

0	0	0	0	0	0	0	0	0	0	0	0	0	0	0	0	0	0	0	0
0	0	0	0	0	0	0	0	0	0	0	0	0	0	0	0	0	0	0	0
0	0	0	3	3	3	3	3	3	0	0	17	17	17	17	17	0	0	0	0
3	3	3	3	3	2	2	2	3	3	17	17	16	17	16	17	21	21	21	21
2	5	2	2	2	2	2	2	2	4	18	16	16	16	16	18	22	20	20	20
2	2	2	2	2	6	2	2	2	4	18	16	19	16	16	18	22	20	20	20
2	2	2	2	4	4	4	4	4	4	18	16	16	16	16	18	22	20	20	20
4	4	4	2	4	1	1	1	18	18	18	16	16	16	16	18	22	20	23	23
1	1	4	4	4	1	1	1	18	16	16	16	16	16	16	18	22	20	23	23
1	1	1	1	1	1	1	1	18	18	18	18	18	18	18	18	22	20	23	20
8	8	8	8	1	12	12	12	12	12	12	12	12	1	1	1	22	20	22	22
10	10	7	8	8	12	11	11	11	11	11	11	12	1	1	1	22	22	22	1
10	7	7	7	8	12	11	11	15	15	11	11	12	25	25	25	25	25	25	25
7	7	7	8	8	12	11	11	11	11	11	11	12	25	28	24	24	24	24	24
7	7	7	8	12	12	11	14	11	11	11	11	12	25	28	24	24	24	24	24
7	7	7	8	12	11	11	11	11	11	11	11	12	25	24	24	24	27	24	24
9	9	7	9	13	13	13	11	13	13	11	11	13	26	26	26	26	26	24	26
0	9	9	9	0	0	13	13	13	13	13	13	13	0	0	0	0	26	26	26
0	0	0	0	0	0	0	0	0	0	0	0	0	0	0	0	0	0	0	0
0	0	0	0	0	0	0	0	0	0	0	0	0	0	0	0	0	0	0	0

Figure 4.1: **Example of a simplified domain for the CPM of the cell and cord hollowing model.** $\sigma(\mathbf{x})$ denotes the label of the compartment occupying pixel $\mathbf{x}$. Type of compartments, $\tau(\sigma(\mathbf{x}))$, are listed in eq.(4.1.1). $\xi(\sigma(\mathbf{x}))$ identifies the cell to which the compartment belongs.

(target) pixel $\mathbf{x}'$ if $\sigma(\mathbf{x}) \neq \sigma(\mathbf{x}')$. The proposed copy in the spin configuration (spin flip) changes the configuration energy by an amount $\triangle H|_{\sigma(\mathbf{x}) \to \sigma(\mathbf{x}')}$, and it is accepted with probability $P\left(\sigma(\mathbf{x}) \to \sigma(\mathbf{x}')\right)(t) = \{e^{-\Delta H|_{\sigma(\mathbf{x}) \to \sigma(\mathbf{x}')}/T}, \Delta H > 0; 1, \Delta H \leq 0\}$ (Metropolis algorithm) [88]. An appropriate temperature for our simulations is $T = 50$.

Included mechanisms for cell polarization and vacuolization

Cell surface polarization. The polarization of cell membranes is checked every two MCTS. A pixel belongs to the basolateral membrane if among its neighbors there are ECM pixels, and to the apical membrane otherwise.

Table 4.1: **Reference values of external contact energy** J_E [17]

	Cytoplasm	**Basolateral**	**Apical**	**Vesicle**	**Vacuole**	**ECM**	**Luminal fluid**
Cytoplasm	10						
Basolateral	10	30					
Apical	200	50	200				
Vesicle	10	10	10	10			
Vacuole	10	10	10	10	10		
ECM	130	10	10	10	10	10	
Luminal fluid	10	200	50	10	10	130	0

Table 4.2: **Reference values of external contact energy** J_I [17]

	Cytoplasm	**Basolateral**	**Apical**	**Vesicle**	**Vacuole**	**ECM**	**Luminal fluid**
Cytoplasm	10	5	5	10	20	-	-
Basolateral		10	70	100	100	-	-
Apical			10	1	1	-	-
Vesicle				10	5	-	-
Vacuole					5	-	-
ECM						-	-
Luminal fluid							-

Table 4.3: **Reference values of λ and target areas.** Target areas not included in the table are equal to the actual area of the elements.

$\lambda_{\textbf{cell}}$	$\lambda_{\textbf{fluids}}$	$\lambda_{\textbf{vacuole}}$	$\lambda_{\textbf{vesicle}}$	$\mathbf{A}_{\textbf{cell}}$	$\mathbf{A}_{\textbf{vesicle}}$
7	6	50	1000	78.42 μm^2	0.13 μm^2

Pinocytosis. Pinocytosis is a process in which material from ECM is brought into the cell through an invagination of the cell membrane. In our model, pixels belonging to the cell membrane that, through copies of the CPM, get surrounded by cytoplasm, vesicles or vacuoles become vesicles with a probability $P_{\text{pin}} = 1$. This condition is checked every two MCTS.

Swapping of vesicles. The target area of vesicles is one pixel, so their movement is not produced by copies of the CPM. Instead, the information of the two neighboring pixels is exchanged with probability $P_{\text{A}} = 1$ times the Boltzmann probability described above.

Fusion of vesicles and vacuoles. If a suggested copy during CPM is between two vesicles, two vacuoles of a vesicle and a vacuole, these two elements are merged into a single element with probability $P_{\text{fuse}} = 1$. The target area of the new vacuole is the sum of the target areas of the two merged elements.

Transition of isolated vacuole pixels to vesicles. Vacuoles are created by merging vesicles or other vacuoles, but when a vacuole has an area of one pixel, it turns into a vesicle. If a vacuole splits in two, the resulting parts could be vacuoles if the area is greater than one pixel o vesicles. The actual area of each part is checked again and the target area is the actual area after splitting.

Secretion. If a vesicle is in contact with the cell membrane or the luminal fluid, it becomes luminal fluid. In case of vacuoles, the part of them that is in contact with the cell membrane or the luminal fluid becomes luminal fluid. In successive MCTS, the whole vacuole is secreted. The actual area of the resulting cell needs to be modify by subtracting the area of the vesicle, vacuole or part of a vacuole.

Onset of lumen formation

Two possibilities to carry out simulations have been considered: try the model in an already developed sprout or applying this model while the sprout is developing to cells far from the tip cell. The first option was the chosen one and the second option would be develop if the results of the first one were good.

Figure 4.2 shows the initial configuration of the simulation in this model. It consist in a square domain with a simple sprout without branching that has grown from left to right, as we can see for the tip cell in pink. The data of this initial configuration is loaded in the simulation code and the pixels of the cells are classified in cytoplasm, apical membrane and basolateral membrane.

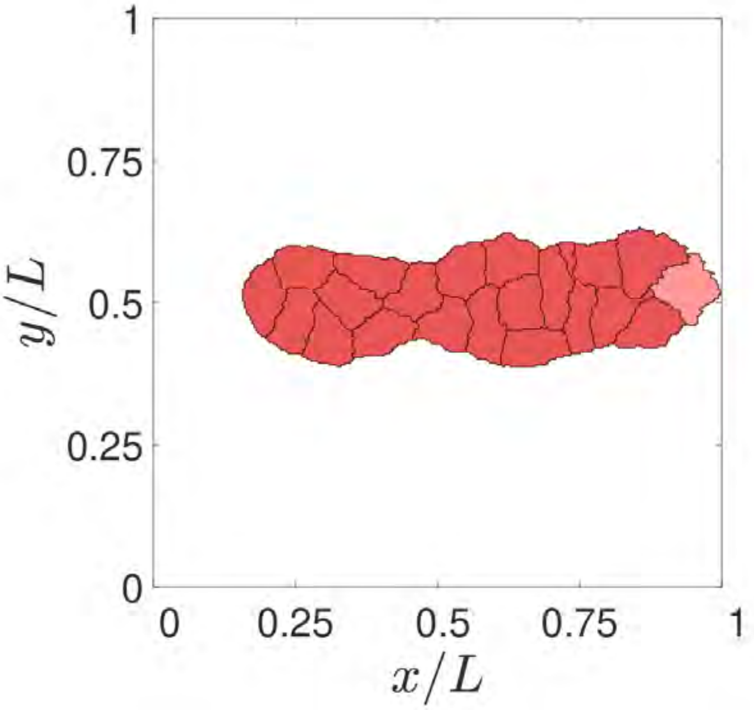

Figure 4.2: **Initial configuration of lumen formation simulations.** Tip cell is pink.

4.1.2 Results and discussion

The simulations of the model described in section 4.1 with the defined initial configuration of Fig. 4.2 exhibit some problems, as shown in Fig. 4.3. All figures in this section are snapshots at MCTS 1, 61, 131, 181, 241, 401; from top left to bottom right. Colorbars represent the type of the objects, defined in eq. (4.1.1).

ECs separate instead of elongate and form the lumen. This event produces an invasion of the ECM into the luminal fluid and the reduction of the ECs size due to the adhesion parameters. The difference in the results is caused by the missing rails in our simulations. Before setting these rails, some solutions are analyzed.

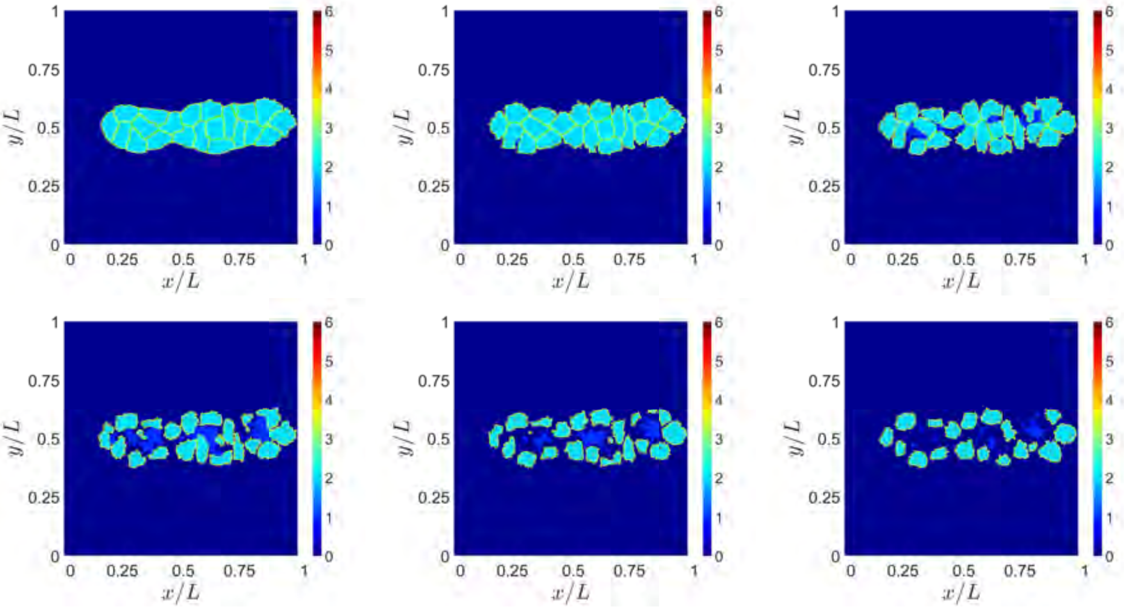

Figure 4.3: **Lumen formation using the model described in section 4.1.**

The first one is changing the external adhesion parameter J_E between ECM and the apical membrane. Although it is true the apical membrane is the one that is not in contact with the ECM, due to the frequency with which the cells are polarized in the model, it may occur during certain MCTS. Thus, increasing ten times the value of J_E(ECM, Apical) makes this contact more costly in terms of energy of the system. In

Fig. 4.4 we can see the result of setting J_E(ECM, Apical) $= 100$. In this case, ECs stay together longer, but when the ECM penetrates between them, their size is significantly reduced due to the adhesion parameters.

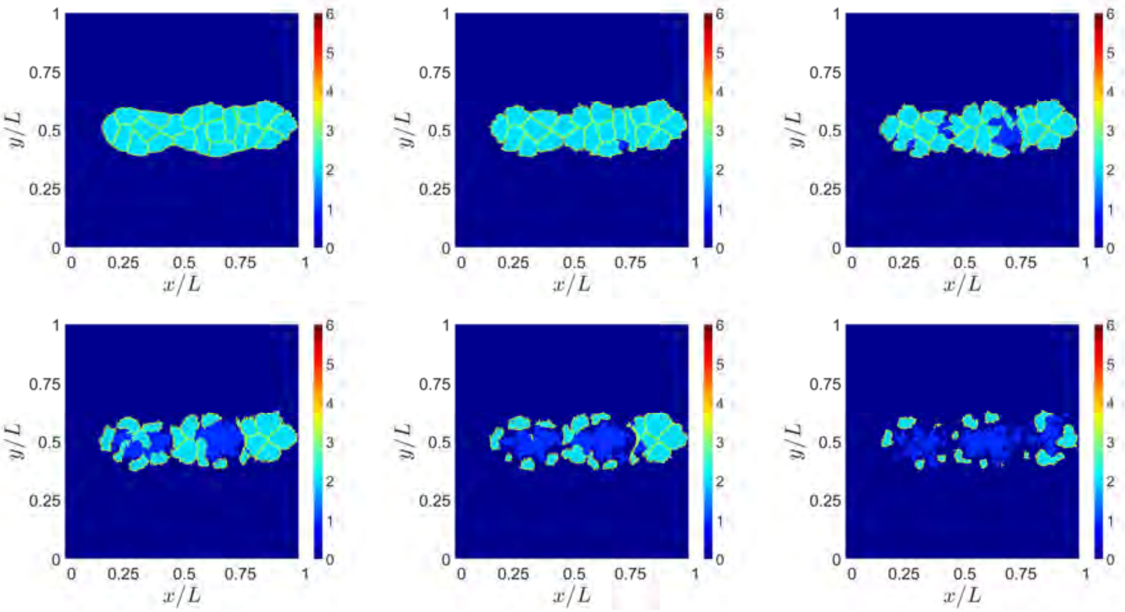

Figure 4.4: **Lumen formation using the model described in section 4.1, but** J_E**(ECM, Apical)** $= 100$**.**

In order to maintain the size of the ECs near the target area, the Potts parameter of the area of ECs has been increased to $\lambda_{\text{cell}} = 500$ in Fig. 4.5. However, basically there is no difference between Figs. 4.4 and 4.5.

The first two modifications can not solve the problem of cell separation. We suggest a different approaching of the problem after setting the values of the modified parameters to the original values presented in tables 4.1, 4.2 and 4.3. If the ECM can not copy the ID of its pixels over the basolateral membrane, the ECs do not separate from each other. This mechanism has been implemented on the simulation of Fig. 4.6.

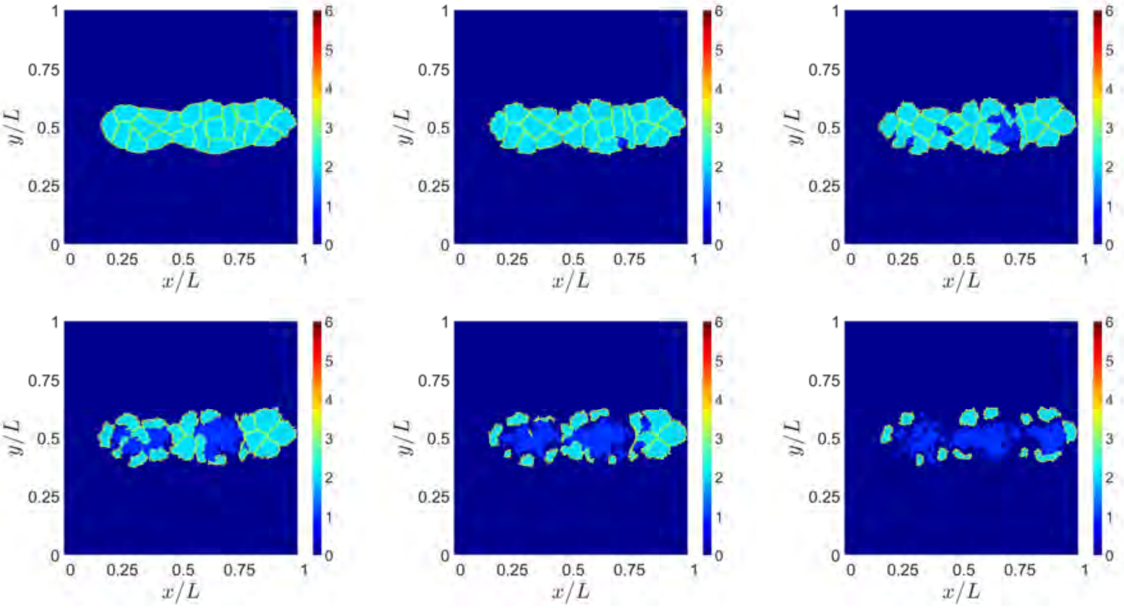

Figure 4.5: **Lumen formation using the model described in section 4.1, but** J_E**(ECM, Apical)** $= 100$ **and** $\lambda_{\text{cell}} = 500$**.**

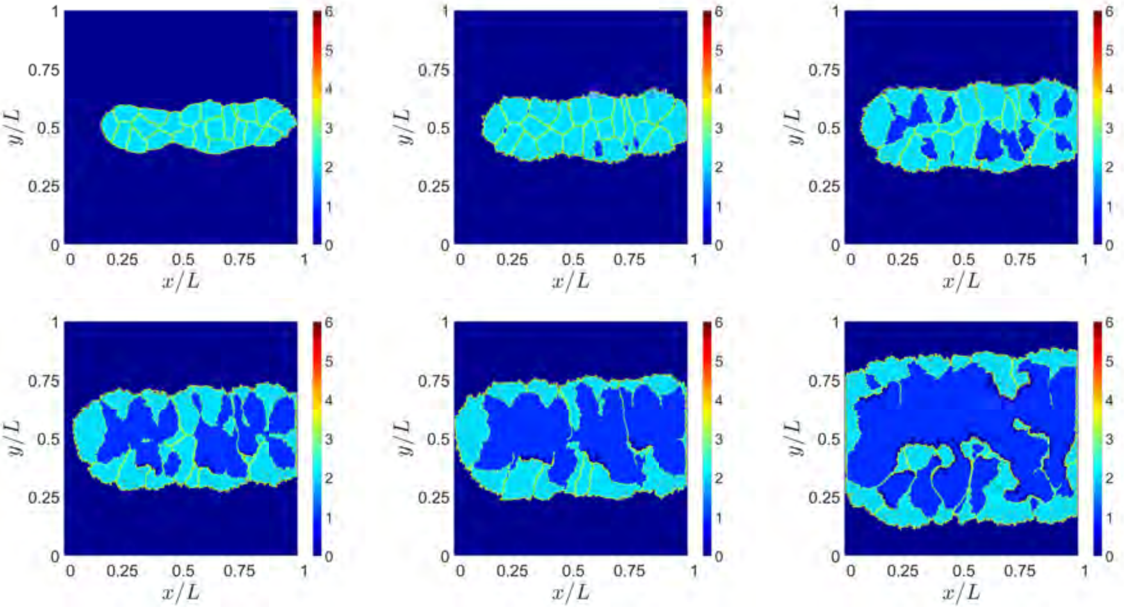

Figure 4.6: **Lumen formation using the model described in section 4.1, but copies from ECM over basolateral membranes are not accepted.**

On the other hand, the ECs and the luminal fluid spread across the domain. The final snapshot of Fig. 4.6 is closer to the idea of lumen formation, but the area of the luminal fluid and the ECs need to be closer to the target values. Fig. 4.7 displays a simulation with the same mechanism as Fig. 4.6 but $\lambda_{\text{cell}} = 500$ and $\lambda_{\text{fluids}} = 4000$.

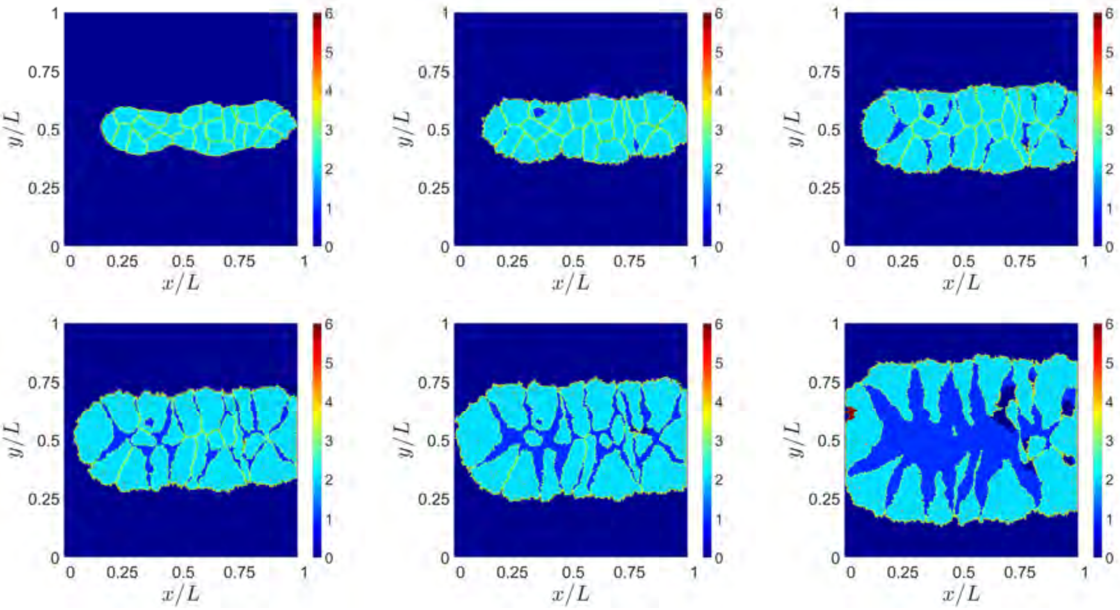

Figure 4.7: **Lumen formation using the model described in section 4.1, but copies from ECM or luminal fluid over basolateral membranes are not accepted, $\lambda_{\text{cell}} = 500$ and $\lambda_{\text{fluids}} = 4000$.**

The changes in the Potts parameters to control the area of ECs and luminal fluid do not avoid the sprout to expand, although the ECs have similar area between them in Fig. 4.7. Finally, we decided to maintain fixed the basolateral membrane of every cell. Thus, MC attempts involving pixels belonging to a basolateral membrane are discarded. The result is shown in Fig. 4.8. In this last simulation, ECs do not separated from each other and narrow for forming the lumen. Even tough the lumenization is finally produced, fixing the basolateral membranes makes the implementation of lumen formation during the sprouting unrealistic. Furthermore, one of the characteristics of the CPM that is the fluctuations of cell membranes is now discarded.

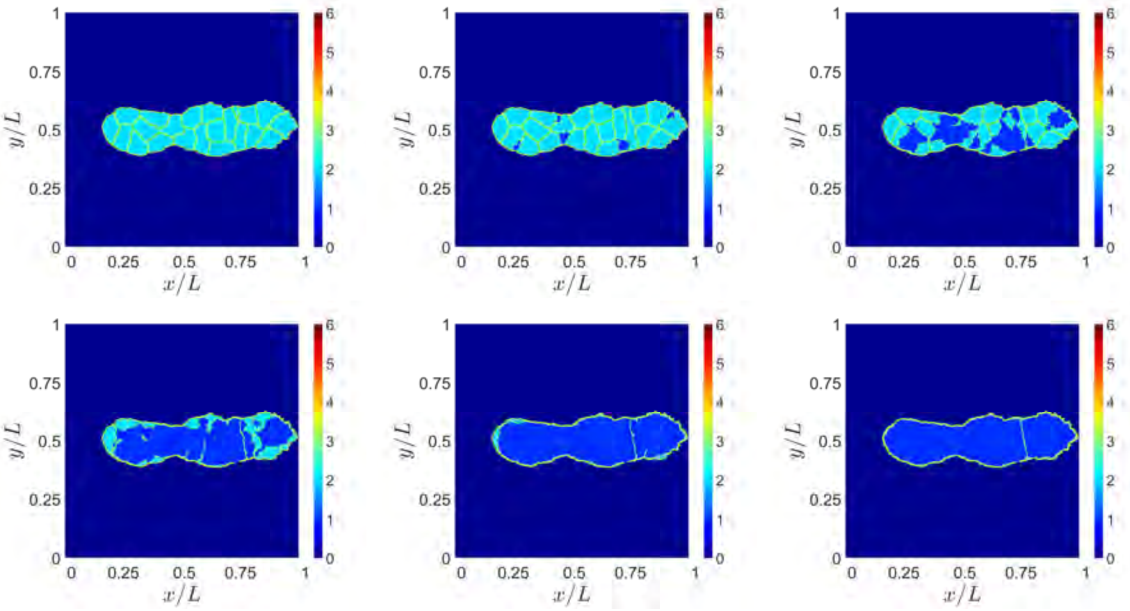

Figure 4.8: **Lumen formation using the model described in section 4.1, but copies that involve ECM are not accepted.**

4.2 Inverse blebbing model

The model of lumen formation by inverse blebbing is based on the model of chapter 2 with the incorporation of new elements for the lumenization process [125]. A CPM includes haptotaxis, durotaxis, chemotaxis and constraints for area, perimeter and length of ECs is in charge of moving ECs and change their size. Meanwhile the unsupervised K-means algorithm is used to implement proliferation of ECs. Notch signaling pathway is incorporated to the model and it decides the phenotype of the cells of the sprout. However, only one sprout is considered without branching nor anastomosis in order to simplify at this point of model development. During the evolution of the sprout, the formation of the lumen is included through two extra terms in the hamiltonian. One of them favors the movement of ECs in the direction of some forces. These forces represent the pressure of the blood from the parent vessel and the mentioned unsupervised K-means algorithm is used again to set the forces. Since it is a 2D model and we consider the cross section of the vessel, ECs will be separated in two sides after the lumen formation. ECs except the tip cell are previously classified in one of these sides to add cell polarization in the other extra term of the hamiltonian for the adhesion between sides.

Signaling processes and continuum fields at the extracellular scale such as VEGF concentration and strains are considered in exactly the same way as in Chapter 2 [125]. In order to avoid repetitions, the detail of these parts may be review in the mentioned chapter.

4.2.1 Mathematical model

Cellular Potts model

Square grid. We consider a square domain Ω of side $L = 0.23$ mm with the grid points as defined in section 2.1 [125]. The domain size is slightly smaller than the one in in section 2.1, but the number of pixels $(M-1)^2$ has changed in order to make their size smaller and gain accuracy.

Objects, spins and Metropolis algorithm. Pixels $\mathbf{x}$ can belong to different type of objects Σ_σ, namely ECs and ECM. The field (called spin in a Potts model) $\sigma(\mathbf{x})$ denotes the label of the object occupying pixel $\mathbf{x}$ [88], 0 for ECM and greater than 0 for ECs. The side in the sprout of the object $\sigma(\mathbf{x})$ is denoted by the field φ_σ. Each given spin configuration for all the pixels in the domain has an associated energy $H(\{\sigma(\mathbf{x})\})$ to be specified below. At MCTS t, we select randomly a pixel $\mathbf{x}$, belonging to object $\sigma(\mathbf{x})$, and propose to copy its spin $\sigma(\mathbf{x})$ to a neighboring (target) pixel $\mathbf{x}'$ that $\sigma(\mathbf{x}') \neq \sigma(\mathbf{x})$. The proposed change in the spin configuration (spin flip) changes the configuration energy by an amount $\triangle H|_{\sigma(\mathbf{x})\to\sigma(\mathbf{x}')}$, and it is accepted with probability (Metropolis algorithm) [88, 125]

$$P\left(\sigma(\mathbf{x}) \to \sigma(\mathbf{x}')\right)(t) = \begin{cases} e^{-\Delta H|_{\sigma(\mathbf{x})\to\sigma(\mathbf{x}')}/T}, & \Delta H|_{\sigma(\mathbf{x})\to\sigma(\mathbf{x}')} > 0; \\ 1, & \Delta H|_{\sigma(\mathbf{x})\to\sigma(\mathbf{x}')} \leq 0. \end{cases} \tag{4.2.1}$$

The temperature $T > 0$ is measured in units of energy and it is related to an overall system motility. We have selected $T = 4$ in our simulations.

Energy functional. The energy functional H is

$$\begin{aligned} H \;=\; & \sum_{\sigma} \rho_{\text{area}} \left(\frac{a_\sigma - A_\sigma}{A_\sigma}\right)^2 + \sum_{\sigma} \rho_{\text{perimeter}} \left(\frac{p_\sigma - P_\sigma}{P_\sigma}\right)^2 + \sum_{\sigma} \rho_{\text{length}} \left(\frac{l_\sigma - L_\sigma}{L_\sigma}\right)^2 \\ & + \sum_{\mathbf{x},\mathbf{x}'} \rho_{\text{adh}}^{\Sigma_\sigma,\Sigma_{\sigma'}} \left(1 - \delta_{\sigma,\sigma'}\right) + \sum_{\mathbf{x},\mathbf{x}'} \rho_{\text{sid}}^{\varphi_\sigma,\varphi_{\sigma'}} \left(1 - \delta_{\sigma,\sigma'}\right) \\ & + H_{\text{durot}} + H_{\text{chem}} + H_{\text{lumen}}. \end{aligned} \tag{4.2.2}$$

where the three first terms are sums over cells that impel them to reach target areas, perimeters and lengths with strengths given by their Potts parameters ρ_j. The fourth term (haptotaxis) sums over all pixels and accounts for adhesion between elements. It is zero for pixels belonging to the same cell and calibrates the repulsion between pixels belonging to different cells (adhesion is stronger for smaller repulsion), depending on the value of the corresponding Potts parameter $\rho_{\text{adh}}^{\Sigma_\sigma,\Sigma_{\sigma'}}$.

The fifth term sums over all pixels and accounts for adhesion between the sides of the sprout. Although the tip cell does not belong to any side, the adhesion between the tip cell and the two sides is also considered as well as the adhesion between sides.

The sixth and seventh terms correspond to durotaxis and chemotaxis, impelling cells to move toward gradients of stiffness and VEGF concentration, respectively [125].

The eighth term represents the movement of ECs due to blood pressure. The net variation of the lumenization term H_{lumen} is

$$\Delta H_{\text{lumen}} \;=\; -\rho_{\text{lumen}} \cos(\theta_{\mathbf{v}_f,\mathbf{v}_m}) \left(\mathbf{v}_f \cdot \mathbf{v}_m\right)^2, \tag{4.2.3}$$

where ρ_{lumen} is a Potts parameter, $\mathbf{v}_m = (\mathbf{x}' - \mathbf{x})/\left|\mathbf{x}' - \mathbf{x}\right|$ and $\mathbf{v}_f = \mathbf{U}(\mathbf{x})/\left|\mathbf{U}(\mathbf{x})\right|$ is the vector of the force exerted by the blood, $\mathbf{U}(\mathbf{x})$, with $\mathbf{x}$ the target pixel for retractions and the source pixel for extensions. $\theta_{\mathbf{v}_f,\mathbf{v}_m}$ is the angle between vectors $\mathbf{v}_m$ and $\mathbf{v}_f$.

Detailed expressions for these terms except the fifth and eighth are given in section 2.1.

The values of the Potts parameters are listed in Tables 4.4 and 4.5. They are chosen according to those defined in section 2.1 and the reference [125], but allowing more fluctuations in perimeter and length of ECs. Additionally, adhesion terms become more important.

Table 4.4: **Dimensionless Potts parameters.** Area, perimeter and length constraints, durotaxis, chemotaxis and lumen.

Param.	ρ_{area}	$\rho_{\text{perimeter}}$	ρ_{length}	ρ_{durot}	ρ_{chem}^0	ρ_{lumen}
Value	4500	75	3.6	20	200000	500

Table 4.5: **Dimensionless Potts parameters.** Adhesion.

Param.	$\rho_{\text{adh}}^{\Sigma_\sigma,\Sigma_{\sigma'}}$ (EC - EC)	$\rho_{\text{adh}}^{\Sigma_\sigma,\Sigma_{\sigma'}}$ (EC-ECM)	$\rho_{\text{sid}}^{\varphi_\sigma,\varphi_{\sigma'}}$(different sides)	$\rho_{\text{sid}}^{\varphi_\sigma,\varphi_{\sigma'}}$ (side - tip cell)
Value	55.2	27.6	69	44.16

Definition of forces related to blood pressure

ECs of the sprout except for the tip cell are classified in the two sides. Thus, for each side $i = 1, 2$, let $\mathbf{v}_s^i$ be a vector that contains the ID of the pixels in the side i that have boundary with the pixels in the side j with $j \neq i$. The unsupervised machine learning algorithm *K-means clustering* is used to associate each pixel of the side $i = 1, 2$ to one of the elements of the vector $\mathbf{v}_s^j$ with $j \neq i$. Thereby, the elements of the vector $\mathbf{v}_s^j$ function as the centroids of the K clusters with K the length of $\mathbf{v}_s^j$ and the pixels are assigned prioritizing the criterion of the distance but with spatial sense.

Let $\mathcal{C}^{\mathbf{x}}$ be the centroid of the cluster that $\mathbf{x}$ belongs. Let $\mathbf{x}^{\text{tip}}$ be the pixel of the tip cell closest to the hypoxic area. Let $d_{\mathbf{x},\mathcal{C}^{\mathbf{x}}} = \sqrt{(\mathcal{C}^{\mathbf{x}}{}_x - \mathbf{x}_x)^2 + (\mathcal{C}^{\mathbf{x}}{}_y - \mathbf{x}_y)^2}$ be the distance between $\mathbf{x}$ and $\mathcal{C}^{\mathbf{x}}$. The force applied to the pixel $\mathbf{x}$ by the blood is

$$\begin{aligned}\mathbf{U}(\mathbf{x}) = \Bigg[& U_0 \exp\left(-\left(\frac{(\mathcal{C}^{\mathbf{x}}{}_x - \mathbf{x}_x)^2}{\nu_l} + \frac{(\mathcal{C}^{\mathbf{x}}{}_y - \mathbf{x}_y)^2}{\nu_l}\right)\right) \\ & - U_1 \left(d_{\mathbf{x},\mathcal{C}^{\mathbf{x}}} - r_l\right)^2 H(d_{\mathbf{x},\mathcal{C}^{\mathbf{x}}} - r_l)\Bigg] \omega(\mathbf{x}, \mathbf{x}^{\text{tip}})\, \mathbf{D_l}\left(\mathbf{x},\, \mathcal{C}^{\mathbf{x}}\right)\end{aligned} \tag{4.2.4}$$

where $U_0 = 6250000$, $U_1 = 40000$, $\nu_l = 1$, $r_l = 5$ and H the Heaviside function. The weight function $\omega(\mathbf{x}, \mathbf{x}^{\text{tip}})$ is

$$\omega(\mathbf{x}, \mathbf{x}^{\text{tip}}) = \frac{\left(\mathbf{x}_x^{\text{tip}} - \mathbf{x}_x\right)^2 + \left(\mathbf{x}_y^{\text{tip}} - \mathbf{x}_y\right)^2}{(\mathbf{x}_x^{\text{tip}})^2}$$

And the direction of the force U is given by $\mathbf{D_l}\left(\mathbf{x},\, \mathcal{C}^{\mathbf{x}}\right)$

$$\mathbf{D_l}\left(\mathbf{x},\, \mathcal{C}^{\mathbf{x}}\right) = \left(\frac{\mathbf{x}_x - \mathcal{C}^{\mathbf{x}}{}_x}{d_{\mathbf{x},\mathcal{C}^{\mathbf{x}}}}, \frac{\mathbf{x}_y - \mathcal{C}^{\mathbf{x}}{}_y}{d_{\mathbf{x},\mathcal{C}^{\mathbf{x}}}}\right)$$

$\mathbf{U}$ may change every MCTS due to the copies of the CPM. Therefore, at MCTS t the force at pixel $\mathbf{x}$ is updated with the average of $\mathbf{U}(\mathbf{x})$ and the value of this force in $\mathbf{x}$ in the previous MCTS, $t-1$, if that is different from zero.

Every MCTS, $\mathbf{U}$ is updated only in the pixels belonging to ECs of the sides. We maintain the defined forces in pixels of the ECM which belonged to some ECs before. The forces in pixels of the tip cell are set at zero.

Proliferation

Cell splitting and proliferation is implemented as it is described in section 2.1. However, in this model one cell per side is able to proliferate. At the beginning of the simulation, the tip is the unique cell and it doubles its size and proliferates. One of the resulting cells maintains the tip phenotype and the other is assigned to one of the sides. The cell assigned to one of the sides is a proliferating cell. Once it splits in two, one cell maintain the same side and the other is assigned to the other side. At this point of the simulation, there are three ECs: a tip cell and one proliferating cell per side. From this moment, the cells resulting from the splitting stay in the same side to elongate each side and therefore the sprout.

4.2.2 Results and discussion

The preliminary results show the initial formation of the lumen in the sprout by inverse blebbing. A detailed description of the simulation code can be found in Chapter 5. In figures 4.9 and 4.10, the black arrows represent the force vectors related to blood pressure, tip cell is pink and cells of each side have different colors, light or dark red, and the contour lines represent the VEGF concentration, C. An initial stage of a simulation is shown in Fig. 4.9. The direction of the force vectors is adequate to start the lumen formation and their modules are higher further from the tip cell to favor the lumenization at this point.

Figure 4.10 displays snapshots of a simulation of the inverse blebbing model. The endothelial cells of the sprout adapt their shape and form the lumen while the sprout is developing. Inverse blebs appear in Fig. 4.10 (f) and the lumen formation almost reaches the tip cell.

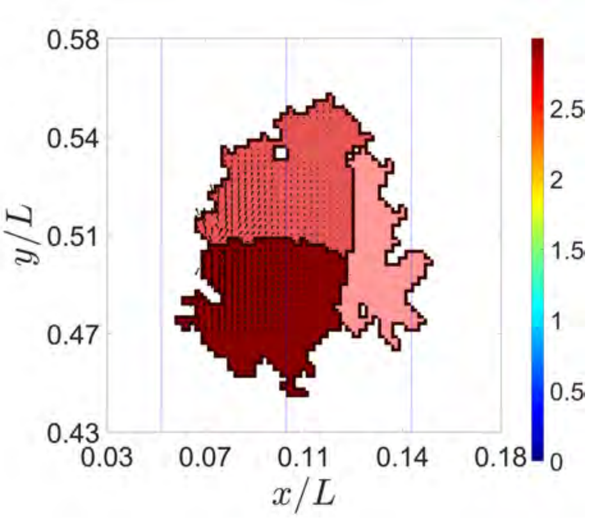

Figure 4.9: **Example of initial stage of the simulation with only three cells: the tip cell and one cell per side.**

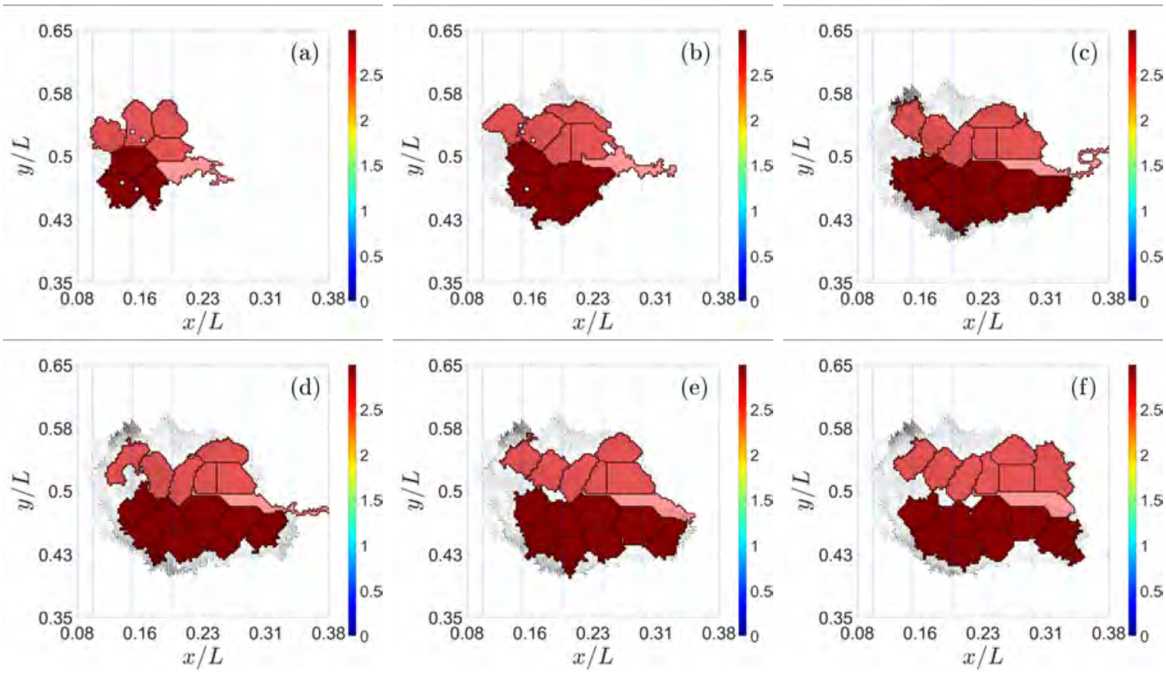

Figure 4.10: **Lumen formation using the inverse blebbing model.** Times in MCTS are: (a) 301, (b) 1181, (c) 2001, (d) 2401, (e) 3001, (f) 3381.

Chapter 5

GPU-based parallel implementation of cellular dynamics models of angiogenesis

The models of chapters 2, 3 and 4 have been implemented on Graphics Processing Unit (GPU) using C-CUDA (CUDA: Compute Unified Device Architecture created by NVIDIA Corporation), and some parts of our code contain proprietary NVIDIA corporation source code. The visualization is performed using Matlab's graphics functions.

Our simulation code of chapter 2, which we refer to as AngioVCTB, is inspired by the simulation code due to van Oers *et al.* [92](implemented in C), and it uses the K-means CUDA algorithm [133] and some CUDA libraries that will be specified later.

The simulation codes for chapters 3 and 4 are based on the previous one [125].

5.1 AngioVCTB

Here, we describe a novel parallel computing implementation of the model that uses C-CUDA to reduce the computational times as much as possible. The number of processes that can be calculated at the same time over pixels, cells or vessels using kernels (function that runs on the GPU) make this problem manageable. Furthermore, the implementation of our own code allow us to control times, features, parallel processes and the addition or changes of modules. Fig. 5.1 shows a flow diagram of our simulation code. Each part of the flow diagram will be described in detail afterwards.

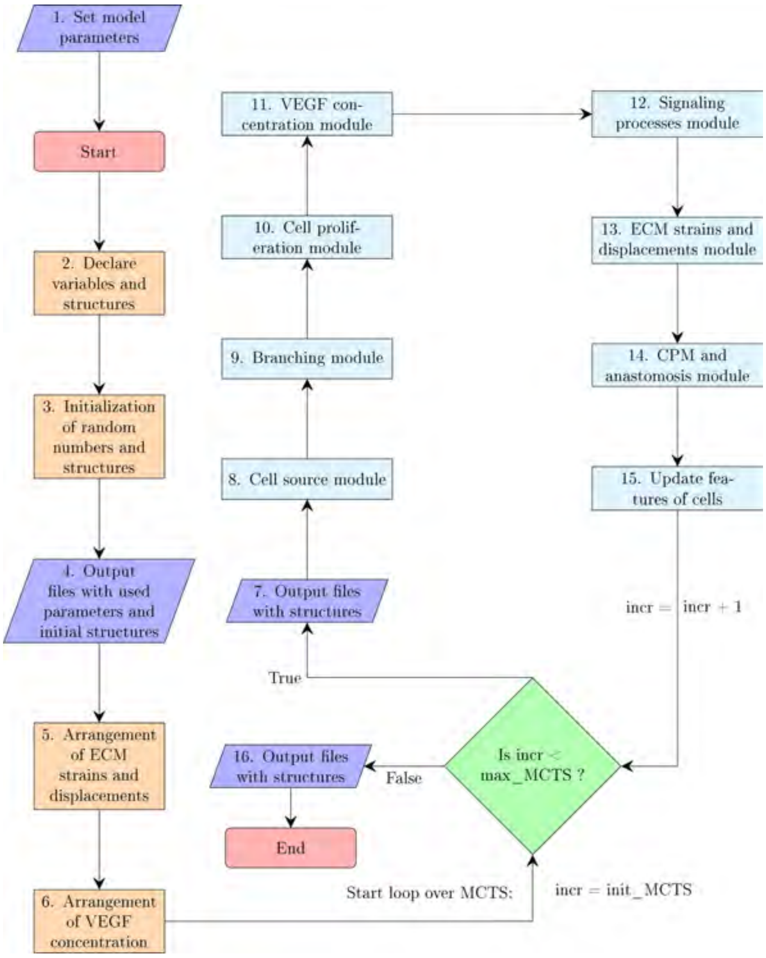

Figure 5.1: **Flow diagram of the simulation code of the AngioVCTB model [125]**

5.1.1 Modules 1. & 2. Set model parameters & Declare variables and structures

This simulation code consists of the following source (.cpp, .cu, .cc) and header (.h, .cuh) files:

- `def.h` defines model parameter values.
- `struct.h` defines structures used in the code.
- `functions.h` declares all the functions used in the code executed in Central Processing Unit (CPU) (and shows in which .cpp, .cu or .cc file are defined).
- `functions_CUDA.cuh` declares all the functions used in the code executed in GPU (and shows in which .cpp, .cu or .cc file are defined).
- `cpmfem.cpp` contains the main() function, which calls all other functions of the model.
- `init.cpp` initializes pixels, nodes, cells and vessels structures at zero.
- `init.cu` sets the initial distribution of cells in pixels, nodes, cells and vessels structures, impose external forces and constrains. This file also contains functions that copy from CPU to GPU or vice versa and then call functions in write.cpp to save output.
- `read.cpp` loads input, for instance cell positions.
- `write.cpp` saves output, such as cell positions and strains.
- `cellmoves.cu` cellular Potts movement and anastomosis.
- `cellforces.cu` calculates cell traction forces.
- `FE_local.cpp` defines element stiffness matrices (and using them to calculate stresses and strains).

- `FE_assembly.cpp` assembles element stiffness matrices into global stiffness matrix.
- `FE_nodes2dofs.cu` some bookkeeping between the set of elasticity equations and nodal forces and displacements.
- `branching.cu` performs the branching of blood vessels.
- `chemotaxis.cu` contains the Preconditioned Conjugate Gradient (PCG) method. This file calculates the VEGF concentration.
- `notchsignaling.cu` calculates number of proteins related to the signaling processes for each cell.
- `proliferation.cu` splits in two the cells that meet some conditions.
- `fp_abstraction.h, kmcuda.cc, kmcuda.h, metric_abstraction.h, private.h, traspose.cu, tricks.cuh, wrappers.h` are files related to K-means algorithm.
- `mt.cpp` contains the Mersenne twister algorithm for generation of pseudorandom numbers.

Considering the domain and the computational requirements of of AngioVTCB, we use the C-structures and arrays described below:

- VOX: structure with data related to pixels. Arrays contain $(M-1)^2$ elements, where M is the number of nodes on a side of the square domain.
  - .ctag: (int array) ID of occupying cell, 0 if no cell.
  - .vtag: (int array) ID of occupying vessel, 0 if no vessel.
- NOD: structure with data related to nodes. Arrays contain M^2 elements.
  - .fx, .fy: (float arrays) x and y component of the force that it is exerted by cells in this node.
  - .ux, .uy: (float arrays) x and y component of the displacement that it is suffered by this node.

  - .restrictx, restricty: (boolean arrays) 1 if there is a nodal restrictions in x or y direction, 0 otherwise.

- CEL: structure with data related to cells. Arrays contain a maximum of $10\cdot(M-1)$ elements, but it is only filled with non-zero values up to the number of cells at that moment.
  - .siz: (int array) cell's size (in pixels).
  - .peri: (int array) cell's perimeter (in pixels).
  - .tip: (int array) position in the grid of the cell's pixel that is closer to the hypoxic area.
  - .tail: (int array) position in the grid of the cell's pixel that is further to the hypoxic area.
  - .vegf: (float array) concentration of VEGF associated to the cell (measured in bottom left grid point of the pixel selected in .tip).
  - .pos: (int array) cell's phenotype. 1 if it is a tip cell, 2 if it is a proliferating stalk cell and 3 if it is a non-proliferating stalk cell.
  - .tshybrid: (boolean array) 1 if the cell has hybrid phenotype, 0 otherwise.
  - .age: (int array) cell's age (in MCTS).
  - .vess: (int array) ID of the vessel that the cell belongs.

- NDJ: structure with the amount of cells proteins of signaling processes. Arrays contain a maximum of $10 \cdot (M-1)$ elements, but it is only filled with non-zero values up to the number of cells at that moment.
  - .N: (float array) amount of Notch in the cell.
  - .D: (float array) amount of Delta in the cell.
  - .J: (float array) amount of Jagged in the cell.
  - .I: (float array) amount of NICD in the cell.

  - .Vr: (float array) amount of VEGFR2 in the cell.
  - .V: (float array) amount of active VEGF in the cell.

- VES: structure with data related to vessels. Arrays contain a maximum of $M-1$ elements, but it is only filled with non-zero values up to the number of vessels at that moment.
  - .tiptag: (int array) ID of the tip cell of the vessel.
  - .tipvox: (int array) ID of the pixel stored on .tip (CEL) of the tip cell.
  - .proltag: (int array) ID of proliferating stalk cell of the vessel.
  - .birth: (int array) MCTS when vessel was born.
  - .death: (int array) MCTS when vessel was died.
  - .isactive: (boolean array) 1 if the vessel is active, 0 otherwise.
  - .branch: (int array) number of MCTS in which the new vessel has to maintain the direction or, after that, the ID of the cell that could be a new tip cell of a new sprout.
  - .bx, by: (float arrays) x and y coordinates of the branching direction that the vessel should follow it during certain MCTS, 0.0 otherwise.
  - .ncell: (int array) number of cells in the vessel.
  - .parenttag: (int array) ID of the vessel from which it branched, 0 if it is a initial sprout.
  - .ndescen: (int array) number of sprouts that branched off the vessel.

- contact_perimeter: int array of size $10(M-1) \cdot 10(M-1)$. It is set as a matrix in which each row and column is the cell with the ID of the row or column number. (i,j) position stores the number of pixels shared by cell i and cell j. (i,i) position stores the number of perimeter pixels of cell i. $(i,0)$ position stores the number of neighbors of cell i. $(0,i)$ position stores the number of perimeter pixels occupied by neighbors.

- V: int array of size $M \cdot M$. It stores the value of VEGF concentration on each node.

These structures and arrays have a copy in the CPU and another copy in the GPU. The main modules of the code work with the copy in the GPU and the copy in the CPU is updated to generate the output files.

5.1.2 Module 3. Initialization of random numbers and structures

To generate random numbers, this code uses the library CUDA Random Number Generation (cuRAND) and the Mersenne twister algorithm. The Mersenne twister algorithm is initialized after the declaration of all the variables described in subsection 5.1.1.

The structures defined in subsection 5.1.1 are initialize at zero in CPU and copied to GPU (functions in `init.cpp` file and `init.cu`). Depending on the objective of the simulation, there are two options:

- Start a new simulation (init_MCTS = 0): In terms of the number of initial sprouts we have chosen, structures are modified to set new cells. Two kernels are used to do that (kernels in `init.cu`). The first one assigns one thread to one pixel and modifies CEL and VOX structures, placing equispaced cells of one pixel sized. The second one assigns one thread to one initial sprout and modifies VES structures, filling data of the vessel.
- Continue other simulation (init_MCTS $\neq 0$): Data from output files is loaded in the CPU copy of the structures (functions in `read.cpp` file and `init.cu`).

5.1.3 Module 4. Output files with used parameters and initial structures

In order to have a record of the used parameters and the initial state of the simulation, these data are store in output files with .out extension. `parameters.out` is a file with the name, value and description of the parameters set in `def.h`. The data of structures are stored in the following files, where `X` is the value of init_MCTS:

- `ctagsX.out` stores a $(M-1) \times (M-1)$ matrix with .ctag of VOX values.
- `vtagsX.out` stores a $(M-1) \times (M-1)$ matrix with .vtag of VOX values.
- `dcnsX.out` stores a matrix of size (cells number) × 15. Each row is a cell and each column is an item of the CEL (the first nine) and NDJ (the last six) structures, ordered as follows: .siz, .peri, .tip, .tail, .pos, .tshybrid, .age, .vess, .vegf, .N, .D, .J, .I, .V, Vr.
- `dvX.out` stores a matrix of size (number of initial sprouts) × 12. Each row is a vessel and each column is an item of the VES structure, ordered as follows: .tiptag, .tipvox, .proltag, .birth, .death, .isactive, .branch, .bx, .by, .ncell, .parenttag, .ndescen.
- `periX.out` stores a $10(M-1) \times 10(M-1)$ matrix with the contact_perimeter values.

5.1.4 Module 5. Arrangement of ECM strains and displacements

Given the elasticity problem (2.1.11), certain elements need to be prepared to solve the system and calculate ECM strains and displacements. The matrix K will remain fixed throughout the MCTS, therefore it is calculated once before starting. K is a sparse matrix so the problem needs to be solved with an appropriate method, like the preconditioned conjugate gradient method using ILU decomposition. The algorithm is provided by NVIDIA corporation and it is implemented on the GPU using CUBLAS and CUSPARSE libraries.

The following steps are performed in this module:

1. Set forces made by cells and forces in the boundary nodes. Set restrictions in the boundary nodes. These two actions are carried out in a single kernel that assign one thread to one node (kernel in `init.cu`).
2. Set element stiffness matrices K_e (function in `FE_local.cpp`), eq. (2.1.12).
3. Assemble the global stiffness matrix K from all element stiffness matrices (function in `FE_assemblyl.cpp`).
4. Keep track of Degree Of Freedom (DOF) of K in an array. DOFs that are restricted get a -1, while the remaining DOFs get a number from 0 upwards (function in `FE_assemblyl.cpp`).
5. Reduce K removing the row and column from K for all DOFs with a -1 (function in `FE_assemblyl.cpp`).
6. Prepare K matrix in Compressed Sparse Row (CSR) format, necessary condition to use the PCG algorithm (function in `FE_assemblyl.cpp`). The steps 2 to 5 are functions of the supplementary material of Van Oers `et al.` [92]. However, we solve the system $Ku = f$ using parallel computing, so that K matrix must be adapted. We have made this adaptation through a complex function that converts the output format of K to CSR format. K is decomposed into three arrays:
    - $Kval$ is an array of size $10 \cdot 2 \cdot M \cdot M$. This array contains the non zero values of matrix K.
    - $Kcol$ is an array of size $10 \cdot 2 \cdot M \cdot M$. It contains the index of the column of corresponding nonzero value written in $Kval$.

- *Krow* is an array of size $N_{FE}+1$, where N_{FE} is the number of unrestricted DOFs. It contains the cumulative number of non-zero values in rows of K, starting with 0 in the first gap.

7. Prepare CUBLAS and CUSPARSE data:
   (a) Create CUBLAS context.
   (b) Create CUSPARSE context.
   (c) Description of the K matrix.
   (d) Define the properties of the matrix.
   (e) Create the analysis info object for the K matrix.
   (f) Perform the analysis for the Non-Transpose case.
   (g) Copy K data to ILU0 vals as input.
   (h) Generate the Incomplete LU factor H for the matrix K using cudsparseScsrilu0.
   (i) Create info objects for the ILU0 preconditioner.

5.1.5 Module 6. Arrangement of VEGF concentration

Given the initial-boundary value problem (2.1.7) - (2.1.9), certain elements need to be prepared to solve the problem and calculate the concentration of VEGF.

Firstly, this initial-boundary problem is nondimensionalized. So that we introduce the following scalings in order to nondimensionalize:

$$\tilde{C}=\frac{C}{[C]},\ \tilde{t}=\frac{t}{[t]},\ \tilde{x}=\frac{x}{[x]},\ \tilde{y}=\frac{y}{[x]},\ \tilde{G}=\frac{G}{[G]}$$

where $[C]$, $[t]$, $[x]$ and $[G]$ are non-zero parameters. Substituting these new variables into the partial differential equation (PDE) (2.1.7), we obtain:

$$\frac{[C]}{[t]}\frac{\partial \tilde{C}}{\partial \tilde{t}} = \frac{D_f\,[C]}{[x]^2}\left(\frac{\partial^2 \tilde{C}}{\partial \tilde{x}^2} + \frac{\partial^2 \tilde{C}}{\partial \tilde{y}^2}\right) - \nu\,[C]\,\tilde{C} - [G]\,\tilde{G} \;\Leftrightarrow \left(\text{ dividing by } \frac{D_f[C]}{[x]^2}\right)$$

$$\frac{[x]^2}{D_f\,[t]}\frac{\partial \tilde{C}}{\partial \tilde{t}} = \left(\frac{\partial^2 \tilde{C}}{\partial \tilde{x}^2} + \frac{\partial^2 \tilde{C}}{\partial \tilde{y}^2}\right) - \frac{[x]^2\,\nu}{D_f}\tilde{C} - \frac{[G]\,[x]^2}{D_f\,[C]}\tilde{G}$$

Regarding to the cell binding term, choosing $[G] = \frac{D_f[C]}{[x]^2}$ leads to have two terms which are $\mathcal{O}(1)$, cell binding term and diffusion term, and the PDE obtained is:

$$\frac{[x]^2}{D_f\,[t]}\frac{\partial \tilde{C}}{\partial \tilde{t}} = \triangle \tilde{C} - \frac{[x]^2\,\nu}{D_f}\tilde{C} - \tilde{G}$$

The value of $\frac{[x]^2}{D_f[t]}$ and of $\frac{[x]^2\nu}{D_f}$ depend on the characteristic time scale, equal to 1 MCTS, and the characteristic length scale, on the order of the length of a side of 1 pixel. The value of $[C]$ depends on S and the value of $[G]$ could be known with these data. Regarding to the equivalence between 1 MCTS and the real time units, we use the time of the experiments in the work of Sugihara *et al.* [120] to calibrate Monte Carlo time steps. In this work, the branch elongation takes 36 hours to grow 135 μm, so it would take 132 hours to grow 495 μm. If our simulations take 3001 MCTS approximately, 1 MCTS is 0.044 hours.

$$[t] = 1 \text{ MCTS} \simeq 0.044 \text{ h},\; [x]^2 = \left(\frac{L}{M-1}\right)^2 = \left(\frac{0.495 \text{ mm}}{600}\right)^2 = 0.6806\ \mu\text{m}^2$$

$$[C] = \frac{1}{3}S = 1.67 \times 10^{-7} \text{ pg}/\mu\text{m}^2 \text{ due to the triangle centroid, so}$$

$$[G] = \frac{D_f\,[C]}{[x]^2} = \frac{3.6 \times 10^4\ \mu\text{m}^2/\text{h} \times 1.67 \times 10^{-7} \text{ pg}/\mu\text{m}^2}{0.6806\ \mu\text{m}^2} = 8.83 \times 10^{-3} \text{ pg}/(\mu\text{m}^2 \text{ h})$$

Therefore,

$$\frac{[x]^2}{D_f\,[t]} = \frac{0.6806\ \mu\text{m}^2}{3.6 \times 10^4\ \mu\text{m}^2/\text{h} \times 0.044\text{h}} = 4.2967 \times 10^{-4} \ll 1$$

$$\frac{[x]^2\,\nu}{D_f} = \frac{0.6806\ \mu\text{m}^2 \times 0.6498 \text{ h}^{-1}}{3.6 \times 10^4\ \mu\text{m}^2/\text{h}} = 1.2285 \times 10^{-5} \ll 1$$

The resulting factors are much less than one, so the solution of

$$0 = \triangle\tilde{C}(\tilde{x},\tilde{y},\tilde{t}) - \tilde{G}(\tilde{x},\tilde{y},\tilde{C}),\ (\tilde{x},\tilde{y}) \in \Omega,\ \tilde{t} > 0$$

$$C(0,\tilde{y},\tilde{t}) = 0,\ C(M-1,\tilde{y},\tilde{t}) = \tilde{S} = \frac{S}{[C]},\ C(\tilde{x},0,\tilde{t}) = \frac{\tilde{S}}{M-1}\tilde{x} = C(\tilde{x},M-1,\tilde{t}),\ (\tilde{x},\tilde{y}) \in \Omega,\ \tilde{t} > 0$$

$$C(\tilde{x},\tilde{y},0) = 0,\ (\tilde{x},\tilde{y}) \in \Omega$$

can be used to approximate the VEGF field in our model. This equation can be solved with the Finite Difference Method (FDM) using five-point stencil [134] .

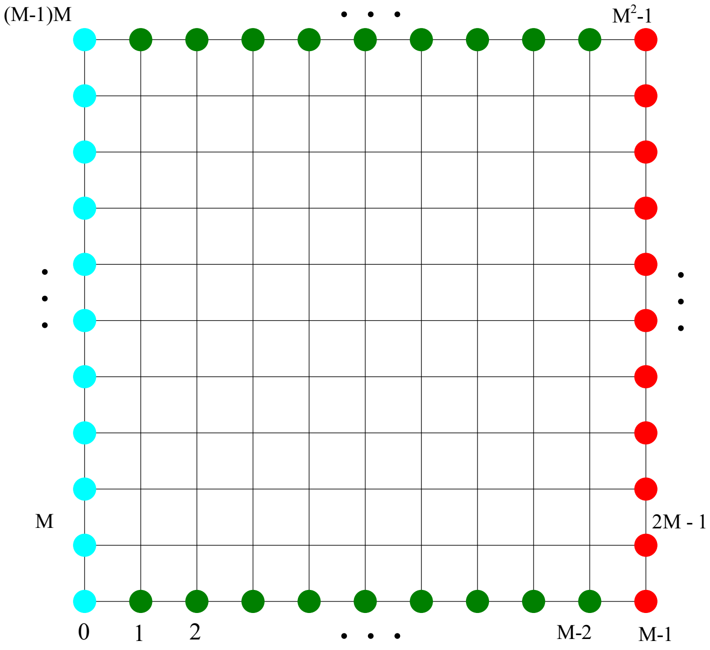

Figure 5.2: **Grid scheme.**

But, first of all and in order to simplify the notation, dimensionless parameters and functions will be used without tildes. The notation ∇^2 is more suitable for the laplacian operator; the symbol $\triangle$ would lead to confusion in numerical work where $\triangle x$ and $\triangle y$

are used for grid spacing. To sum up, we obtain the following Poisson problem:

$$\begin{aligned}
\text{PDE:} \quad & \nabla^2 C(x,y,t) = G(x,y,C),\ 0 < x < M-1,\ 0 < y < M-1,\ t > 0 \\
\text{BC:} \quad & C(0,y,t) = 0,\ C(M-1,y,t) = S,\ 0 < y < M-1,\ t > 0 \\
& C(x,0,t) = \tfrac{S}{M-1}x = C(x,M-1,t),\ 0 < x < M-1,\ t > 0 \\
\text{IC:} \quad & C(x,y,0) = 0,\ 0 < x < M-1,\ 0 < y < M-1.
\end{aligned} \tag{5.1.1}$$

Let C_{ij} represent an approximation to $C(x_i, y_j, t)$, where (x_i, y_j) have been described in domain section. Note that time variable is not been taken into account because the solution of the PDE of (5.1.1) on each MCTS is not time-dependent. To discretize the PDE of (5.1.1), centered finite differences have been used for $x-$ and $y-$derivatives, which gives:

$$\begin{gathered}
\tfrac{1}{h^2}\left(C_{i-1,j} - 2C_{ij} + C_{i+1,j}\right) + \tfrac{1}{h^2}\left(C_{i,j-1} - 2C_{ij} + C_{i,j+1}\right) = G_{ij} \Leftrightarrow \\
\left(C_{i-1,j} + C_{i,j-1} - 4C_{ij} + C_{i+1,j} + C_{i,j+1}\right) = h^2 G_{ij}
\end{gathered} \tag{5.1.2}$$

where $G_{ij} = G(x_i, y_j)$ (we know exactly G function). The equation (5.1.2) changes in function of the point it is focus on and some of them have boundary conditions, so the following equations are written distinguishing each case:

- If $j = 0$ or $j = M-1$ and $\forall i$ (green nodes in figure 5.2 (b)),

$$C_{i,0} = C_{i,M-1} = \frac{S}{M-1} i$$

- If $i = 0$ and $\forall j$ (blue nodes in figure 5.2 (b)),

$$C_{0j} = 0,$$

- If $i = M-1$ and $\forall j$ (red nodes in figure 5.2 (b)),

$$C_{M-1j} = S,$$

- If $i = 1$ and:

- $j = 1$

$$(-4C_{1,1} + C_{1,2} + C_{2,1}) = h^2G_{1,1} - \frac{S}{M-1}, \tag{5.1.3}$$

- $j = M - 2,$

$$(C_{1,M-3} - 4C_{1,M-2} + C_{2,M-2}) = h^2G_{1,M-2} - \frac{S}{M-1}, \tag{5.1.4}$$

- $2 \leq j \leq M - 3,$

$$(C_{1,j-1} - 4C_{1,j} + C_{1,j+1} + C_{2,j}) = h^2G_{1,j}, \tag{5.1.5}$$

- If $i = M - 2$ and:

  - $j = 1$

$$(C_{M-3,1} - 4C_{M-2,1} + C_{M-2,2}) = h^2G_{M-2,1} - \frac{S}{M-1}(M-2) - S, \tag{5.1.6}$$

  - $j = M - 2,$

$$\begin{aligned}(C_{M-3,M-2} + C_{M-2,M-3} - 4C_{M-2,M-2}) = \\ h^2G_{M-2,M-2} - \frac{S}{M-1}(M-2) - S,\end{aligned} \tag{5.1.7}$$

  - $2 \leq j \leq M - 3,$

$$(C_{M-3,j} + C_{M-2,j-1} - 4C_{M-2,j} + C_{M-2,j+1}) = h^2G_{M-2,j} - S, \tag{5.1.8}$$

- If $j = 1$ and $2 \leq i \leq M - 3$

$$(C_{i-1,1} - 4C_{i,1} + C_{i,2} + C_{i+1,1}) = h^2G_{i,1} - \frac{S}{M-1}i, \tag{5.1.9}$$

- If $j = M - 2$ and $2 \leq i \leq M - 3$

$$(C_{i-1,M-2} + C_{i,M-3} - 4C_{i,M-2} + C_{i+1,M-2}) = h^2G_{i,M-2} - \frac{S}{M-1}i, \tag{5.1.10}$$

- If $2 \leq i \leq M - 3$ and $2 \leq j \leq M - 3,$

$$(C_{i-1,j} + C_{i,j-1} - 4C_{ij} + C_{i,j+1} + C_{i+1,j}) = h^2G_{ij}, \tag{5.1.11}$$

The above equations can be collected together into a matrix equation $Ax = R$. The colored nodes of the figure 5.2 (b) are not considered since their values are already known. So, the equations to take into account are from (5.1.3) to (5.1.11). A is a matrix of size N_{FD}^2, with $N_{FD} = (M-3)^2$ that contains the factors that appear multiplying C_{ij} terms, i.e. 0, 1 and -4. x is an array of size N_{FD} that contains the values for C_{ij} terms that satisfy the matrix form equation. The first time we calculate x, it is initialized at zero, but in future Monte Carlo time steps we use the solution calculated in the previous MCTS. R is an array of size N_{FD} and it is formed by the right - hand side of the previous equations.

A is a sparse matrix so the system is needed to be solved with an appropriate method, like the PCG method using ILU decomposition. The algorithm is provided by CUDA and uses a CSR format, so we have decomposed A into three arrays:

- *Aval* is an array of size $nz_{FD} = 5N_{FD} - 4\sqrt{N_{FD}}$. nz_{FD} is the number of non zero values of A, i.e. five - point finite difference scheme minus number of frontier nodes per boundary times number of boundaries. This array contains the non zero values of matrix A.

- *Acol* is an array of size nz_{FD}. It contains the index of the column of corresponding nonzero value written in *Aval*.

- *Arow* is an array of size $N_{FD} + 1$. It contains the cumulative number of non-zero values in rows of A, starting with 0 in the first gap.

These three arrays, plus x and R, are needed to use the mentioned algorithm. After that, the x array is included in a bigger one V, which also contains the values of VEGF concentration at the boundaries. Thus, the following steps are performed in this module:

1. Initialize x and R.
2. Define A matrix in CSR format.

3. Prepare CUBLAS and CUSPARSE data:
    (a) Create CUBLAS context.
    (b) Create CUSPARSE context.
    (c) Description of the A matrix.
    (d) Define the properties of the matrix.
    (e) Create the analysis info object for the A matrix.
    (f) Perform the analysis for the Non-Transpose case.
    (g) Copy A data to ILU0 vals as input.
    (h) Generate the Incomplete LU factor H for the matrix A using cudsparseScsrilu0.
    (i) Create info objects for the ILU0 preconditioner.
4. Solve $Ax = R$ system using PCG method.
5. Include array x in V. This takes place in a kernel where is assigned one thread to one node (kernel in `chemotaxis.cu`).
6. Associate to each cell the value of VEGF concentration on the bottom left grid point of the pixel selected in .tip of CEL structure, i.e., update .vegf of CEL structure. This takes place in a kernel where is assigned one thread to one cell (kernel in `chemotaxis.cu`).

5.1.6 Modules 7. & 16. Output files with structures

These output files are used to save data about the simulation every certain MCTS and then to be able to visualize some data or make statistics. Files are generated with an .out extension and they store data of structures. The frequency at which these data are stored can change according to interest of the simulation, we usually do it every 50 MCTS. Before generating the files, the copy in the CPU is updated with the new data of the structures that are in the GPU.

The generated files at `X` MCTS are:

- `ctagsX.out` stores a $(M-1)\times(M-1)$ matrix with .ctag of VOX values.
- `vtagsX.out` stores a $(M-1)\times(M-1)$ matrix with .vtag of VOX values.
- `dcnsX.out` stores a matrix of size (cells number) × 15. Each row is a cell and each column is an item of the CEL (the first nine) and NDJ (the last six) structures, ordered as follows: .siz, .peri, .tip, .tail, .pos, .tshybrid, .age, .vess, .vegf, .N, .D, .J, .I, .V, Vr.
- `dvX.out` stores a matrix of size (number of initial sprouts) × 12. Each row is a vessel and each column is an item of the VES structure, ordered as follows: .tiptag, .tipvox, .proltag, .birth, .death, .isactive, .branch, .bx, .by, .ncell, .parenttag, .ndescen.
- `pstrain.out` stores a matrix of size $(M\cdot M)\times$ 6. Each row is a node and columns are: .fx, .fy, larger eigenvalue, first component of the eigenvector of this eigenvalue, second component of the eigenvector of this eigenvalue, the other eigenvalue.
- `periX.out` stores a $10(M-1)\times 10(M-1)$ matrix with the contact_perimeter values.
- `VEGF.out` stores a $M\times M$ matrix with values of V.

5.1.7 Module 8. Cell source

In our model, numerical simulations show that a growing sprout may separate from the primary blood vessel more than one cell diameter (10 μm). As the primary vessel is a source of ECs, we create a new stalk cell to fill the resulting hole if this happens. For this purpose, a kernel which assigns one thread to one pixel places as many cells as they fit between the parent vessel and the closest cell of the sprout.

The following steps are performed in this module (kernels in `cellsource.cu`):

1. For each initial tip, find the pixel belonging to a cell that is closest to the point where the first cell of this initial tip was place.
2. Kernel that places as many cells as they could be placed between at the left of the pixel found before and $x = 0$. The distance between this pixel and $x = 0$ must be, at least, one cell diameter (10 μm) to place one cell. This kernel assigns one thread to one pixel.

We only take into account this module in case (B) (cell elongation & cell overtaking) described in chapter 2.

5.1.8 Module 9. Branching

In this module, the branching is carried out as it is described in branching subsection of 2.1. The following steps are performed in this module (kernels in `branching.cu`):

1. Kernel that calculates the direction of branching of each possible new tip cells. The average modulus and argument for the direction of branching are defined in (2.1.25). This kernel assigns one thread to one pixel.
2. Kernel that calculates the probability of branching taking into account the direction and their neighbors. This kernel assigns one thread to one vessel.

3. Kernel that updates VOX structure with new tip cells, in the case where branching has been accepted. This kernel assigns one thread to one pixel.
4. Kernel that updates CEL and VES structure. This kernel assigns one thread to one vessel.
5. Kernel that checks if one of these new tip cells needs to jump in the direction of branching and update CEL and VES structures, if necessary. This kernel assigns one thread to one vessel.
6. Kernel that updates VOX structure after cell's jumping, if necessary. This kernel assigns one thread to one pixel.

5.1.9 Module 10. Cell proliferation

Cell splitting and proliferation, described in cell proliferation and duration of one MCTS subsection of 2.1, is implemented in this module. The following steps are performed in this module (kernels in `proliferation.cu`):

1. Kernel that builds an array with the labels of the cell that can proliferate for each vessel. This kernel assigns one thread to one vessel.
2. Kernel that checks if cells in the built array meet certain requirements to proliferate. *nprol* is the number of cells that have met the requirements. This kernel assigns one thread to one vessel.
3. Kernel that prepares data arrays for K-means algorithm. This kernel runs *nprol* times.
4. K-means algorithm is used to form two groups of pixels of each cell. After that, every structure and contact_perimeter array are updated with the new data of these two cell that have formed through the groups of pixels. The two kernels involved run sequentially in a loop, *nprol* times, one for each cell.

5.1.10 Module 11. VEGF concentration

After the preparations described in subsection 5.1.5 before starting the loop over MCTS, the system of linear equations to calculate VEGF concentration is solved every MCTS. The following steps are performed in this module (kernels in `chemotaxis.cu`):

1. Kernel that calculates right-hand side R of the system $Ax = R$ (see subsection 5.1.5). This kernel assigns one thread to one node.
2. Solve $Ax = R$ system using PCG method where x is the solution calculated in the last MCTS.
3. Kernel that includes the array x in V. This kernel assigns one thread to one node.
4. Kernel that associates to each cell the value of VEGF concentration on the bottom left grid point of the pixel selected in .tip of CEL structure, i.e., update .vegf of CEL structure. This kernel assigns one thread to one cell.

5.1.11 Module 12. Signaling processes

In this module, the nondimensionalized version of the system of Ordinary Differential Equations (ODEs), Eqs. (2.1.16) - (2.1.21) of the main text, is numerically solved.

Firstly, we introduce the following scalings in order to nondimensionalize:

$$\text{(eq. (2.1.16))} \;\rightarrow N_0 \sim k_C\,[N]\,[D] \Leftrightarrow [N]^2 \sim \frac{N_0}{k_C} \sim \frac{D_0}{k_C} \Rightarrow [N] = \sqrt{\frac{D_0}{k_C}} = \sqrt{2}\times 10^3 \text{ molec.}$$

$$\text{(eq. (2.1.17))} \;\rightarrow D_0 \sim k_C\,[D]\,[N] \Leftrightarrow [D]^2 \sim \frac{D_0}{k_C} \Rightarrow [D] = \sqrt{\frac{D_0}{k_C}} = \sqrt{2}\times 10^3 \text{ molec.}$$

$$\frac{[D]}{[t]} \sim D_0 \Leftrightarrow [t] \sim \frac{[D]}{D_0} \Rightarrow [t] = \frac{1}{\sqrt{k_C D_0}} = \sqrt{2}\text{ h}$$

$$\text{(eq. (2.1.18))} \;\rightarrow J_0 \sim k_C\,[J]\,[N] \Leftrightarrow [J]^2 \sim \frac{J_0}{k_C} \sim \frac{D_0}{k_C} \Rightarrow [J] = \sqrt{\frac{D_0}{k_C}} = \sqrt{2}\times 10^3 \text{ molec.}$$

$$\Rightarrow [N] = [D] = [J]$$

$$\text{(eq. (2.1.19))} \;\rightarrow k_T\,[N]\,[D] \sim \gamma_S\,[I] \Leftrightarrow k_T\,[D]^2 \sim \gamma_S\,[I] \Rightarrow [I] = \frac{k_T D_0}{k_C \gamma_S} = 10^2 \text{ molec.}$$

$$\text{(eq. (2.1.20))} \;\rightarrow V_{R0} \sim \gamma\,[V_R] \Rightarrow [V_R] = \frac{V_{R0}}{\gamma} = 10^4 \text{ molec.}$$

$$\text{(eq. (2.1.21))} \;\rightarrow k_T\,[V_R]\,[V] \sim \gamma_S\,[V] \Leftrightarrow k_T\frac{V_{R0}}{\gamma} \sim \gamma_S \Leftrightarrow 2.5\times 10^{-5}\times 10^4 \text{ molec.} = 0.25 \sim 0.5 \;\checkmark$$

$$[V] = V_0 = 2\times 10^2 \text{ molec.}$$

$$V_{ext} \rightarrow V_{ext} = \sum_{j\in\text{neigh.}} V_j + V_{ECM},\; V_{ECM} = \sqrt{\frac{1}{2}\times\frac{0.35}{7.472\times 10^{-8}}\times\frac{1.65}{0.01}} = 2\times 10^4$$

Thereby,

$$\hat{N} = \frac{N}{[N]} = N\sqrt{\frac{k_C}{D_0}}, \qquad \hat{D} = \frac{D}{[D]} = D\sqrt{\frac{k_C}{D_0}},$$

$$\hat{J} = \frac{J}{[J]} = J\sqrt{\frac{k_C}{D_0}}, \qquad \hat{I} = \frac{I}{[I]} = I\frac{k_C\gamma_S}{k_T D_0},$$

$$\hat{V_R} = \frac{V_R}{[V_R]} = V_R\frac{\gamma}{V_{R0}}, \qquad \hat{V} = \frac{V}{[V]} = V\frac{\gamma}{V_{R0}},$$

$$\hat{N}_{ext} = \frac{N_{ext}}{[N]} = N_{ext}\sqrt{\frac{k_C}{D_0}}, \qquad \hat{D}_{ext} = \frac{D_{ext}}{[D]} = D_{ext}\sqrt{\frac{k_C}{D_0}},$$

$$\hat{J}_{ext} = \frac{J_{ext}}{[J]} = J_{ext}\sqrt{\frac{k_C}{D_0}}, \qquad \hat{V}_{ext} = \frac{V_{ext}}{[V_{ext}]} = V_{ext}\frac{1}{V_{ECM}}$$

$$\hat{t} = \frac{t}{[t]} = t\sqrt{k_C D_0},$$

Note that N_{ext}, D_{ext} and J_{ext} are actually the sums of the N, D and J of the neighboring cells, respectively. V_{ext} is the sum of the neighboring cells plus the VEGF in the extracellular matrix.

Therefore, we obtain the following equations:

- From equation (2.1.16):

$$\begin{aligned}
\frac{[N]}{[t]}\frac{d\hat{N}}{d\hat{t}} &= N_0\left(H^-\left([I]\,\hat{I}\right)(1-\lambda_{I,N})+\lambda_{I,N}\right)\\
&\quad -[N]\,\hat{N}\Big[\left(k_C\,[D]\,\hat{D}+k_T\,[D]\,\hat{D}_{ext}\right)\left(H^-\left([I]\,\hat{I}\right)(1-\lambda_{F,D})+\lambda_{F,D}\right)\\
&\quad +\left(k_C\,[J]\,\hat{J}+k_T\,[J]\,\hat{J}_{ext}\right)\left(H^-\left([I]\,\hat{I}\right)(1-\lambda_{F,J})+\lambda_{F,J}\right)\Big]-\gamma\,[N]\,\hat{N}\Leftrightarrow\\
\frac{d\hat{N}}{d\hat{t}} &= \frac{N_0\,[t]}{[N]}\left(\frac{1}{1+\left(\frac{[I]\hat{I}}{I_0}\right)^{n_N}}(1-\lambda_{I,N})+\lambda_{I,N}\right)\\
&\quad -\hat{N}\left[\left(k_C\,[D]\,[t]\,\hat{D}+k_T\,[D]\,[t]\,\hat{D}_{ext}\right)\left(\frac{1}{1+\left(\frac{[I]\hat{I}}{I_0}\right)^{n_F}}(1-\lambda_{F,D})+\lambda_{F,D}\right)\right.\\
&\quad \left.+\left(k_C\,[J]\,[t]\,\hat{J}+k_T\,[J]\,[t]\,\hat{J}_{ext}\right)\left(\frac{1}{1+\left(\frac{[I]\hat{I}}{I_0}\right)^{n_F}}(1-\lambda_{F,J})+\lambda_{F,J}\right)\right]-\gamma\,[t]\,\hat{N}\Leftrightarrow\\
\frac{d\hat{N}}{d\hat{t}} &= \frac{N_0}{D_0}\left(\frac{1}{1+\left(\frac{k_T D_0}{k_C\gamma_S I_0}\hat{I}\right)^{n_N}}(1-\lambda_{I,N})+\lambda_{I,N}\right)\\
&\quad -\hat{N}\left[\left(\hat{D}+\frac{k_T}{k_C}\hat{D}_{ext}\right)\left(\frac{1}{1+\left(\frac{k_T D_0}{k_C\gamma_S I_0}\hat{I}\right)^{n_F}}(1-\lambda_{F,D})+\lambda_{F,D}\right)\right.\\
&\quad \left.+\left(\hat{J}+\frac{k_T}{k_C}\hat{J}_{ext}\right)\left(\frac{1}{1+\left(\frac{k_T D_0}{k_C\gamma_S I_0}\hat{I}\right)^{n_F}}(1-\lambda_{F,J})+\lambda_{F,J}\right)\right]-\frac{\gamma}{\sqrt{k_C D_0}}\hat{N}\\
&\Leftrightarrow (n_N=2,\ \lambda_{I,N}=2,\ n_F=1,\ \lambda_{F,D}=3,\ \lambda_{F,J}=0.3)\\
\frac{d\hat{N}}{d\hat{t}} &= \frac{N_0}{D_0}\left(2-\frac{1}{1+\left(\frac{k_T D_0}{k_C\gamma_S I_0}\hat{I}\right)^2}\right)-\hat{N}\left[\left(\hat{D}+\frac{k_T}{k_C}\hat{D}_{ext}\right)\left(3-2\frac{1}{1+\left(\frac{k_T D_0}{k_C\gamma_S I_0}\hat{I}\right)}\right)\right.\\
&\quad \left.+\left(\hat{J}+\frac{k_T}{k_C}\hat{J}_{ext}\right)\left(0.3+0.7\frac{1}{1+\left(\frac{k_T D_0}{k_C\gamma_S I_0}\hat{I}\right)}\right)\right]-\frac{\gamma}{\sqrt{k_C D_0}}\hat{N}
\end{aligned}$$

- From equation (2.1.17):

$$
\begin{aligned}
\frac{[D]}{[t]}\frac{d\hat{D}}{d\hat{t}} &= D_0\left(H^-\left([I]\,\hat{I}\right)(1-\lambda_{I,D})+\lambda_{I,D}\right)\left(H^-\left([V]\,\hat{V}\right)(1-\lambda_{V,D})+\lambda_{V,D}\right)\\
&\quad-[D]\,\hat{D}\left[k_C\,[N]\,\hat{N}\left(H^-\left([I]\,\hat{I}\right)(1-\lambda_{F,D})+\lambda_{F,D}\right)+k_T\,[N]\,\hat{N}_{ext}\right]-\gamma\,[D]\,\hat{D}\Leftrightarrow\\
\frac{d\hat{D}}{d\hat{t}} &= \frac{D_0\,[t]}{[D]}\left(\frac{1}{1+\left(\frac{[I]\hat{I}}{I_0}\right)^{n_D}}(1-\lambda_{I,D})+\lambda_{I,D}\right)\left(\frac{1}{1+\left(\frac{[V]\hat{V}}{V_0}\right)^{n_D}}(1-\lambda_{V,D})+\lambda_{V,D}\right)\\
&\quad-\hat{D}\left[k_C\,[t]\,[N]\,\hat{N}\left(\frac{1}{1+\left(\frac{[I]\hat{I}}{I_0}\right)^{n_F}}(1-\lambda_{F,D})+\lambda_{F,D}\right)+k_T\,[N]\,[t]\,\hat{N}_{ext}\right]-\gamma\,[t]\,\hat{D}\Leftrightarrow\\
\frac{d\hat{D}}{d\hat{t}} &= \left(\frac{1}{1+\left(\frac{k_T D_0}{k_C\gamma_S I_0}\hat{I}\right)^{n_D}}(1-\lambda_{I,D})+\lambda_{I,D}\right)\left(\frac{1}{1+\hat{V}^{n_D}}(1-\lambda_{V,D})+\lambda_{V,D}\right)\\
&\quad-\hat{D}\left[\hat{N}\left(\frac{1}{1+\left(\frac{k_T D_0}{k_C\gamma_S I_0}\hat{I}\right)^{n_F}}(1-\lambda_{F,D})+\lambda_{F,D}\right)+\frac{k_T}{k_C}\hat{N}_{ext}\right]-\frac{\gamma}{\sqrt{k_C D_0}}\hat{D}\\
&\quad\Leftrightarrow\left(n_D=2,\ \lambda_{I,D}=0,\ \lambda_{V,D}=2,\ n_F=1,\ \lambda_{F,D}=3\right)\\
\frac{d\hat{D}}{d\hat{t}} &= \left(\frac{1}{1+\left(\frac{k_T D_0}{k_C\gamma_S I_0}\hat{I}\right)^2}\right)\left(2-\frac{1}{1+\hat{V}^2}\right)-\hat{D}\left[\hat{N}\left(3-2\frac{1}{1+\left(\frac{k_T D_0}{k_C\gamma_S I_0}\hat{I}\right)}\right)+\frac{k_T}{k_C}\hat{N}_{ext}\right]\\
&\quad-\frac{\gamma}{\sqrt{k_C D_0}}\hat{D}
\end{aligned}
$$

- From equation (2.1.18):

$$\begin{aligned}
\frac{[J]}{[t]}\frac{d\hat{J}}{d\hat{t}} &= J_0\left(H^-\left([I]\,\hat{I}\right)(1-\lambda_{I,J})+\lambda_{I,J}\right)\\
&\quad-[J]\,\hat{J}\left[k_C\,[N]\,\hat{N}\left(H^-\left([I]\,\hat{I}\right)(1-\lambda_{F,J})+\lambda_{F,J}\right)+k_T\,[N]\,\hat{N}_{ext}\right]-\gamma\,[J]\,\hat{J}\Leftrightarrow\\
\frac{d\hat{J}}{d\hat{t}} &= \frac{J_0\,[t]}{[J]}\left(\frac{1}{1+\left(\frac{[I]\hat{I}}{I_0}\right)^{n_J}}(1-\lambda_{I,J})+\lambda_{I,J}\right)\\
&\quad-\hat{J}\left[k_C\,[N]\,[t]\,\hat{N}\left(\frac{1}{1+\left(\frac{[I]\hat{I}}{I_0}\right)^{n_F}}(1-\lambda_{F,J})+\lambda_{F,J}\right)+k_T\,[t]\,[N]\,\hat{N}_{ext}\right]-\gamma\,[t]\,\hat{J}\Leftrightarrow\\
\frac{d\hat{J}}{d\hat{t}} &= \frac{J_0}{D_0}\left(\frac{1}{1+\left(\frac{k_T D_0}{k_C\gamma_S I_0}\hat{I}\right)^{n_J}}(1-\lambda_{I,J})+\lambda_{I,J}\right)\\
&\quad-\hat{J}\left[\hat{N}\left(\frac{1}{1+\left(\frac{k_T D_0}{k_C\gamma_S I_0}\hat{I}\right)^{n_F}}(1-\lambda_{F,J})+\lambda_{F,J}\right)+\frac{k_T}{k_C}\hat{N}_{ext}\right]-\frac{\gamma}{\sqrt{k_C D_0}}\hat{J}\\
&\quad\Leftrightarrow(n_J=5,\ \lambda_{I,J}=2,\ n_F=1,\ \lambda_{F,J}=0.3)\\
\frac{d\hat{J}}{d\hat{t}} &= \frac{J_0}{D_0}\left(2-\frac{1}{1+\left(\frac{k_T D_0}{k_C\gamma_S I_0}\hat{I}\right)^{5}}\right)-\hat{J}\left[\hat{N}\left(0.3+0.7\frac{1}{1+\left(\frac{k_T D_0}{k_C\gamma_S I_0}\hat{I}\right)}\right)+\frac{k_T}{k_C}\hat{N}_{ext}\right]-\frac{\gamma}{\sqrt{k_C D_0}}\hat{J}
\end{aligned}$$

- From equation (2.1.19):

$$\begin{aligned}
\frac{[I]}{[t]}\frac{d\hat{I}}{d\hat{t}} &= k_T\,[N]\,\hat{N}\,\Big[[D]\,\hat{D}_{ext}\Big(H^-\Big([I]\,\hat{I}\Big)\,(1-\lambda_{F,D})+\lambda_{F,D}\Big) \\
&\quad +[J]\,\hat{J}_{ext}\Big(H^-\Big([I]\,\hat{I}\Big)\,(1-\lambda_{F,J})+\lambda_{F,J}\Big)\Big]-\gamma_S\,[I]\,\hat{I}\Leftrightarrow \\
\frac{d\hat{I}}{d\hat{t}} &= \frac{k_T\,[N]^2\,[t]}{[I]}\hat{N}\left[\hat{D}_{ext}\left(\frac{1}{1+\left(\frac{[I]\hat{I}}{I_0}\right)^{n_F}}\,(1-\lambda_{F,D})+\lambda_{F,D}\right)\right. \\
&\quad \left.+\hat{J}_{ext}\left(\frac{1}{1+\left(\frac{[I]\hat{I}}{I_0}\right)^{n_F}}\,(1-\lambda_{F,J})+\lambda_{F,J}\right)\right]-\gamma_S\,[t]\,\hat{I}\Leftrightarrow \\
\frac{d\hat{I}}{d\hat{t}} &= \frac{\gamma_S}{\sqrt{k_C D_0}}\hat{N}\left[\hat{D}_{ext}\left(\frac{1}{1+\left(\frac{k_T D_0}{k_C\gamma_S I_0}\hat{I}\right)^{n_F}}\,(1-\lambda_{F,D})+\lambda_{F,D}\right)\right. \\
&\quad \left.+\hat{J}_{ext}\left(\frac{1}{1+\left(\frac{k_T D_0}{k_C\gamma_S I_0}\hat{I}\right)^{n_F}}\,(1-\lambda_{F,J})+\lambda_{F,J}\right)\right]-\frac{\gamma_S}{\sqrt{k_C D_0}}\hat{I} \\
&\quad \Leftrightarrow (n_F=1,\ \lambda_{F,D}=3,\ \lambda_{F,J}=0.3) \\
\frac{d\hat{I}}{d\hat{t}} &= \frac{\gamma_S}{\sqrt{k_C D_0}}\hat{N}\left[\hat{D}_{ext}\left(3-2\frac{1}{1+\left(\frac{k_T D_0}{k_C\gamma_S I_0}\hat{I}\right)}\right)+\hat{J}_{ext}\left(0.3+0.7\frac{1}{1+\left(\frac{k_T D_0}{k_C\gamma_S I_0}\hat{I}\right)}\right)\right]-\frac{\gamma_S}{\sqrt{k_C D_0}}\hat{I}
\end{aligned}$$

- From equation (2.1.20):

$$\begin{aligned}
\frac{[V_R]}{[t]}\frac{d\hat{V}_R}{d\hat{t}} &= V_{R0}\Big(H^-\Big([I]\,\hat{I}\Big)\,(1-\lambda_{I,V_R})+\lambda_{I,V_R}\Big)-k_T\,[V_R]\,[V_{ext}]\,\hat{V}_R\hat{V}_{ext}-\gamma\,[V_R]\,\hat{V}_R\Leftrightarrow \\
\frac{d\hat{V}_R}{d\hat{t}} &= \frac{V_{R0}\,[t]}{[V_R]}\left(\frac{1}{1+\left(\frac{[I]\hat{I}}{I_0}\right)^{n_{V_R}}}\,(1-\lambda_{I,V_R})+\lambda_{I,V_R}\right)-k_T\,[V_{ext}]\,[t]\,\hat{V}_{ext}\hat{V}_R-\gamma\,[t]\,\hat{V}_R\Leftrightarrow \\
\frac{d\hat{V}_R}{d\hat{t}} &= \frac{\gamma}{\sqrt{k_C D_0}}\left(\frac{1}{1+\left(\frac{k_T D_0}{k_C\gamma_S I_0}\hat{I}\right)^{n_{V_R}}}\,(1-\lambda_{I,V_R})+\lambda_{I,V_R}\right)-\frac{k_T V_{ECM}}{\sqrt{k_C D_0}}\hat{V}_{ext}\hat{V}_R-\frac{\gamma}{\sqrt{k_C D_0}}\hat{V}_R \\
&\quad \Leftrightarrow (n_{V_R}=2,\ \lambda_{I,V_R}=0) \\
\frac{d\hat{V}_R}{d\hat{t}} &= \frac{\gamma}{\sqrt{k_C D_0}}\left(\frac{1}{1+\left(\frac{k_T D_0}{k_C\gamma_S I_0}\hat{I}\right)^2}\right)-\frac{k_T V_{ECM}}{\sqrt{k_C D_0}}\hat{V}_{ext}\hat{V}_R-\frac{\gamma}{\sqrt{k_C D_0}}\hat{V}_R
\end{aligned}$$

- From equation (2.1.21):

$$\begin{aligned}
\frac{[V]}{[t]}\frac{d\hat{V}}{d\hat{t}} &= k_T\,[V_{ext}]\,\hat{V}_{ext}\,[V_R]\,\hat{V}_R - \gamma_S\,[V]\,\hat{V} \Leftrightarrow \\
\frac{d\hat{V}}{d\hat{t}} &= \frac{k_T\,[V_{ext}]\,[V_R]\,[t]}{[V]}\hat{V}_{ext}\hat{V}_R - \gamma_S\,[t]\,\hat{V} \Leftrightarrow \\
\frac{d\hat{V}}{d\hat{t}} &= \frac{k_T V_{ECM} V_{R0}}{\gamma V_0\sqrt{k_C D_0}}\hat{V}_{ext}\hat{V}_R - \frac{\gamma_S}{\sqrt{k_C D_0}}\hat{V}
\end{aligned}$$

To sum up, the dimensionless version of equations (2.1.16) - (2.1.21) is

$$\begin{aligned}
\frac{d\hat{N}}{d\hat{t}} =& \frac{N_0}{D_0}\left(2 - \frac{1}{1+\left(\frac{k_T D_0}{k_C\gamma_S I_0}\hat{I}\right)^2}\right) - \hat{N}\left[\left(\hat{D} + \frac{k_T}{k_C}\hat{D}_{ext}\right)\left(3 - 2\frac{1}{1+\left(\frac{k_T D_0}{k_C\gamma_S I_0}\hat{I}\right)}\right)\right. \\
&\left. + \left(\hat{J} + \frac{k_T}{k_C}\hat{J}_{ext}\right)\left(0.3 + 0.7\frac{1}{1+\left(\frac{k_T D_0}{k_C\gamma_S I_0}\hat{I}\right)}\right)\right] - \frac{\gamma}{\sqrt{k_C D_0}}\hat{N} \\
\frac{d\hat{D}}{d\hat{t}} =& \left(\frac{1}{1+\left(\frac{k_T D_0}{k_C\gamma_S I_0}\hat{I}\right)^2}\right)\left(2 - \frac{1}{1+\hat{V}^2}\right) - \hat{D}\left[\hat{N}\left(3 - 2\frac{1}{1+\left(\frac{k_T D_0}{k_C\gamma_S I_0}\hat{I}\right)}\right) + \frac{k_T}{k_C}\hat{N}_{ext}\right] \\
&- \frac{\gamma}{\sqrt{k_C D_0}}\hat{D} \\
\frac{d\hat{J}}{d\hat{t}} =& \frac{J_0}{D_0}\left(2 - \frac{1}{1+\left(\frac{k_T D_0}{k_C\gamma_S I_0}\hat{I}\right)^5}\right) - \hat{J}\left[\hat{N}\left(0.3 + 0.7\frac{1}{1+\left(\frac{k_T D_0}{k_C\gamma_S I_0}\hat{I}\right)}\right) + \frac{k_T}{k_C}\hat{N}_{ext}\right] - \frac{\gamma}{\sqrt{k_C D_0}}\hat{J} \\
\frac{d\hat{I}}{d\hat{t}} =& \frac{\gamma_S}{\sqrt{k_C D_0}}\hat{N}\left[\hat{D}_{ext}\left(3 - 2\frac{1}{1+\left(\frac{k_T D_0}{k_C\gamma_S I_0}\hat{I}\right)}\right) + \hat{J}_{ext}\left(0.3 + 0.7\frac{1}{1+\left(\frac{k_T D_0}{k_C\gamma_S I_0}\hat{I}\right)}\right)\right] - \frac{\gamma_S}{\sqrt{k_C D_0}}\hat{I} \\
\frac{d\hat{V}_R}{d\hat{t}} =& \frac{\gamma}{\sqrt{k_C D_0}}\left(\frac{1}{1+\left(\frac{k_T D_0}{k_C\gamma_S I_0}\hat{I}\right)^2}\right) - \frac{k_T V_{ECM}}{\sqrt{k_C D_0}}\hat{V}_{ext}\hat{V}_R - \frac{\gamma}{\sqrt{k_C D_0}}\hat{V}_R \\
\frac{d\hat{V}}{d\hat{t}} =& \frac{k_T V_{ECM} V_{R0}}{\gamma V_0\sqrt{k_C D_0}}\hat{V}_{ext}\hat{V}_R - \frac{\gamma_S}{\sqrt{k_C D_0}}\hat{V}
\end{aligned}$$

where,

$$\begin{aligned}
\alpha &= \frac{N_0}{D_0} = 1.20, & \beta &= \frac{J_0}{D_0} = 1.00,\\
\kappa &= \frac{k_T}{k_C} = 0.05, & \eta &= \frac{k_T D_0}{k_C \gamma_S I_0} = 0.50,\\
\sigma &= \frac{k_T V_{ECM}}{\sqrt{k_C D_0}} = 0.70, & \xi &= \frac{k_T V_{ECM} V_{R0}}{\gamma V_0 \sqrt{k_C D_0}} = 35.35,\\
\tau &= \frac{\gamma}{\sqrt{k_C D_0}} = 0.14, & \tau_S &= \frac{\gamma_S}{\sqrt{k_C D_0}} = 0.70,
\end{aligned}$$

Therefore,

$$\begin{aligned}
\frac{d\hat{N}}{d\hat{t}} &= \alpha \left(2 - \frac{1}{1 + \left(\eta \hat{I}\right)^2} \right) - \hat{N} \left[\left(\hat{D} + \kappa \hat{D}_{ext} \right) \left(3 - 2 \frac{1}{1 + \left(\eta \hat{I}\right)} \right) \right.\\
&\quad \left. + \left(\hat{J} + \kappa \hat{J}_{ext} \right) \left(0.3 + 0.7 \frac{1}{1 + \left(\eta \hat{I}\right)} \right) \right] - \tau \hat{N}\\
\frac{d\hat{D}}{d\hat{t}} &= \left(\frac{1}{1 + \left(\eta \hat{I}\right)^2} \right) \left(2 - \frac{1}{1 + \hat{V}^2} \right) - \hat{D} \left[\hat{N} \left(3 - 2 \frac{1}{1 + \left(\eta \hat{I}\right)} \right) + \kappa \hat{N}_{ext} \right] - \tau \hat{D}\\
\frac{d\hat{J}}{d\hat{t}} &= \beta \left(2 - \frac{1}{1 + \left(\eta \hat{I}\right)^5} \right) - \hat{J} \left[\hat{N} \left(0.3 + 0.7 \frac{1}{1 + \left(\eta \hat{I}\right)} \right) + \kappa \hat{N}_{ext} \right] - \tau \hat{J}\\
\frac{d\hat{I}}{d\hat{t}} &= \tau_S \hat{N} \left[\hat{D}_{ext} \left(3 - 2 \frac{1}{1 + \left(\eta \hat{I}\right)} \right) + \hat{J}_{ext} \left(0.3 + 0.7 \frac{1}{1 + \left(\eta \hat{I}\right)} \right) \right] - \tau_S \hat{I}\\
\frac{d\hat{V}_R}{d\hat{t}} &= \tau \left(\frac{1}{1 + \left(\eta \hat{I}\right)^2} \right) - \sigma \hat{V}_{ext} \hat{V}_R - \tau \hat{V}_R\\
\frac{d\hat{V}}{d\hat{t}} &= \xi \hat{V}_{ext} \hat{V}_R - \tau_S \hat{V}
\end{aligned}$$

This system is solved with the explicit Euler method each 10 MCTS, due to the difficulty of parallelize this module. According to Boareto *et al.* [110], the role of tip and stalk cells could change every two hours, so that updating parameters values of the proteins involved each 0.44 hours is enough. Additionally, for a given cell i, the system have some ‘external’ terms that need the number of some proteins of the neighbors of cell i, so the system of ODEs of a cell is also coupled with other system of ODEs of other cells.

On each step of time, we consider two kernels that assign one thread to one cell. The first one calculates the ‘external’ terms and solves the system. The second one updates the approximate solution in the NDJ structure because that will be the data to be load next time step. The maximum number of steps has been chosen considers the convergence of the Euler method. Other numerical methods have been considered but have been discarded because they required more computational time and they did not improve results given by the Euler method.

5.1.12 Module 13. ECM strains and displacements

After the preparations described in subsection 5.1.4 before starting the loop over MCTS, the system of linear equations to calculate ECM strains and displacements is solved every MCTS. The following steps are performed in this module:

1. Kernel that restarts forces in NOD structure. This kernel assigns one thread to one node (kernel in `cellforces.cu`).
2. Kernel that calculates forces on each node and writes them in NOD structure. This kernel assigns one thread to one node (kernel in `cellforces.cu`).
3. Kernel that copies displacements calculated on the last MCTS from NOD structure in an array u. This kernel assigns one thread to one node (kernel in `FE_nodes2dofs.cu`).
4. Kernel that copies calculated forces in an array f. This kernel assigns one thread to one node (kernel in `FE_nodes2dofs.cu`).
5. Solve $Ku = f$ system using PCG method, eq. (2.1.11).

6. Kernel that copies the recalculated u in NOD structure. This kernel assigns one thread to one node (kernel in `FE_nodes2dofs.cu`).

5.1.13 Module 14. CPM and anastomosis

At each MCTS, $(M-1)^2$ copies are proposed so the following steps need to be performed in this module (kernels in `cellmoves.cu`):

1. Generate three arrays of size $(M-1) \cdot (M-1)$ with:
    - ID of randomly selected pixels.
    - ID of random neighbors of randomly selected pixels.
    - Random float numbers between 0 and 1 used to calculate the Boltzmann probability factor in the Metropolis algorithm.
2. We divide the grid in boxes of pixels in order to compute each one in parallel. Therefore we need to know to which box each randomly selected pixel belongs. It is done by a kernel that assigns one thread to one pixel. This kernel also calculate the inertia tensor for each cell.
3. The kernel in charge of the CPM and the anastomosis assigns one thread to one box of pixels. In parallel on each box, a loop runs through each randomly selected pixel that it contains. The steps that are followed in this kernel are:
    (a) In the case of the selected pixel belongs to a expanding cell of a new sprout, check if the direction of expansion is similar to the branching direction.
    (b) Check if a cell will break in two, if necessary.
    (c) Calculate the variation of energy if the copy is made with the Hamiltonian H described in eq. (2.1.2) .

(d) Calculate the Boltzmann probability, defined in eq.(2.1.1), and check, using a random float number previously calculated, whether, according to the Metropolis rule, the copy is approved.

(e) If the copy is approved, update structures and contact_perimeter array.

(f) Check if anastomosis has occurred between two vessels and one of them becomes inactive.

5.1.14 Module 15. Update features

Every MCTS and after any change produced in the modules, we need to update the structures and arrays. For this purpose, the following steps are performed in this module (kernels in `proliferation.cu`):

1. Kernel that updates the age of cells, i.e., .age of CEL structure. This kernel assigns one thread to one cell.
2. Kernel that updates the size of cells and pixels that are closer and further to the hypoxic area of cells, i.e., .siz, .tip and .tail of CEL structure. This kernel assigns one thread to one pixel.
3. Kernel that updates the number of MCTS that a sprout has to keep its branching direction, i.e., the incubation time of our manuscript. This kernel assigns one thread to one vessel.
4. Kernel that updates types of cells and selects possible new tip cells of new sprouts. this kernel assigns one thread to one pixel.

5.1.15 Compiling, IDE, Hardware and computation time

We have used the integrated development environment Microsoft Visual Studio to edit the code, to compile multiple source files (including .cu files and CUDA libraries) and build the executable file.

The computation time of each simulation in a computer with Intel(R) Core(TM) i7-7700K CPU @4.20 GHz processor, 64.0 GB RAM and NVIDIA GeForce GTX 1080 graphics card is about 4 hours.

5.2 AMD model code

Based on AngioVCTB of the previous section, the simulation code for the angiogenesis model in retina has four main modifications with respect to the base code: calculation of VEGF concentration due to the changes in the initial-boundary value problem, activation and deactivation of VEGF sources, deactivation of the cell source module and adaptation of algorithms to the new elements (BM, RPE and drusen). Fig. 5.3 shows a flow diagram of our simulation code. The only difference with Fig. 5.1 is the replacement of the cell source module with the activation and deactivation of VEGF sources module in number 8. Each modified part of the flow diagram will be described in detail afterwards.

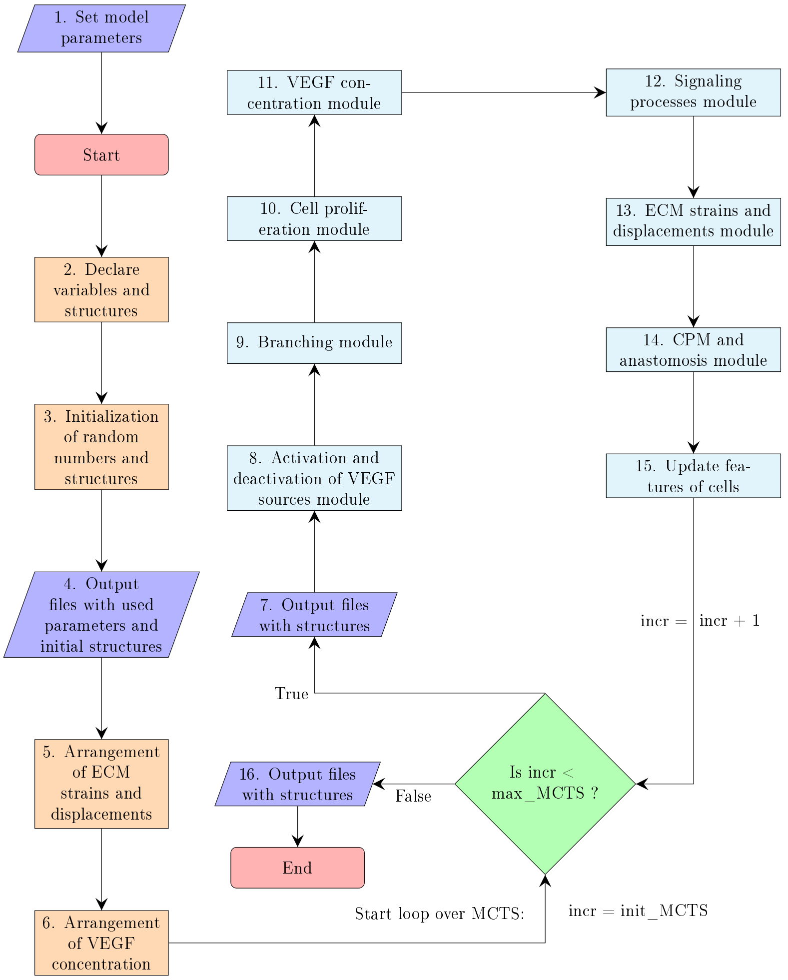

Figure 5.3: **Flow diagram of the simulation code of the angiogenesis model in retina**

5.2.1 Module 6. Arrangement of VEGF concentration

The same steps taken in section 5.1.5 need to be followed. In this case, we consider the initial-boundary value problem of eqs. (3.1.3) - (3.1.6) and it is nondimensionalized. So that we introduce the following scalings in order to nondimensionalize:

$$\tilde{C} = \frac{C}{[C]},\ \tilde{t} = \frac{t}{[t]},\ \tilde{x} = \frac{x}{[x]},\ \tilde{y} = \frac{y}{[x]},\ \tilde{G} = \frac{G}{[G]},\ \tilde{A} = \frac{A}{[A]}$$

where $[C]$, $[t]$, $[x]$, $[G]$ and $[A]$ are non-zero parameters. Substituting these new variables into the partial differential equation (PDE) (3.1.3), we obtain:

$$\frac{[C]}{[t]}\frac{\partial \tilde{C}}{\partial \tilde{t}} = \frac{D_f\,[C]}{[x]^2}\left(\frac{\partial^2 \tilde{C}}{\partial \tilde{x}^2} + \frac{\partial^2 \tilde{C}}{\partial \tilde{y}^2}\right) - \nu\,[C]\,\tilde{C} - [G]\,\tilde{G} + [A]\,\tilde{A} \;\Leftrightarrow\; \left(\text{ dividing by } \frac{D_f[C]}{[x]^2}\right)$$

$$\frac{[x]^2}{D_f\,[t]}\frac{\partial \tilde{C}}{\partial \tilde{t}} = \left(\frac{\partial^2 \tilde{C}}{\partial \tilde{x}^2} + \frac{\partial^2 \tilde{C}}{\partial \tilde{y}^2}\right) - \frac{[x]^2\,\nu}{D_f}\tilde{C} - \frac{[G]\,[x]^2}{D_f\,[C]}\tilde{G} + \frac{[A]\,[x]^2}{D_f\,[C]}\tilde{A}$$

Regarding to the cell binding and VEGF sources terms, choosing $[G] = [A] = \frac{D_f[C]}{[x]^2}$ leads to have three terms which are $\mathcal{O}(1)$, cell binding term, VEGF sources term and diffusion term, and the PDE obtained is:

$$\frac{[x]^2}{D_f\,[t]}\frac{\partial \tilde{C}}{\partial \tilde{t}} = \triangle \tilde{C} - \frac{[x]^2\,\nu}{D_f}\tilde{C} - \tilde{G} + \tilde{A}$$

The value of $\frac{[x]^2}{D_f[t]}$ and of $\frac{[x]^2\nu}{D_f}$ depend on the characteristic time scale, equal to 1 MCTS, and the characteristic length scale, on the order of the length of a side of 1 pixel. The value of $[C]$ depends on S and the value of $[G]$ and $[A]$ could be known with these data. Regarding to the equivalence between 1 MCTS and the real time units, we use the same as in the previous section

$$[t] = 1 \text{ MCTS} \simeq 0.044 \text{ h},\; [x]^2 = \left(\frac{L}{M-1}\right)^2 = \left(\frac{400\ \mu\text{m}}{400}\right)^2 = 1\ \mu\text{m}^2$$

$$[C] = 1.67 \times 10^{-7}\ \text{pg}/\mu\text{m}^2 \text{ due to the previous section, so}$$

$$[G] = [A] = \frac{D_f\,[C]}{[x]^2} = \frac{3.6 \times 10^4\ \mu\text{m}^2/\text{h} \times 1.67 \times 10^{-7}\ \text{pg}/\mu\text{m}^2}{1\ \mu\text{m}^2} = 6 \times 10^{-3}\ \text{pg}/(\mu\text{m}^2\ \text{h})$$

Therefore,

$$\frac{[x]^2}{D_f\,[t]} = \frac{1\ \mu\text{m}^2}{3.6 \times 10^4\ \mu\text{m}^2/\text{h} \times 0.044\text{h}} = 6.31 \times 10^{-4} \ll 1$$

$$\frac{[x]^2\,\nu}{D_f} = \frac{1\ \mu\text{m}^2 \times 0.6498\ \text{h}^{-1}}{3.6 \times 10^4\ \mu\text{m}^2/\text{h}} = 1.8 \times 10^{-5} \ll 1$$

The resulting factors are much less than one, so the solution of the following problem can be used to approximate the VEGF field in our model.

$$0 = \triangle \tilde{C}(\tilde{x}, \tilde{y}, \tilde{t}) - \tilde{G}(\tilde{x}, \tilde{y}, \tilde{C}) + \tilde{A}(\tilde{x}, \tilde{y}),\; (\tilde{x}, \tilde{y}) \in \Omega,\; \tilde{t} > 0$$

$$C(0,\tilde{y},\tilde{t}) = 0 = C(M-1,\tilde{y},\tilde{t}),\ C(\tilde{x},0,\tilde{t}) = 0 = C(\tilde{x},M-1,\tilde{t}),\ (\tilde{x},\tilde{y}) \in \Omega,\ \tilde{t} > 0$$

$$\mathbf{n}\cdot\nabla C(\tilde{x},\tilde{y},t) = 0,\ (\tilde{x},\tilde{y}) \in \Xi_{BM} = x_{\mathrm{h}}\times\{246,248\}\cup\{72,128,272,328\}\times[246,248],\ t>0,$$

$$C(\tilde{x},\tilde{y},0) = 0,\ (\tilde{x},\tilde{y}) \in \Omega.$$

where $x_{\mathrm{h}} = [0\ ,72]\cup[128,272]\cup[328,400]$. This equation can be solved with FDM using five-point stencil.

But, first of all and in order to simplify the notation, dimensionless parameters and functions will be used without tildes. The notation ∇^2 is more suitable for the laplacian operator. To sum up, we obtain the following Poisson problem:

$$\begin{aligned}
\text{PDE:}\quad & \nabla^2 C(x,y,t) = G(x,y,C) - A(x,y),\ 0<x<M-1,\ 0<y<M-1,\ t>0\\
\text{BC:}\quad & C(0,y,t) = 0 = C(M-1,y,t),\ 0<y<M-1,\ t>0\\
& C(x,0,t) = 0 = C(x,M-1,t),\ 0<x<M-1,\ t>0\\
& \mathbf{n}\cdot\nabla C(x,y,t) = 0,\ (x,y)\in\Xi_{BM},\ t>0,\\
\text{IC:}\quad & C(x,y,0) = 0,\ 0<x<M-1,\ 0<y<M-1.
\end{aligned} \tag{5.2.1}$$

Let C_{ij} represent an approximation to $C(x_i,y_j,t)$, where (x_i,y_j) have been described in domain section. Note that time variable is not been taken into account because the solution of the PDE of (5.2.1) on each MCTS is not time-dependent. To discretize the PDE of (5.2.1), centered finite differences have been used for $x-$ and $y-$derivatives, which gives:

$$\begin{gathered}
\tfrac{1}{h^2}\left(C_{i-1,j} - 2C_{ij} + C_{i+1,j}\right) + \tfrac{1}{h^2}\left(C_{i,j-1} - 2C_{ij} + C_{i,j+1}\right) = G_{ij} - A_{ij} \Leftrightarrow \\
\left(C_{i-1,j} + C_{i,j-1} - 4C_{ij} + C_{i+1,j} + C_{i,j+1}\right) = h^2 G_{ij} - h^2 A_{ij}
\end{gathered} \tag{5.2.2}$$

where $G_{ij} = G(x_i,y_j)$, $A_{ij} = A(x_i,y_j)$ (we know exactly G and A functions). The equation (5.2.2) changes in function of the point it is focus on and some of them have boundary conditions, so the following equations are written distinguishing each case:

- If $i=0$ and $\forall j$, or $i=M-1$ and $\forall j$, or $j=0$ and $\forall i$, or $j=M-1$ and $\forall i$,

$$C_{0j} = 0,$$

- If $i = 1$ and:
  - $j = 1$
    $$(-4C_{1,1} + C_{1,2} + C_{2,1}) = h^2 G_{1,1} - h^2 A_{1,1},$$
  - $j = M - 2$,
    $$(C_{1,M-3} - 4C_{1,M-2} + C_{2,M-2}) = h^2 G_{1,M-2} - h^2 A_{1,M-2},$$
  - $2 \leq j \leq M - 3$,
    $$(C_{1,j-1} - 4C_{1,j} + C_{1,j+1} + C_{2,j}) = h^2 G_{1,j} - h^2 A_{1,j},$$
- If $i = M - 2$ and:
  - $j = 1$
    $$(C_{M-3,1} - 4C_{M-2,1} + C_{M-2,2}) = h^2 G_{M-2,1} - h^2 A_{M-2,1},$$
  - $j = M - 2$,
    $$(C_{M-3,M-2} + C_{M-2,M-3} - 4C_{M-2,M-2}) = h^2 G_{M-2,M-2} - h^2 A_{M-2,M-2},$$
  - $2 \leq j \leq M - 3$,
    $$(C_{M-3,j} + C_{M-2,j-1} - 4C_{M-2,j} + C_{M-2,j+1}) = h^2 G_{M-2,j} - h^2 A_{M-2,j},$$
- If $j = 1$ and $2 \leq i \leq M - 3$
  $$(C_{i-1,1} - 4C_{i,1} + C_{i,2} + C_{i+1,1}) = h^2 G_{i,1} - h^2 A_{i,1},$$
- If $j = M - 2$ and $2 \leq i \leq M - 3$
  $$(C_{i-1,M-2} + C_{i,M-3} - 4C_{i,M-2} + C_{i+1,M-2}) = h^2 G_{i,M-2} - h^2 A_{i,M-2},$$
- If $j = 246$ and:

  - $i \in (0\ ,72) \cup (128, 272) \cup (328, 400)$

$$(C_{i-1,j} + 2C_{i,j-1} - 4C_{ij} + C_{i+1,j}) = h^2 G_{ij} - h^2 A_{ij},$$

  - $i = 72,\ 272$

$$(2C_{i,j-1} - 4C_{ij} + 2C_{i+1,j}) = h^2 G_{ij} - h^2 A_{ij},$$

  - $i = 128,\ 328$

$$(2C_{i-1,j} + 2C_{i,j-1} - 4C_{ij}) = h^2 G_{ij} - h^2 A_{ij},$$

- If $j = 248$ and:

  - $i \in (0,\ 72) \cup (128,\ 272) \cup (328,\ 400)$

$$(C_{i-1,j} - 4C_{ij} + 2C_{i,j+1} + C_{i+1,j}) = h^2 G_{ij} - h^2 A_{ij},$$

  - $i = 72,\ 272$

$$(-4C_{ij} + 2C_{i,j+1} + 2C_{i+1,j}) = h^2 G_{ij} - h^2 A_{ij},$$

  - $i = 128,\ 328$

$$(2C_{i-1,j} - 4C_{ij} + 2C_{i,j+1}) = h^2 G_{ij} - h^2 A_{ij},$$

- If $i = 72,\ 272$ and $j \in (246,\ 248)$,

$$(C_{i,j-1} - 4C_{ij} + C_{i,j+1} + 2C_{i+1,j}) = h^2 G_{ij} - h^2 A_{ij},$$

- If $i = 128,\ 328$ and $j \in (246,\ 248)$,

$$(2C_{i-1,j} + C_{i,j-1} - 4C_{ij} + C_{i,j+1}) = h^2 G_{ij} - h^2 A_{ij},$$

- If $2 \le i \le M - 3$ and $2 \le j \le M - 3$,

$$(C_{i-1,j} + C_{i,j-1} - 4C_{ij} + C_{i,j+1} + C_{i+1,j}) = h^2 G_{ij} - h^2 A_{ij},$$

The above equations can be collected together into a matrix equation $Qx = R$. Q is a matrix of size N_{FD}^2, with $N_{FD} = (M-2)^2$ that contains the factors that appear multiplying C_{ij} terms. x is an array of size N_{FD} that contains the values for C_{ij} terms that satisfy the matrix form equation. The first time we calculate x, it is initialized at zero, but in future Monte Carlo time steps we use the solution calculated in the previous MCTS. R is an array of size N_{FD} and it is formed by the right - hand side of the previous equations.

Q is a sparse matrix so the system is needed to be solved with an appropriate method, like the PCG method using ILU decomposition. The algorithm is provided by CUDA and uses a CSR format, so we have decomposed Q into three arrays:

- $Qval$ is an array of size $nz_{FD} = 5(N_{FD} - ((248-1)-246)\sqrt{N_{FD}} - (128-72) - 1 - (328-272) - 1)) - 4\sqrt{N_{FD}} - 2\sqrt{N_{FD}} - (128-72) + 1 - (328-272) + 1) - 4(248-246+1) + 2((248-1)-246)$ is the number of non zero values of Q, i.e. five - point finite difference scheme minus number of frontier nodes per boundary times number of boundaries. This array contains the non zero values of matrix Q.
- $Qcol$ is an array of size nz_{FD}. It contains the index of the column of corresponding nonzero value written in $Qval$.
- $Qrow$ is an array of size $N_{FD}+1$. It contains the cumulative number of non-zero values in rows of Q, starting with 0 in the first gap.

These three arrays, plus x and R, are needed to use the mentioned algorithm. After that, the x array is included in a bigger one V, which also contains the values of VEGF concentration at the boundaries. Thus, the following steps are performed in this module:

1. Initialize x and R.
2. Define Q matrix in CSR format.

3. Prepare CUBLAS and CUSPARSE data:
    (a) Create CUBLAS context.
    (b) Create CUSPARSE context.
    (c) Description of the Q matrix.
    (d) Define the properties of the matrix.
    (e) Create the analysis info object for the Q matrix.
    (f) Perform the analysis for the Non-Transpose case.
    (g) Copy Q data to ILU0 vals as input.
    (h) Generate the Incomplete LU factor H for the matrix Q using cudsparseScsrilu0.
    (i) Create info objects for the ILU0 preconditioner.
4. Solve $Qx = R$ system using PCG method.
5. Include array x in V. This takes place in a kernel where is assigned one thread to one node (kernel in `chemotaxis.cu`).
6. Associate to each cell the value of VEGF concentration on the bottom left grid point of the pixel selected in .tip of CEL structure, i.e., update .vegf of CEL structure. This takes place in a kernel where is assigned one thread to one cell (kernel in `chemotaxis.cu`).

The description of *Module 11. VEGF concentration* of section 5.1.10 is also correct for this model taking into account that the right - hand side, R, has changed.

5.2.2 Module 8. Activation and deactivation of VEGF sources

Due to the retinal configuration and onset of angiogenesis in this model, the cell source module is not required. Instead, we need a module that regulates the activation and deactivation of VEGF sources, i.e., the term $A(x, y)$ of eq. (3.1.3).

As it is described in section 3.1 and eq. (3.1.8), VEGF sources associated with each druse are activated when it reaches a certain size. This condition is checked with an *if* statement for each druse and if it is met, the right - hand side R of the previous section, i.e., the term $A(x, y)$ of eq. (3.1.3), is modified and the druse produces a hole in the Bruch's membrane.

Once the VEGF sources are activated, the sources associated to drusen could be deactivated if a sprout arrives near them. The proximity of sprouts near the drusen is checked using the library Thrust to be able to look at the position of every cell in parallel. If a cell is close enough to a druse, the right - hand side R of the previous section, i.e., the term $A(x, y)$ of eq. (3.1.3), is modified and the VEGF source of this druse deactivated.

5.2.3 Module 14. CPM and anastomosis

Essentially, the development of this module is the same as that described in section 5.1.13. In the code, the incorporation of new elements to the model only modifies some conditional statements in order to check the element. In this sense, the module where the CPM is carried out is the most affected module, however the rest of the modules are also affected.

5.3 Lumen formation model code

The simulation codes of both models presented in chapter 4 are based on AngioVCTB [125] of section 5.1. However, the simulation code of the cell and cord hollowing model is simple due to the fact that the model is applied on an already developed sprout and the main new additions have been described in section 4.1. For these reasons, the simulation code of inverse blebbing model is the only one that will be described in this section.

Fig. 5.4 shows a flow diagram of our simulation code for the inverse blebbing model. The only differences with Fig. 5.1 are the replacement of the cell source module with the definition of forces related to blood pressure module in number 8 and the module of branching and anastomosis that are not considered in this model. In addition to the new module, small modifications have been carried out in more modules, which will be detailed afterwards too.

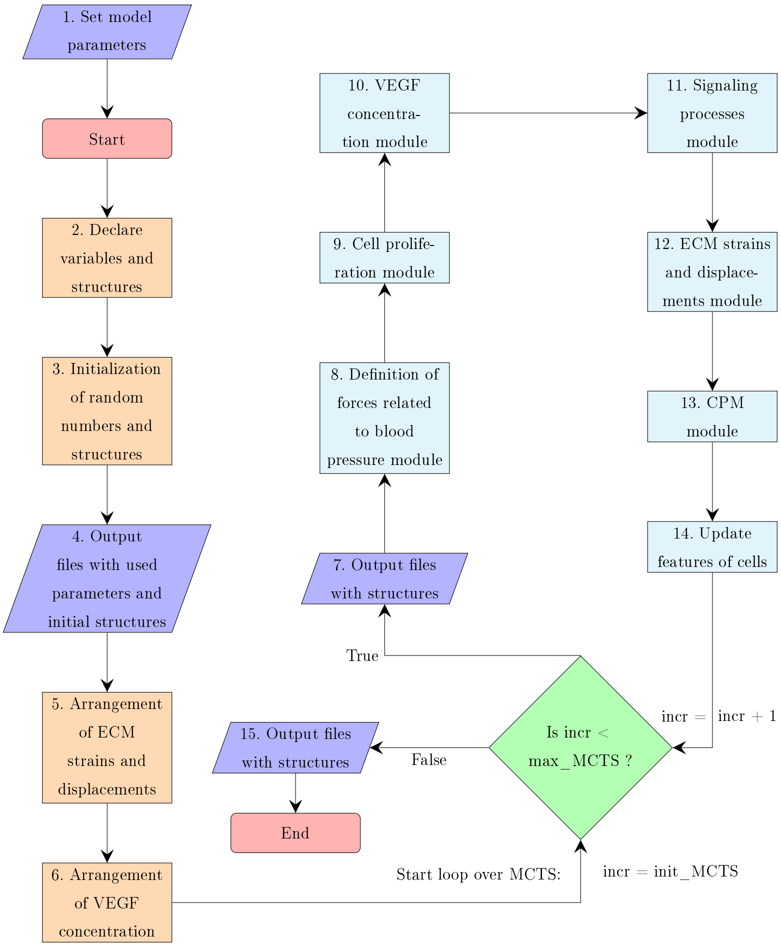

Figure 5.4: **Flow diagram of the simulation code of the inverse blebbing model for lumen formation**

5.3.1 Module 2. Declare variables and structures

The assignment of ECs to the sides needs to be stored in some structures as well as the forces related to the blood pressure. Therefore, new members have been incorporated to the following C-structures:

- VOX: it has a new member, .sid, that is an array with the ID of occupying side, 0 if no side.
- NOD: it has two new members, .flx and .fly. They are the x and y component of the force exerted by blood pressure in the corresponding node.
- CEL: it has a new member, .sid, that is an array with the ID of cell's side, 0 if no side.
- VES: there are two members of the structure that store the ID of the proliferating cell, one per side, .proltags1 and .proltags2. Additionally, .ns1, .ns2 store the number of ECs per side.

The output files of this simulation code also store the new elements.

5.3.2 Module 8. Definition of forces related to blood pressure

Definition of forces related to blood pressure, described in a subsection of 4.2, is implemented in this module. Therefore, the following steps are performed:

1. Kernel that builds the arrays $\mathbf{v}_s^i$ with $i = 1, 2$. This array contains the ID of the pixels in the side i that have boundary with the pixels in the side j with $j \neq i$. This kernel assigns one thread to one node.
2. Functions of library Thrust prepares data arrays for K-means algorithm. The two arrays with the pixels to classify, one per side, and the two arrays of centroids. The preparation includes to have two elements per pixel in these four arrays: position (i, j) of the pixel $\mathbf{x}$ in the square grid.

3. K-means algorithm is used once per side. This algorithm forms clusters of pixels of side i with $i = 1, 2$ that are associated to the elements of $\mathbf{v}_s^j$ with $j \neq i$. The number of clusters is equal to the length of $\mathbf{v}_s^j$. Since the centroids should not change, the number of iterations of the K-means algorithm is one.

4. Kernel that calculates the forces on each node using the equation (4.2.4). This kernel is executed once per side and considers the clusters and centroids resulting of the K-means algorithm as well as the position of the tip of the sprout. This kernel assigns one thread to one pixel of one side.

5.3.3 Module 9. Cell proliferation

Cell proliferation module is developed mainly as described in section 5.1.9 of AngioVCTB simulation code. As discussed in section 4.2, the difference is the consideration of two proliferating cells per sprout, one per side. Thereby, the kernels that prepare the arrays and conditions to use the K-means algorithm have been adapted to check two cells per sprout and the threads are assigned one to each side of the sprout.

Chapter 6

Conclusions and future work

The motivation for this thesis is as simple as it is challenging: understanding the underlying mechanisms of angiogenesis and finding the key to convert pathological angiogenesis in physiological angiogenesis. The development of cellular dynamics models of angiogenesis that permit exploration of the relative importance of mechanical, chemical and cellular cues is essential for these purposes. This goal cannot be pursued without the review of important biological notions and the mathematical models developed to date given in chapter 1.

In chapter 2, based on our paper [125], we present a mathematical model of early stage angiogenesis that is able to explore the role of biochemical signaling and tissue mechanics. We use a CPM that incorporates cell motion following increasing gradients of VEGF (chemotaxis), of adhesion to substrate (haptotaxis) and of substrate stiffness (durotaxis), as well as a model of cell splitting and proliferation that uses an unsupervised machine learning algorithm, and the Notch signaling pathway. This model is used to unravel the regulating role of Jagged, Notch and Delta dynamics in vascular cells. These membrane proteins have an important part in determining the leading cell in each neovascular sprout and also in branching, anastomosis and speed of angiogenesis.

Simulations of this model show that although anastomosis is driven by chemotaxis, it may be favored or impeded depending on the mechanical configuration of the strains near the tip cells. Regarding to the Notch signaling pathway, we have found that increasing the production rate of Jagged produce a thinner vasculature that advances faster due to the larger number of cells with hybrid phenotype. On the other hand, increasing the production rate of Delta lowers the number of tip cells therefore there are less sprouts and anastomosis is less frequent. Quantitative results have confirmed that an imbalance of the Jagged production results in pathological angiogenesis that can be corrected by increasing the Delta production rate to diminish the number of tips and slow down somewhat angiogenesis. These results have been obtained for two types of cell dynamics: rounder and insensitive to chemical and mechanical cues stalk cells and more elongate and motile stalk cells.

The following chapter is focused on the angiogenesis in the retina. The model presented here is an adaptation of the model described above. Multiple sources of VEGF and new elements are considered to analyze their effects on the choroidal neovascularization taking place in wet age-related macular degeneration. Our results confirm the widely studied relationship between adhesion and type of CNV. Impaired lateral adhesion between the Bruch's membrane and RPE cells, between RPE cells themselves or endothelial cells themselves determine the formation and type of CNV. It is also known that high levels of VEGF concentration are needed for angiogenesis to begin. However, we also find that the level of VEGF concentration at the point where a sprout may cross the RPE layer to the subretinal space is decisive to be able to cross. We also discover an extraordinary relationship between Notch signaling and AMD. Reducing the production rate of Jagged in a subretinal CNV decreases the number of blood vessel in this area and slows the speed of angiogenesis. Finally, we are able to recognize the CNV type that develops during AMD looking and some Notch signaling proteins that work as markers.

After chapter 3, chapter 4 introduces two models of lumen formation. Simulations of the first model exhibit the need to incorporate the blood pressure in a model of lumen formation in angiogenesis. The second and promising model is a work in progress, but the preliminary results show the capacity of the endothelial cells to rearrange and form the lumen in a sprout using the mechanism of inverse blebbing.

An essential part of this thesis is the implementation of the simulation codes for these models. It has been necessary to face the complexity of carrying out a GPU-based parallel implementation in order to obtain the previous results. Paralleling the codes of the multiple biological processes models over cells, nodes or pixels is fundamental to be able to get simulations of multiple sprouts in an achievable computational time. Chapter 5 is devoted to the explanation of the simulation codes.

Despite all of the work developed in this thesis, a complete understanding of the mechanisms involved in angiogenesis and how to control it is far from being achieved. Some suggestions about how to improve models of chapters 2 and 3 have been made in the corresponding chapters. However we overview them again and add some extra comments in the next paragraphs.

Our 2D model of early stage angiogenesis of chapter 2 needs to be extended in several directions to be made more realistic. A later stage of angiogenesis, the lumen formation, has been considered in chapter 4 in order to improve the model. However, this work is still in progress and it needs to be extended to more than one sprout. Modeling how the lumen continues connected in a branching point will be a challenge. Including this functional lumen formation model to the model of angiogenesis in the retina would be the next step. In that way, an investigation about how a poor lumen formation affects the leaking of blood in the retina may be interesting.

The extension of these models to three dimensional configurations is straightforward although it requires more computing power. The used architecture CUDA is ready for 3D simulations, but the number of threads to use would be much higher so more GPUs would be needed. Moreover, some biological processes that we have included in the models would be challenging to describe in 3D due to the fact that most of the available images from experiments are 2D.

While we have studied relatively short distances between the primary vessel and the target hypoxic region or between the choroid and the photoreceptor cells, we need to consider larger systems to be able to do statistical studies of vessel numbers and their width. This study may be appropriate to learn more about the vascular plexus developed in the simulations and their morphology.

Bibliography

[1] SEOM, “Las cífras del cáncer en españa 2020,” tech. rep., Sociedad Española de Oncología Médica, 2020.

[2] P. Carmeliet, “Angiogenesis in health and disease,” *Nature Medicine*, vol. 9, pp. 653–660, jun 2003.

[3] W. L. Wong, X. Su, X. Li, C. M. G. Cheung, R. Klein, C.-Y. Cheng, and T. Y. Wong, “Global prevalence of age-related macular degeneration and disease burden projection for 2020 and 2040: a systematic review and meta-analysis,” *The Lancet Global Health*, vol. 2, pp. e106–e116, feb 2014.

[4] J. B. Jonas, “Global prevalence of age-related macular degeneration,” *The Lancet Global Health*, vol. 2, pp. e65–e66, feb 2014.

[5] J. Hunter, *The Works of John Hunter, F.R.S. with Notes.* 1835.

[6] A. T. Hertig, *Angiogenesis in the early human chorion and in the primary placenta of the macaque monkey.* 1935.

[7] L. M. Sherwood, E. E. Parris, and J. Folkman, “Tumor angiogenesis: Therapeutic implications,” *New England Journal of Medicine*, vol. 285, pp. 1182–1186, nov 1971.

[8] N. Ferrara, H.-P. Gerber, and J. LeCouter, “The biology of VEGF and its receptors,” *Nature Medicine*, vol. 9, pp. 669–676, jun 2003.

[9] T. T. Chen, A. Luque, S. Lee, S. M. Anderson, T. Segura, and M. L. Iruela-Arispe, "Anchorage of VEGF to the extracellular matrix conveys differential signaling responses to endothelial cells," *Journal of Cell Biology*, vol. 188, pp. 595–609, feb 2010.

[10] K. Bentley, H. Gerhardt, and P. A. Bates, "Agent-based simulation of notch-mediated tip cell selection in angiogenic sprout initialisation," *Journal of Theoretical Biology*, vol. 250, pp. 25–36, jan 2008.

[11] H. Gerhardt, M. Golding, M. Fruttiger, C. Ruhrberg, A. Lundkvist, A. Abramsson, M. Jeltsch, C. Mitchell, K. Alitalo, D. Shima, and C. Betsholtz, "VEGF guides angiogenic sprouting utilizing endothelial tip cell filopodia," *Journal of Cell Biology*, vol. 161, pp. 1163–1177, jun 2003.

[12] M. Hellström, L.-K. Phng, J. J. Hofmann, E. Wallgard, L. Coultas, P. Lindblom, J. Alva, A.-K. Nilsson, L. Karlsson, N. Gaiano, K. Yoon, J. Rossant, M. L. Iruela-Arispe, M. Kalén, H. Gerhardt, and C. Betsholtz, "Dll4 signalling through notch1 regulates formation of tip cells during angiogenesis," *Nature*, vol. 445, pp. 776–780, jan 2007.

[13] G. T. Meyer, L. J. Matthias, L. Noack, M. A. Vadas, and J. R. Gamble, "Lumen formation during angiogenesis in vitro involves phagocytic activity, formation and secretion of vacuoles, cell death, and capillary tube remodelling by different populations of endothelial cells," *The Anatomical Record*, vol. 249, pp. 327–340, nov 1997.

[14] B. Lubarsky and M. A. Krasnow, "Tube morphogenesis," *Cell*, vol. 112, pp. 19–28, jan 2003.

[15] M. L. Iruela-Arispe and G. E. Davis, "Cellular and molecular mechanisms of vascular lumen formation," *Developmental Cell*, vol. 16, pp. 222–231, feb 2009.

[16] V. Gebala, R. Collins, I. Geudens, L.-K. Phng, and H. Gerhardt, “Blood flow drives lumen formation by inverse membrane blebbing during angiogenesis in vivo,” *Nature Cell Biology*, vol. 18, pp. 443–450, feb 2016.

[17] S. E. M. Boas and R. M. H. Merks, “Synergy of cell–cell repulsion and vacuolation in a computational model of lumen formation,” *Journal of The Royal Society Interface*, vol. 11, p. 20131049, mar 2014.

[18] M. Moreira-Soares, R. Coimbra, L. Rebelo, J. Carvalho, and R. D. M. Travasso, “Angiogenic factors produced by hypoxic cells are a leading driver of anastomoses in sprouting angiogenesis–a computational study,” *Scientific Reports*, vol. 8, p. 8726, jun 2018.

[19] A. Fantin, J. M. Vieira, G. Gestri, L. Denti, Q. Schwarz, S. Prykhozhij, F. Peri, S. W. Wilson, and C. Ruhrberg, “Tissue macrophages act as cellular chaperones for vascular anastomosis downstream of VEGF-mediated endothelial tip cell induction,” *Blood*, vol. 116, pp. 829–840, aug 2010.

[20] K. Zhan, L. Bai, and J. Xu, “Role of vascular endothelial progenitor cells in construction of new vascular loop,” *Microvascular Research*, vol. 90, pp. 1–11, nov 2013.

[21] I. Geudens and H. Gerhardt, “Coordinating cell behaviour during blood vessel formation,” *Development*, vol. 138, pp. 4569–4583, sep 2011.

[22] J. Flores, A. M. Romero, R. D. Travasso, and E. C. Poiré, “Flow and anastomosis in vascular networks,” *Journal of Theoretical Biology*, vol. 317, pp. 257–270, jan 2013.

[23] C. A. Franco, M. L. Jones, M. O. Bernabeu, I. Geudens, T. Mathivet, A. Rosa, F. M. Lopes, A. P. Lima, A. Ragab, R. T. Collins, L.-K. Phng, P. V. Coveney, and H. Gerhardt, “Dynamic endothelial cell rearrangements drive developmental vessel regression,” *PLOS Biology*, vol. 13, p. e1002125, apr 2015.

[24] M. O. Bernabeu, M. L. Jones, R. W. Nash, A. Pezzarossa, P. V. Coveney, H. Gerhardt, and C. A. Franco, “PolNet: A tool to quantify network-level cell polarity and blood flow in vascular remodeling,” *Biophysical Journal*, vol. 114, pp. 2052–2058, may 2018.

[25] A. Szymborska and H. Gerhardt, “Hold me, but not too tight—endothelial cell–cell junctions in angiogenesis,” *Cold Spring Harbor Perspectives in Biology*, vol. 10, p. a029223, aug 2018.

[26] C.-M. Lo, H.-B. Wang, M. Dembo, and Y. li Wang, “Cell movement is guided by the rigidity of the substrate,” *Biophysical Journal*, vol. 79, pp. 144–152, jul 2000.

[27] I. B. Lobov, R. A. Renard, N. Papadopoulos, N. W. Gale, G. Thurston, G. D. Yancopoulos, and S. J. Wiegand, “Delta-like ligand 4 (dll4) is induced by VEGF as a negative regulator of angiogenic sprouting,” *Proceedings of the National Academy of Sciences*, vol. 104, pp. 3219–3224, feb 2007.

[28] L.-K. Phng and H. Gerhardt, “Angiogenesis: A team effort coordinated by notch,” *Developmental Cell*, vol. 16, pp. 196–208, feb 2009.

[29] P. Santos-Oliveira, A. Correia, T. Rodrigues, T. M. Ribeiro-Rodrigues, P. Matafome, J. C. Rodríguez-Manzaneque, R. Seiça, H. Girão, and R. D. M. Travasso, “The force at the tip - modelling tension and proliferation in sprouting angiogenesis,” *PLOS Computational Biology*, vol. 11, p. e1004436, aug 2015.

[30] L. Jakobsson, C. A. Franco, K. Bentley, R. T. Collins, B. Ponsioen, I. M. Aspalter, I. Rosewell, M. Busse, G. Thurston, A. Medvinsky, S. Schulte-Merker, and H. Gerhardt, “Endothelial cells dynamically compete for the tip cell position during angiogenic sprouting,” *Nature Cell Biology*, vol. 12, pp. 943–953, sep 2010.

[31] S. Arima, K. Nishiyama, T. Ko, Y. Arima, Y. Hakozaki, K. Sugihara, H. Koseki, Y. Uchijima, Y. Kurihara, and H. Kurihara, "Angiogenic morphogenesis driven by dynamic and heterogeneous collective endothelial cell movement," *Development*, vol. 138, pp. 4763–4776, sep 2011.

[32] B. Cruys, B. W. Wong, A. Kuchnio, D. Verdegem, A. R. Cantelmo, L.-C. Conradi, S. Vandekeere, A. Bouché, I. Cornelissen, S. Vinckier, R. M. H. Merks, E. Dejana, H. Gerhardt, M. Dewerchin, K. Bentley, and P. Carmeliet, "Glycolytic regulation of cell rearrangement in angiogenesis," *Nature Communications*, vol. 7, jul 2016.

[33] A. R. Cantelmo, L.-C. Conradi, A. Brajic, J. Goveia, J. Kalucka, A. Pircher, P. Chaturvedi, J. Hol, B. Thienpont, L.-A. Teuwen, S. Schoors, B. Boeckx, J. Vriens, A. Kuchnio, K. Veys, B. Cruys, L. Finotto, L. Treps, T. E. Stav-Noraas, F. Bifari, P. Stapor, I. Decimo, K. Kampen, K. D. Bock, G. Haraldsen, L. Schoonjans, T. Rabelink, G. Eelen, B. Ghesquière, J. Rehman, D. Lambrechts, A. B. Malik, M. Dewerchin, and P. Carmeliet, "Inhibition of the glycolytic activator PFKFB3 in endothelium induces tumor vessel normalization, impairs metastasis, and improves chemotherapy," *Cancer Cell*, vol. 30, pp. 968–985, dec 2016.

[34] L.-C. Conradi, A. Brajic, A. R. Cantelmo, A. Bouché, J. Kalucka, A. Pircher, U. Brüning, L.-A. Teuwen, S. Vinckier, B. Ghesquiére, M. Dewerchin, and P. Carmeliet, "Tumor vessel disintegration by maximum tolerable PFKFB3 blockade," *Angiogenesis*, vol. 20, pp. 599–613, sep 2017.

[35] A. R. Cantelmo, A. Pircher, J. Kalucka, and P. Carmeliet, "Vessel pruning or healing: endothelial metabolism as a novel target?," *Expert Opinion on Therapeutic Targets*, vol. 21, pp. 239–247, jan 2017.

[36] H. M. Eilken and R. H. Adams, "Dynamics of endothelial cell behavior in sprouting angiogenesis," *Current Opinion in Cell Biology*, vol. 22, pp. 617–625, oct 2010.

[37] K. Bentley, C. A. Franco, A. Philippides, R. Blanco, M. Dierkes, V. Gebala, F. Stanchi, M. Jones, I. M. Aspalter, G. Cagna, S. Weström, L. Claesson-Welsh, D. Vestweber, and H. Gerhardt, "The role of differential VE-cadherin dynamics in cell rearrangement during angiogenesis," *Nature Cell Biology*, vol. 16, pp. 309–321, mar 2014.

[38] C. M. Warren and M. L. Iruela-Arispe, "Signaling circuitry in vascular morphogenesis," *Current Opinion in Hematology*, p. 1, mar 2010.

[39] B. Ubezio, R. A. Blanco, I. Geudens, F. Stanchi, T. Mathivet, M. L. Jones, A. Ragab, K. Bentley, and H. Gerhardt, "Synchronization of endothelial dll4-notch dynamics switch blood vessels from branching to expansion," *eLife*, vol. 5, apr 2016.

[40] R. Benedito, C. Roca, I. Sörensen, S. Adams, A. Gossler, M. Fruttiger, and R. H. Adams, "The notch ligands dll4 and jagged1 have opposing effects on angiogenesis," *Cell*, vol. 137, pp. 1124–1135, jun 2009.

[41] J. J. Hofmann and M. L. Iruela-Arispe, "Notch expression patterns in the retina: An eye on receptor–ligand distribution during angiogenesis," *Gene Expression Patterns*, vol. 7, pp. 461–470, feb 2007.

[42] M. Sjöqvist and E. R. Andersson, "Do as i say, not(ch) as i do: Lateral control of cell fate," *Developmental Biology*, vol. 447, pp. 58–70, mar 2017.

[43] J. Folkman, "Angiogenesis in cancer, vascular, rheumatoid and other disease," *Nature Medicine*, vol. 1, pp. 27–30, jan 1995.

[44] P. Carmeliet, "Angiogenesis in life, disease and medicine," *Nature*, vol. 438, pp. 932–936, dec 2005.

[45] M. G. Tonnesen, X. Feng, and R. A. Clark, "Angiogenesis in wound healing," *Journal of Investigative Dermatology Symposium Proceedings*, vol. 5, pp. 40–46, dec 2000.

[46] J. R. Jackson, M. P. Seed, C. H. Kircher, D. A. Willoughby, and J. D. Winkler, “The codependence of angiogenesis and chronic inflammation,” *The FASEB Journal*, vol. 11, pp. 457–465, may 1997.

[47] D. Liao and R. S. Johnson, “Hypoxia: A key regulator of angiogenesis in cancer,” *Cancer and Metastasis Reviews*, vol. 26, pp. 281–290, jun 2007.

[48] I. J. Fidler, “Angiogenesis and cancer metastasis.,” *Cancer journal (Sudbury, Mass.)*, vol. 6 Suppl 2, pp. S134–S141, Apr. 2000.

[49] P. Carmeliet and R. K. Jain, “Angiogenesis in cancer and other diseases,” *Nature*, vol. 407, pp. 249–257, sep 2000.

[50] I. Zuazo-Gaztelu and O. Casanovas, “Unraveling the role of angiogenesis in cancer ecosystems,” *Frontiers in Oncology*, vol. 8, jul 2018.

[51] C. R. V. A. Maruotti N, Cantatore F and R. D, “Angiogenesis in rheumatoid arthritis,” *Histol. Histopathol*, vol. 21, pp. 557–566, 2006.

[52] R. N. Taylor, J. Yu, P. B. Torres, A. C. Schickedanz, J. K. Park, M. D. Mueller, and N. Sidell, “Mechanistic and therapeutic implications of angiogenesis in endometriosis,” *Reproductive Sciences*, vol. 16, pp. 140–146, feb 2009.

[53] M. Laschke and M. Menger, “Anti-angiogenic treatment strategies for the therapy of endometriosis,” *Human Reproduction Update*, vol. 18, pp. 682–702, jun 2012.

[54] A. Martin, M. R. Komada, and D. C. Sane, “Abnormal angiogenesis in diabetes mellitus,” *Medicinal Research Reviews*, vol. 23, pp. 117–145, mar 2003.

[55] R. D. Jager, W. F. Mieler, and J. W. Miller, “Age-related macular degeneration,” *New England Journal of Medicine*, vol. 358, pp. 2606–2617, jun 2008.

[56] L. Nivison-Smith, R. Milston, M. Madigan, and M. Kalloniatis, “Age-related macular degeneration,” *Optometry and Vision Science*, vol. 91, pp. 832–848, aug 2014.

[57] V. Manjunath, M. Taha, J. G. Fujimoto, and J. S. Duker, “Choroidal thickness in normal eyes measured using cirrus HD optical coherence tomography,” *American Journal of Ophthalmology*, vol. 150, pp. 325–329.e1, sep 2010.

[58] M. L. G. Coscas and F. Coscas, *Atlas of OCT: Angiography in AMD. Comparison with multimodal imaging.* Societé Francaise de Retine, 2015.

[59] T. Laforest, M. Künzi, L. Kowalczuk, D. Carpentras, F. Behar-Cohen, and C. Moser, “Transscleral optical phase imaging of the human retina,” *Nature Photonics*, vol. 14, pp. 439–445, mar 2020.

[60] R. F. Gariano and T. W. Gardner, “Retinal angiogenesis in development and disease,” *Nature*, vol. 438, pp. 960–966, dec 2005.

[61] M. Fruttiger, “Development of the retinal vasculature,” *Angiogenesis*, vol. 10, pp. 77–88, feb 2007.

[62] A. Scott, M. B. Powner, P. Gandhi, C. Clarkin, D. H. Gutmann, R. S. Johnson, N. Ferrara, and M. Fruttiger, “Astrocyte-derived vascular endothelial growth factor stabilizes vessels in the developing retinal vasculature,” *PLoS ONE*, vol. 5, p. e11863, jul 2010.

[63] S. Selvam, T. Kumar, and M. Fruttiger, “Retinal vasculature development in health and disease,” *Progress in Retinal and Eye Research*, vol. 63, pp. 1–19, mar 2018.

[64] P. Mammadzada, P. M. Corredoira, and H. André, “The role of hypoxia-inducible factors in neovascular age-related macular degeneration: a gene therapy perspective,” *Cellular and Molecular Life Sciences*, vol. 77, pp. 819–833, dec 2020.

[65] K. M. Gehrs, D. H. Anderson, L. V. Johnson, and G. S. Hageman, “Age-related macular degeneration—emerging pathogenetic and therapeutic concepts,” *Annals of Medicine*, vol. 38, pp. 450–471, jan 2006.

[66] E. Ellertsdóttir, A. Lenard, Y. Blum, A. Krudewig, L. Herwig, M. Affolter, and H.-G. Belting, "Vascular morphogenesis in the zebrafish embryo," *Developmental Biology*, vol. 341, pp. 56–65, may 2010.

[67] A. Schuermann, C. S. Helker, and W. Herzog, "Angiogenesis in zebrafish," *Seminars in Cell & Developmental Biology*, vol. 31, pp. 106–114, jul 2014.

[68] L. L. Bonilla, M. Carretero, and F. Terragni, "Stochastic models of blood vessel growth," in *Stochastic Dynamics Out of Equilibrium*, pp. 413–436, Springer International Publishing, 2019.

[69] C. L. Stokes and D. A. Lauffenburger, "Analysis of the roles of microvessel endothelial cell random motility and chemotaxis in angiogenesis," *Journal of Theoretical Biology*, vol. 152, pp. 377–403, oct 1991.

[70] C. L. Stokes, D. A. Lauffenburger, and S. K. Williams, "Migration of individual microvessel endothelial cells: stochastic model and parameter measurement.," *Journal of cell science*, vol. 99 (Pt 2), pp. 419–430, June 1991.

[71] L. L. Bonilla, M. Carretero, and F. Terragni, "Integrodifference master equation describing actively growing blood vessels in angiogenesis," *International Journal of Nonlinear Science and Numerical Simulation*, 2020.

[72] M. Plank, B. Sleeman, and P. Jones, "The role of the angiopoietins in tumour angiogenesis," *Growth Factors*, vol. 22, pp. 1–11, mar 2004.

[73] S. Tong and F. Yuan, "Numerical simulations of angiogenesis in the cornea," *Microvascular Research*, vol. 61, pp. 14–27, jan 2001.

[74] M. R. Owen, T. Alarcón, P. K. Maini, and H. M. Byrne, "Angiogenesis and vascular remodelling in normal and cancerous tissues," *Journal of Mathematical Biology*, vol. 58, pp. 689 – 721, 2009.

[75] F. Milde, M. Bergdorf, and P. Koumoutsakos, "A hybrid model for three-dimensional simulations of sprouting angiogenesis," *Biophysical Journal*, vol. 95, pp. 3146–3160, oct 2008.

[76] V. Capasso and D. Morale, "Stochastic modelling of tumour-induced angiogenesis," *Journal of Mathematical Biology*, vol. 58, pp. 219–233, jun 2008.

[77] L. L. Bonilla, V. Capasso, M. Alvaro, and M. Carretero, "Hybrid modeling of tumor-induced angiogenesis," *Physical Review E*, vol. 90, no. 6, p. 062716, 2014.

[78] F. Terragni, M. Carretero, V. Capasso, and L. L. Bonilla, "Stochastic model of tumor-induced angiogenesis: Ensemble averages and deterministic equations," *Physical Review E*, vol. 93, p. 022413, feb 2016.

[79] L. L. Bonilla, M. Carretero, F. Terragni, and B. Birnir, "Soliton driven angiogenesis," *Scientific Reports*, vol. 6, p. 31296, aug 2016.

[80] L. L. Bonilla, M. Carretero, and F. Terragni, "Solitonlike attractor for blood vessel tip density in angiogenesis," *Physical Review E*, vol. 94, p. 062415, dec 2016.

[81] L. L. Bonilla, V. Capasso, M. Alvaro, M. Carretero, and F. Terragni, "On the mathematical modelling of tumor-induced angiogenesis," *Mathematical Biosciences and Engineering*, vol. 14, no. 1, pp. 45–66, 2017.

[82] R. D. Travasso, M. Castro, and J. C. Oliveira, "The phase-field model in tumor growth," *Philosophical Magazine*, vol. 91, pp. 183–206, jan 2011.

[83] R. D. M. Travasso, E. C. Poiré, M. Castro, J. C. Rodrguez-Manzaneque, and A. Hernández-Machado, "Tumor angiogenesis and vascular patterning: A mathematical model," *PLoS ONE*, vol. 6, p. e19989, may 2011.

[84] G. Vilanova, I. Colominas, and H. Gomez, "Coupling of discrete random walks and continuous modeling for three-dimensional tumor-induced angiogenesis," *Computational Mechanics*, vol. 53, pp. 449–464, dec 2014.

[85] G. Vilanova, I. Colominas, and H. Gomez, "Computational modeling of tumor-induced angiogenesis," *Archives of Computational Methods in Engineering*, vol. 24, pp. 1071–1102, jan 2017.

[86] A. M. T. Rojas, A. M. Romero, I. Pagonabarraga, R. D. M. Travasso, and E. C. Poiré, "Obstructions in vascular networks: Relation between network morphology and blood supply," *PLOS ONE*, vol. 10, p. e0128111, jun 2015.

[87] T. Heck, M. M. Vaeyens, and H. V. Oosterwyck, "Computational models of sprouting angiogenesis and cell migration: Towards multiscale mechanochemical models of angiogenesis," *Mathematical Modelling of Natural Phenomena*, vol. 10, no. 1, pp. 108–141, 2015.

[88] F. Graner and J. A. Glazier, "Simulation of biological cell sorting using a two-dimensional extended potts model," *Physical Review Letters*, vol. 69, pp. 2013–2016, sep 1992.

[89] N. Chen, J. A. Glazier, J. A. Izaguirre, and M. S. Alber, "A parallel implementation of the cellular potts model for simulation of cell-based morphogenesis," *Computer Physics Communications*, vol. 176, pp. 670–681, jun 2007.

[90] A. L. Bauer, T. L. Jackson, and Y. Jiang, "A cell-based model exhibiting branching and anastomosis during tumor-induced angiogenesis," *Biophysical Journal*, vol. 92, pp. 3105–3121, may 2007.

[91] A. W. Mahoney, B. G. Smith, N. S. Flann, and G. J. Podgorski, "Discovering novel cancer therapies: A computational modeling and search approach," in *2008 IEEE Symposium on Computational Intelligence in Bioinformatics and Computational Biology*, IEEE, sep 2008.

[92] R. F. M. van Oers, E. G. Rens, D. J. LaValley, C. A. Reinhart-King, and R. M. H. Merks, “Mechanical cell-matrix feedback explains pairwise and collective endothelial cell behavior in vitro,” *PLoS Computational Biology*, vol. 10, p. e1003774, aug 2014.

[93] M. Orme and M. Chaplain, “A mathematical model of vascular tumour growth and invasion,” *Mathematical and Computer Modelling*, vol. 23, pp. 43–60, may 1996.

[94] M. E. ORME and M. A. J. CHAPLAIN, “Two-dimensional models of tumour angiogenesis and anti-angiogenesis strategies,” *Mathematical Medicine and Biology*, vol. 14, pp. 189–205, sep 1997.

[95] H. A. Levine, B. D. Sleeman, and M. Nilsen-Hamilton, “A mathematical model for the roles of pericytes and macrophages in the initiation of angiogenesis. i. the role of protease inhibitors in preventing angiogenesis,” *Mathematical Biosciences*, vol. 168, pp. 77–115, nov 2000.

[96] S. B. Levine HA, Pamuk S and N.-H. M, “Mathematical modeling of capillary formation and development in tumor angiogenesis: Penetration into the stroma,” *Bulletin of Mathematical Biology*, vol. 63, pp. 801–863, sep 2001.

[97] A. Anderson and M. Chaplain, “Continuous and discrete mathematical models of tumor-induced angiogenesis,” *Bulletin of Mathematical Biology*, vol. 60, pp. 857–899, sep 1998.

[98] S. McDougall, “Mathematical modelling of flow through vascular networks: Implications for tumour-induced angiogenesis and chemotherapy strategies,” *Bulletin of Mathematical Biology*, vol. 64, pp. 673–702, jul 2002.

[99] N. V. Mantzaris, S. Webb, and H. G. Othmer, “Mathematical modeling of tumor-induced angiogenesis,” *Journal of Mathematical Biology*, vol. 49, feb 2004.

[100] P. Macklin, S. McDougall, A. R. A. Anderson, M. A. J. Chaplain, V. Cristini, and J. Lowengrub, "Multiscale modelling and nonlinear simulation of vascular tumour growth," *Journal of Mathematical Biology*, vol. 58, pp. 765–798, sep 2009.

[101] H. Perfahl, H. M. Byrne, T. Chen, V. Estrella, T. Alarcón, A. Lapin, R. A. Gatenby, R. J. Gillies, M. C. Lloyd, P. K. Maini, M. Reuss, and M. R. Owen, "Multiscale modelling of vascular tumour growth in 3d: The roles of domain size and boundary conditions," *PLoS ONE*, vol. 6, p. e14790, apr 2011.

[102] R. M. H. Merks, E. D. Perryn, A. Shirinifard, and J. A. Glazier, "Contact-inhibited chemotaxis in de novo and sprouting blood-vessel growth," *PLoS Computational Biology*, vol. 4, p. e1000163, sep 2008.

[103] D. Lakatos, E. Somfai, E. Méhes, and A. Czirók, "Soluble VEGFR1 signaling guides vascular patterns into dense branching morphologies," *Journal of Theoretical Biology*, vol. 456, pp. 261–278, nov 2018.

[104] A. Shirinifard, J. S. Gens, B. L. Zaitlen, N. J. Popławski, M. Swat, and J. A. Glazier, "3d multi-cell simulation of tumor growth and angiogenesis," *PLoS ONE*, vol. 4, p. e7190, oct 2009.

[105] A. L. Bauer, T. L. Jackson, and Y. Jiang, "Topography of extracellular matrix mediates vascular morphogenesis and migration speeds in angiogenesis," *PLoS Computational Biology*, vol. 5, p. e1000445, jul 2009.

[106] A. Shamloo, N. Mohammadaliha, S. C. Heilshorn, and A. L. Bauer, "A comparative study of collagen matrix density effect on endothelial sprout formation using experimental and computational approaches," *Annals of Biomedical Engineering*, vol. 44, pp. 929–941, aug 2015.

[107] J. R. D. Ramos, R. Travasso, and J. Carvalho, "Capillary network formation from dispersed endothelial cells: Influence of cell traction, cell adhesion, and extracellular matrix rigidity," *Physical Review E*, vol. 97, p. 012408, jan 2018.

[108] K. Bentley, G. Mariggi, H. Gerhardt, and P. A. Bates, "Tipping the balance: Robustness of tip cell selection, migration and fusion in angiogenesis," *PLoS Computational Biology*, vol. 5, p. e1000549, oct 2009.

[109] L. Venkatraman, E. R. Regan, and K. Bentley, "Time to decide? dynamical analysis predicts partial tip/stalk patterning states arise during angiogenesis," *PLOS ONE*, vol. 11, p. e0166489, nov 2016.

[110] M. Boareto, M. K. Jolly, E. Ben-Jacob, and J. N. Onuchic, "Jagged mediates differences in normal and tumor angiogenesis by affecting tip-stalk fate decision," *Proceedings of the National Academy of Sciences*, vol. 112, pp. E3836–E3844, jul 2015.

[111] M. Boareto, M. K. Jolly, M. Lu, J. N. Onuchic, C. Clementi, and E. Ben-Jacob, "Jagged–delta asymmetry in notch signaling can give rise to a sender/receiver hybrid phenotype," *Proceedings of the National Academy of Sciences*, vol. 112, pp. E402–E409, jan 2015.

[112] M. Boareto, M. K. Jolly, A. Goldman, M. Pietilä, S. A. Mani, S. Sengupta, E. Ben-Jacob, H. Levine, and J. N. Onuchic, "Notch-jagged signalling can give rise to clusters of cells exhibiting a hybrid epithelial/mesenchymal phenotype," *Journal of The Royal Society Interface*, vol. 13, p. 20151106, may 2016.

[113] M. K. Jolly, M. Boareto, M. Lu, J. N. Onuchic, C. Clementi, and E. Ben-Jacob, "Operating principles of notch-delta-jagged module of cell–cell communication," *New Journal of Physics*, vol. 17, p. 055021, may 2015.

[114] P. A. Roberts, E. A. Gaffney, P. J. Luthert, A. J. Foss, and H. M. Byrne, "Mathematical and computational models of the retina in health, development and disease," *Progress in Retinal and Eye Research*, vol. 53, pp. 48–69, jul 2016.

[115] R. Flower, C. von Kerczek, L. Zhu, A. Ernest, C. Eggleton, and L. Topoleski, “Theoretical investigation of the role of choriocapillaris blood flow in treatment of subfoveal choroidal neovascularization associated with age-related macular degeneration,” *American Journal of Ophthalmology*, vol. 132, pp. 85–93, jul 2001.

[116] A. E. Davies, R. L. Williams, G. Lugano, S. R. Pop, and V. R. Kearns, “In vitro and computational modelling of drug delivery across the outer blood–retinal barrier,” *Interface Focus*, vol. 10, p. 20190132, feb 2020.

[117] A. Shirinifard, J. A. Glazier, M. Swat, J. S. Gens, F. Family, Y. Jiang, and H. E. Grossniklaus, “Adhesion failures determine the pattern of choroidal neovascularization in the eye: A computer simulation study,” *PLoS Computational Biology*, vol. 8, p. e1002440, may 2012.

[118] L. Landau and E. Lifshitz, *Mechanics. 3rd ed.* Pergamon Press New York, 1976.

[119] R. M. Merks, S. V. Brodsky, M. S. Goligorksy, S. A. Newman, and J. A. Glazier, “Cell elongation is key to in silico replication of in vitro vasculogenesis and subsequent remodeling,” *Developmental Biology*, vol. 289, pp. 44–54, jan 2006.

[120] K. Sugihara, K. Nishiyama, S. Fukuhara, A. Uemura, S. Arima, R. Kobayashi, A. Köhn-Luque, N. Mochizuki, T. Suda, H. Ogawa, and H. Kurihara, “Autonomy and non-autonomy of angiogenic cell movements revealed by experiment-driven mathematical modeling,” *Cell Reports*, vol. 13, pp. 1814–1827, dec 2015.

[121] S. E. M. Boas and R. M. H. Merks, “Tip cell overtaking occurs as a side effect of sprouting in computational models of angiogenesis,” *BMC Systems Biology*, vol. 9, nov 2015.

[122] K. Herz, A. Becker, C. Shi, M. Ema, S. Takahashi, M. Potente, M. Hesse, B. K. Fleischmann, and D. Wenzel, “Visualization of endothelial cell cycle dynamics in mouse using the flt-1/eGFP-anillin system,” *Angiogenesis*, vol. 21, pp. 349–361, feb 2018.

[123] C. A. Reinhart-King, M. Dembo, and D. A. Hammer, “Cell-cell mechanical communication through compliant substrates,” *Biophysical Journal*, vol. 95, pp. 6044–6051, dec 2008.

[124] J. C. Kohn, D. W. Zhou, F. Bordeleau, A. L. Zhou, B. N. Mason, M. J. Mitchell, M. R. King, and C. A. Reinhart-King, “Cooperative effects of matrix stiffness and fluid shear stress on endothelial cell behavior,” *Biophysical Journal*, vol. 108, pp. 471–478, feb 2015.

[125] R. Vega, M. Carretero, R. D. M. Travasso, and L. L. Bonilla, “Notch signaling and taxis mechanisms regulate early stage angiogenesis: A mathematical and computational model,” *PLOS Computational Biology*, vol. 16, p. e1006919, jan 2020.

[126] H. X. Bai, Y. Mao, L. Shen, X. L. Xu, F. Gao, Z. B. Zhang, B. Li, and J. B. Jonas, “Bruchs membrane thickness in relationship to axial length,” *PLOS ONE*, vol. 12, p. e0182080, aug 2017.

[127] T. R. Friberg, R. A. Bilonick, and P. Brennen, “Is drusen area really so important? an assessment of risk of conversion to neovascular AMD based on computerized measurements of drusen,” *Investigative Opthalmology & Visual Science*, vol. 53, p. 1742, apr 2012.

[128] S. Poh, Y.-C. Tham, M. L. Chee, W. Dai, S. Majithia, Z. D. Soh, E. K. Fenwick, Y. Tao, S. Thakur, T. H. Rim, C. Sabanayagam, and C.-Y. Cheng, “Association between macular thickness profiles and visual function in healthy eyes: The singapore epidemiology of eye diseases (SEED) study,” *Scientific Reports*, vol. 10, p. 6142, apr 2020.

[129] V. K. Gullapalli, I. K. Sugino, Y. V. Patten, S. Shah, and M. A. Zarbin, “Impaired RPE survival on aged submacular human bruchs membrane,” *Experimental Eye Research*, vol. 80, pp. 235–248, feb 2005.

[130] Y. Imamura, S. Noda, K. Hashizume, K. Shinoda, M. Yamaguchi, S. Uchiyama, T. Shimizu, Y. Mizushima, T. Shirasawa, and K. Tsubota, “Drusen, choroidal neovascularization, and retinal pigment epithelium dysfunction in SOD1-deficient mice: A model of age-related macular degeneration,” *Proceedings of the National Academy of Sciences*, vol. 103, pp. 11282–11287, jul 2006.

[131] R. Simó, M. Villarroel, L. Corraliza, C. Hernández, and M. Garcia-Ramírez, “The retinal pigment epithelium: Something more than a constituent of the blood-retinal barrier—implications for the pathogenesis of diabetic retinopathy,” *Journal of Biomedicine and Biotechnology*, vol. 2010, pp. 1–15, 2010.

[132] I. A. Bhutto, D. S. McLeod, T. Hasegawa, S. Y. Kim, C. Merges, P. Tong, and G. A. Lutty, “Pigment epithelium-derived factor (PEDF) and vascular endothelial growth factor (VEGF) in aged human choroid and eyes with age-related macular degeneration,” *Experimental Eye Research*, vol. 82, pp. 99–110, jan 2006.

[133] V. Markovtsev and M. Cuadros, *Src–D/Kmcuda: 6.0.0–1*, 2017.

[134] R. J. LeVeque, *Finite Difference Methods for Ordinary and Partial Differential Equations: Steady-State and Time-Dependent Problem.* SIAM, 2007.